



Universität Augsburg
Mathematisch-Naturwissenschaftlich-
Technische Fakultät

Preparation and Characterization of Thermoelectric SiGe Thin Films Processed by Al Mediated Metal-Induced Crystallization

Dissertation

zur Erlangung des akademischen Grades

Dr. rer. nat.

eingereicht an der

Mathematisch-Naturwissenschaftlich-Technischen Fakultät

der Universität Augsburg

von

Marc Erik Lindorf

Augsburg, Juli 2017

Erstgutachter: Prof. Dr. Manfred Albrecht
Zweitgutachter: Prof. Dr. Simone Raoux

Termin der mündlichen Prüfung: 20.10.2017

Lindorf, Marc Erik

Preparation and Characterization of Thermoelectric SiGe Thin Films Processed by
Al Mediated Metal-Induced Crystallization

Dissertation

Universität Augsburg, Juli 2017

Contents

1	Introduction	1
2	Theoretical Background	5
2.1	Thermoelectric transport theory	5
2.1.1	Thermodynamic forces and fluxes	5
2.1.2	Thermoelectric coefficients	7
2.1.3	Thermoelectric efficiency	10
2.2	Overview of transport properties for different material classes	11
2.2.1	Charge carrier density	11
2.2.2	Electrical conductivity	15
2.2.3	Seebeck coefficient	16
2.2.4	Thermal conductivity	18
2.2.5	Figure of merit	18
2.3	The classical thermoelectric material SiGe	20
2.4	Metal-induced crystallization	24
3	Experimental Techniques	27
3.1	Sputter deposition for thin film approach	27
3.2	Secondary Neutral/Ion Mass Spectrometry	28
3.3	Rutherford Backscattering Spectrometry	29
3.4	X-ray Diffraction	31
3.5	Electron Microscopy	33
3.5.1	Scanning Electron Microscopy	34
3.5.2	Transmission Electron Microscopy	34
3.5.3	Energy Dispersive X-ray Spectrometry	35
3.6	Resistance measurement	35
3.7	Hall Effect measurement	37
3.8	Seebeck measurement	39
3.9	Thermal conductivity measurement	42
4	Results and Discussion	45
4.1	Characterization of SiGe/Al multilayer systems on thermally oxidized Si substrates	45
4.1.1	Verification of MIC in SiGe/Al multilayer systems	45

4.1.2	Transport properties	53
4.2	Characterization of SiGe/Al multilayer systems on aluminum oxide based substrates	59
4.2.1	Microstructure and morphology	59
4.2.2	Transport properties during MIC phase change	67
4.2.3	Influence of the ratio Al:SiGe on the resulting transport properties after MIC phase change	71
4.2.4	Influence of the Al thickness on MIC	78
4.2.5	Thermal conductivity measurements	81
4.3	Characterization of SiGe/Al systems on silicon oxide substrates	83
4.3.1	Reduction of silicon oxide by aluminum	84
4.3.2	Structural Characterization	84
4.3.3	Estimation of SiGe thickness increase	101
4.3.4	Thermoelectric Properties	102
5	Summary	111
	Bibliography	115
	Acknowledgment	125
	Publications	127

1 Introduction

In the last three decades, the world energy consumption has more than doubled [1]. This trend is projected as an averaged 1.4% increase per year until 2040 [2]. Although there are strong efforts to facilitate the use of renewable energies, only about 15% of the total worldwide energy consumption were covered by renewable energy sources in the year 2014 [1]. With fossil energy sources like coal, oil, and gas becoming more and more scarce, the renewable energy sector will have to grow accordingly to compensate for the future lack of fossil energy sources. Renewable energies like wind, solar, and geothermal energy solutions have emerged in the last decades and grew to provide the biggest contribution to the renewable energy sector besides bio fuels [1]. These forms of power generation are coupled to specific local requirements to be economically worthwhile as for example having strong enough winds or hours of sunshine over the year.

Another form of energy source independent of fossil fuels is thermoelectricity. Thermoelectricity enables the transformation of temperature gradients into electrical energy and vice versa. Such temperature gradients are present in every other kind of power generation in the form of waste heat, which could be harvested by thermoelectric devices. Energy losses due to waste heat were estimated in 1971 to 50% of the industrially generated energy in the USA [3], which highlights the potential of waste heat as a form of energy generation without directly relying on fossil fuels. Even the harvesting of naturally abundant temperature gradients provided in the form of human body heat could be utilized in energy self-sufficient systems [4].

The foundations of thermoelectricity were laid in 1821 with the discovery of the Seebeck effect by the Baltic German physicist T. J. Seebeck [5]. He demonstrated that the application of a temperature gradient led to a measurable thermovoltage in metals. In 1834, the French physicist J. C. A. Peltier discovered another thermoelectric effect known as the Peltier effect [5]. This effect describes the emergence of a heat flux due to an electric current. The last thermoelectric effect called Thomson effect was discovered by the British Lord B. Kelvin (formerly William Thomson) in 1851 [6] and describes the absorption or emission of heat when an electric current flows in a material under an applied temperature gradient. The first constant property model to derive parameters for maximum thermoelectric efficiency was introduced by E. Altenkirch in 1911 [7]. It was shown that a high Seebeck coefficient α , a high electrical conductivity σ , and a low thermal conductivity κ are needed to get a highly efficient thermoelectric material. Later on, these thermoelectric transport parameters were combined into the so called figure of merit $ZT = \alpha^2 \sigma \kappa^{-1} T$. This up-to-date used

theory of thermoelectricity along with the introduction of semiconductors as prime thermoelectric material like the classic thermoelectric material SiGe was given by the Russian physicist A. F. Ioffe in 1949 and the following years [8][9].

Despite numerous potential applications, thermoelectric devices are still limited to niche applications like autonomous sensor systems [10], where high reliability and lifetime outweigh their generally low conversion efficiencies [11]. The interdependence of the thermoelectric parameters α , σ , and κ led to the perceived limit of $ZT < 1$ [12] resulting in efficiencies for thermoelectric devices well below 10% until the end of the 1960s. The most prominent application of thermoelectricity was found in space exploration missions to the edge of our solar system, where solar panels are not functional anymore [13]. Here, radioisotope generators based on SiGe were used to supply electrical power through heat generated by radioactive decay.

The interest in thermoelectric research just got reinvigorated in the last two decades by exploring intricate material groups like bismuth chalcogenides (f.e. Bi_2Se_3 , Bi_2Te_3) [14][15], inorganic clathrates (f.e. $\text{Ba}_8\text{Ga}_{16}\text{Ge}_{30}$) [16][17], skutterudites (f.e. CoSb_3) [18][19], and Half Heusler alloys (f.e. $\text{Hf}_{1-x}\text{Zr}_x\text{NiSn}_{1-y}\text{Sb}_y$) [20][21]. Additionally, designing such materials on the nanoscale opened up new possibilities to decouple the linked thermoelectric parameters and improve ZT beyond 1. Approaches included the design of nanocomposites [22], nanostructured material [23], and low dimensional systems [24]. Furthermore, the field of organic thermoelectrics sparked a lot of interest as modern organic polymers can exhibit electrical conductivity in the range of doped semiconductors while retaining their inherently low thermal conductivity [25]. Such materials also present the possibility of being printable and when being prepared on bendable substrates lead to flexible thermoelectrics [25]. Nevertheless, also classic thermoelectric materials underwent improvement with respect to new preparation methods. Such methods include high energy ball milling [26], superlattices [27], and modulation doping [28] in the case of SiGe.

In this work, a thin film approach to thermoelectric SiGe with industrial applicable preparation methods will be presented. Instead of the commonly utilized approach of ball milling and sintering for the production of nanostructured bulk SiGe, the processes of sputter deposition and metal induced crystallization (MIC) were combined to prepare nanocrystalline SiGe thin films. MIC is a process that enables the crystallization of semiconductors like SiGe at temperatures significantly lower than their ordinary crystallization temperature [29]. Aluminum was used as the catalytic metal for the MIC process. This provided the advantages of a low thermal budget, self-doping (p-type), and control over the crystallization process via parameters like Al thickness, annealing temperature and time. Samples were characterized regarding their morphology, composition, microstructure, and crystallinity comparing the as-deposited and post-annealing state. The results were related to the thermoelectric transport properties of electrical conductivity and Seebeck coefficient. Special emphasis was put on the influence of the Al layer thickness on the MIC process itself and

the ratio of Al:SiGe with respect to the transition from metallic to semiconducting transport properties.

2 Theoretical Background

2.1 Thermoelectric transport theory

This chapter shall introduce the reader to the basic principles of thermoelectricity. The thermoelectric transport coefficients will be derived from a thermodynamic point of view. For a more detailed approach please refer to [30][31].

2.1.1 Thermodynamic forces and fluxes

Thermoelectric transport is governed by the occurrence of thermodynamic fluxes originating from thermodynamic forces. Such forces can be understood as gradients of thermodynamic variables. The main relations regarding thermoelectricity can be written as

$$J_Q = -\kappa \nabla T \quad (2.1)$$

$$J_{el} = -\sigma \nabla \phi \quad (2.2)$$

$$J_N = -D \nabla N \quad (2.3)$$

with

J_Q – heat flux

J_{el} – charge flux

J_N – particle flux

κ – thermal conductivity

σ – electrical conductivity

D – diffusion coefficient

T – temperature

ϕ – electrical potential

N – particle density.

Empirically, it is known that cross-coupling between these forces and fluxes exist such as a thermal gradient giving rise to an electric flux and a potential gradient leading to a heat flux. Under the assumption of superposition of the effects and linear coupling

terms, the fluxes can be expressed as

$$J_{el} = L_{11}\nabla\phi + L_{12}\nabla T, \quad (2.4)$$

$$J_Q = L_{21}\nabla\phi + L_{22}\nabla T. \quad (2.5)$$

It was Onsager, who showed that for proper pairs of forces F_i and fluxes J_i the cross-coupling terms L_{ij} become equal in the absence of a magnetic field [32]. Thus, equations (2.4) and (2.5) can be interpreted with a linear cross-coupling term L_{12} as

$$J_1 = L_{11}F_1 + L_{12}F_2, \quad (2.6)$$

$$J_2 = L_{12}F_1 + L_{22}F_2 \quad (2.7)$$

under the entropy condition

$$\frac{\partial S_i}{\partial t} = J_1F_1 + J_2F_2 \quad (2.8)$$

with $\frac{\partial S_i}{\partial t}$ marking the rate of increase in entropy density due to irreversible processes. The continuity equations for a closed system in steady state condition are

$$\nabla J_N = -\frac{\partial N}{\partial t} = 0, \quad (2.9)$$

$$\nabla J_U = -\frac{\partial u}{\partial t} = 0 \quad (2.10)$$

with u and J_U being the internal energy density and its flux, respectively. Since the entropy S of a system is not conserved, the continuity equation for the entropy flux J_S reads

$$\nabla J_S = \frac{\partial S_i}{\partial t}. \quad (2.11)$$

Introducing the electrochemical potential μ_e , chemical potential μ_c , and the signed elementary charge e (+ for holes, - for electrons)

$$\mu_e = \mu_c + e\phi, \quad (2.12)$$

it becomes possible to form a relationship for the fluxes (assuming constant volume) in analogy to $du = TdS + \mu_e dN$ as

$$J_S = \frac{1}{T}J_U - \frac{1}{T}\mu_e J_N. \quad (2.13)$$

Taking the divergence for both sides leads to

$$\nabla J_S = \frac{\partial S_i}{\partial t} = \nabla \left(\frac{1}{T} \right) J_U - \nabla \left(\frac{1}{T} \right) \mu_e J_N - \frac{1}{T} \nabla(\mu_e) J_N, \quad (2.14)$$

if a closed system is assumed. Replacing $J_U = J_Q + \mu_e J_N$

$$\frac{\partial S_i}{\partial t} = \nabla \left(\frac{1}{T} \right) J_Q - \frac{1}{T} \nabla (\mu_e) J_N. \quad (2.15)$$

A comparison with equation (2.8) allows the following identifications

$$J_1 = J_N, \quad F_1 = -\frac{1}{T} \nabla \mu_e, \quad J_2 = J_Q, \quad F_2 = \nabla \left(\frac{1}{T} \right) \quad (2.16)$$

leading to

$$\begin{bmatrix} J_N \\ J_Q \end{bmatrix} = \begin{bmatrix} L_{11} & L_{12} \\ L_{12} & L_{22} \end{bmatrix} \begin{bmatrix} -\frac{1}{T} \nabla \mu_e \\ \nabla \left(\frac{1}{T} \right) \end{bmatrix} \quad (2.17)$$

2.1.2 Thermoelectric coefficients

Decoupled processes

At first the decoupled processes of electrical and thermal conduction without any cross-coupling are derived. Under isothermal conditions

$$\nabla \left(\frac{1}{T} \right) = -\frac{1}{T^2} \nabla T = 0, \quad (2.18)$$

equation (2.17) reveals an expression for the electrical current density

$$J_{el} = e J_N = -\frac{e L_{11}}{T} \nabla \mu_e. \quad (2.19)$$

Knowing that the electric field can be expressed by

$$\mathcal{E} = -\nabla \phi = -\frac{\nabla \mu_e}{e}, \quad (2.20)$$

expression (2.19) of Ohm's law (2.2) can be used to define an isothermal electrical conductivity as

$$\sigma_T = \frac{e^2}{T} L_{11}. \quad (2.21)$$

Similarly by assuming the absence of any particle transport and, therefore, zero electrical current

$$J_{el} = 0 = -L_{11} \left(\frac{\nabla \mu_e}{T} \right) + L_{12} \nabla \left(\frac{1}{T} \right) \quad (2.22)$$

is obtained leading to the expression for the heat flux density at zero electrical current

$$J_{QJ} = \frac{1}{T^2} \left(\frac{L_{12}^2 - L_{11} L_{22}}{L_{11}} \right) \nabla T. \quad (2.23)$$

This is Fourier's law (2.1) with a thermal conductivity κ_J under zero electrical current (open circuit)

$$\kappa_J = \frac{1}{T^2} \left(\frac{L_{11}L_{22} - L_{12}^2}{L_{11}} \right). \quad (2.24)$$

Lastly, a thermal conductivity κ_E at zero electrochemical gradient (closed circuit) can also be derived

$$J_{QE} = -\frac{L_{22}}{T^2} \nabla T \quad \text{with} \quad \kappa_E = \frac{L_{22}}{T^2}. \quad (2.25)$$

Coupled processes

Considering equations (2.18), (2.20), and (2.22), the following relationship in the absence of any particle transport can be obtained

$$-\frac{\nabla \mu_e}{e} = -T \frac{L_{12}}{eL_{11}} \nabla \left(\frac{1}{T} \right) = \frac{L_{12}}{eTL_{11}} \nabla T = \mathcal{E}|_{J_{el}=0}. \quad (2.26)$$

Integration along the temperature gradient and electric field leads to an expression for the voltage U , which can be written as infinitesimal changes

$$dU = \frac{L_{12}}{eTL_{11}} dT. \quad (2.27)$$

Thus, the identity for a thermoelectric transport coefficient is obtained by the definition of the Seebeck coefficient

$$\alpha \equiv \frac{dU}{dT} = \frac{1}{eT} \frac{L_{12}}{L_{11}}. \quad (2.28)$$

In consideration of equation (2.17) under isothermal condition, it is possible to derive the coupling term between the electrical current density and heat flux

$$J_{el} = eL_{11} \left(-\frac{1}{T} \nabla \mu_e \right), \quad J_Q = L_{12} \left(-\frac{1}{T} \nabla \mu_e \right) \Rightarrow J_Q = \frac{L_{12}}{eL_{11}} J_{el}. \quad (2.29)$$

This corresponds to the definition of the Peltier coefficient

$$J_Q = \Pi J_{el} \quad \text{with} \quad \Pi = \frac{1}{e} \frac{L_{12}}{L_{11}}. \quad (2.30)$$

A comparison of Seebeck and Peltier coefficient leads to the second Thomson relation

$$\Pi = \alpha T. \quad (2.31)$$

Entropy transport

A charged carrier can be identified as a carrier of entropy in the sense of a classical thermodynamic cycle. This interpretation is obtained by the entropy flux

$$J_S = \frac{J_Q}{T} = \frac{1}{T} \left[L_{12} \left(-\frac{1}{T} \nabla \mu_e \right) + L_{22} \nabla \left(\frac{1}{T} \right) \right]. \quad (2.32)$$

According to equation (2.19), this can be simplified into

$$J_S = \frac{L_{12}}{eTL_{11}} J_{el} + \frac{1}{T} L_{22} \nabla \left(\frac{1}{T} \right). \quad (2.33)$$

Two contributions to the entropy flux are identified, one from electrochemical origin and the other from thermal origin. Looking at the first term, an entropy transported per charged carrier S_N is given by

$$S_N = \frac{L_{12}}{TL_{11}}. \quad (2.34)$$

Consequently one can see by comparison with equation (2.28), the Seebeck coefficient is directly related to S_N by

$$S_N = e\alpha \quad (2.35)$$

and thus showing the direct link for thermoelectricity between macroscopic and microscopic scale.

Transport parameters

Until now, the following correspondence between the kinetic coefficients of the Onsager relationships and the thermoelectric transport parameters was obtained

$$\begin{array}{ccc} \hline L_{11} & L_{12} & L_{22} \\ \hline \frac{T}{e^2} \sigma_T & \frac{T^2}{e} \sigma_T \alpha & T^3 \sigma_T \alpha^2 + T^2 \kappa_J \\ \hline \end{array}$$

The Onsager relationships itself are

$$J_{el} = -\sigma_T \left(\frac{\nabla \mu_e}{e} \right) + \frac{\sigma_T \alpha T^2}{e} \nabla \left(\frac{1}{T} \right), \quad (2.36)$$

$$J_Q = -T \sigma_T \alpha \left(\frac{\nabla \mu_e}{e} \right) + (T^3 \sigma_T \alpha^2 + T^2 \kappa_J) \nabla \left(\frac{1}{T} \right). \quad (2.37)$$

Finally, the thermal conductivity under zero electrochemical gradient and under zero electrical current can be linked by equations (2.21), (2.24), (2.25), and (2.28)

$$\kappa_E = T \alpha^2 \sigma_T + \kappa_J. \quad (2.38)$$

Inserting equation (2.36) into equation (2.37) and using the identities (2.18) and (2.20), the "classical" thermoelectric transport equations

$$J_{el} = \sigma_T \mathcal{E} - \sigma_T \alpha \nabla T, \quad (2.39)$$

$$J_Q = \alpha T J_{el} - \kappa_J \nabla T \quad (2.40)$$

are obtained.

2.1.3 Thermoelectric efficiency

When discussing thermoelectric efficiency of a given material, one first has to decide whether an electric heat pump driven by an input electric current or a thermoelectric generator driven by a supplied thermal gradient is to be considered. Since for both cases the same principal results are obtained, this topic will be explained exemplarily for the case of a thermoelectric generator [31].

Thermoelectric materials are energy conversion devices and, thus, can convert more electrical output power the more heat flow they can take in. A large thermal conductivity is therefore required. In such a configuration, the material will exhibit a thermal shortcut leading to a very small temperature difference and consequently a small electric output voltage. As the fluxes are maximized and potential differences minimized, this is called the short-circuit configuration.

Now the thermoelectric material is considered from the potential point of view. A large temperature difference is needed to produce a large electric output voltage. Hence, the thermal conductivity of the material should be as small as possible to uphold the temperature gradient leading to only a very small heat input that is converted into electrical power output. In contrast to the former conditions, this is the so called open-circuit configuration, which exhibits maximized potential differences and minimized fluxes.

It becomes apparent, that neither for the short-circuit nor for the open-circuit configuration a satisfactory solution is obtained. Additionally, both configurations contradict each other by having maximal and minimal thermal conductivity, respectively. Remembering the two different thermal conductivities of equation (2.38), one can assign κ_J to the open-circuit configuration ($J_{el} = 0$) and κ_E to the short-circuit configuration ($\nabla \mu_e = 0$) and solve the contradiction by expecting the ratio $\frac{\kappa_E}{\kappa_J}$ to be maximal to achieve maximum electrical output power. Rearranging equation (2.38) leads to

$$\frac{\kappa_E}{\kappa_J} = \left[\frac{\alpha^2 \sigma_T}{\kappa_J} T + 1 \right] \quad (2.41)$$

with the dimensionless figure of merit ZT defined as

$$ZT = \frac{\alpha^2 \sigma_T}{\kappa_J} T. \quad (2.42)$$

This quantity is directly related to the maximal efficiency η of a thermoelectric generator

$$\eta = \frac{T_h - T_c}{T_h} \frac{\sqrt{1 + ZT_m} - 1}{\sqrt{1 + ZT_m} + \frac{T_c}{T_h}} \quad (2.43)$$

with T_h and T_c being the hot and cold side temperature of the applied thermal gradient, respectively, and $T_m = (T_h + T_c)/2$ [31].

However, if the user of a thermoelectric generator is only interested in maximum power output P_{\max}^{out} , this leads to a different optimization

$$P_{\max}^{\text{out}} = \frac{\alpha^2 (T_h - T_c)^2}{4R_{\text{in}}} \quad (2.44)$$

with R_{in} representing the internal electrical resistance of the thermoelectric generator [31]. As the internal resistance is indirectly proportional to the electrical conductivity, it becomes apparent that the maximal power output is directly proportional to the so called power factor $\alpha^2\sigma$

$$P_{\max}^{\text{out}} \propto \alpha^2\sigma. \quad (2.45)$$

This reveals that in contrast to the maximal efficiency approach the thermal conductivity κ can be neglected as an optimization parameter for a thermoelectric generator, if the user is only interested in maximal power output being the case for most waste heat applications. Similar approaches from an engineering point of view regarding system losses due to compatibility issues with regard to contact resistances led to the train of thought that not only ZT should be considered, but also the actual assembly and integration of a thermoelectric module must be considered to achieve appropriate device performance [33].

2.2 Overview of transport properties for different material classes

This chapter shall provide the reader with a short overview of the different typical transport properties for different material classes in the crystalline state. Emphasis will be put on the properties of electrical conductivity σ , Seebeck coefficient α , and thermal conductivity κ , but since all these parameters are dependent on the charge carrier density n this general linking parameter will first be considered.

2.2.1 Charge carrier density

The (free) charge carrier density n of any crystalline material is generally governed by the relationship between allowed energy E and wave vector k for its charge carriers known as dispersion relation $E(k)$. This gives rise to a model of energy bands in

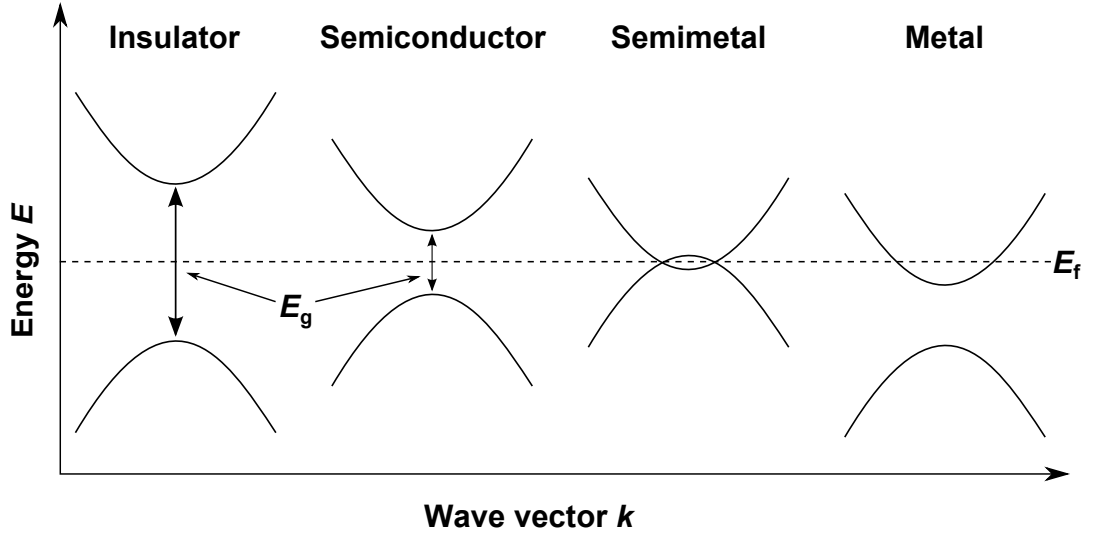


Figure 2.1: Principle energy band structure cases around the Fermi energy E_f .

which the electrons are filled up from the bottom to the Fermi energy E_f according to the Pauli principle. Also charge carriers are only able to contribute to electrical transport phenomena, if their current occupied state $E(k)$ adjoins to an unoccupied one and, therefore, can be treated as free. Accordingly, the first band above E_f is called conduction band and the one below valence band. Depending on the actual arrangement of the energy bands near the Fermi energy, the band structure of a material can be divided into four basic cases shown in fig 2.1.

Intrinsic materials

In the case of intrinsic insulators and semiconductors, an area of forbidden states between conduction and valence band is observed around the Fermi energy being called energy band gap E_g . Consequently, for $T = 0$ no free charge carriers are present. Only for temperatures $T > 0$, it becomes possible for electrons to be excited into the empty conduction band and, therefore, act as free charge carriers contributing to n . Additionally to free electrons n_n in the conduction band, unoccupied states in the valence band left behind by thermally excited electrons can also act as free charge carriers being called holes n_p and behave like positively charged carriers. The charge carriers being thermally excited are given by the Boltzmann distribution

$$n_n = N_C \exp\left(-\frac{E_C - E_f}{k_B T}\right) \quad (2.46)$$

and

$$n_p = N_V \exp\left(-\frac{E_f - E_V}{k_B T}\right) \quad (2.47)$$

with $N_C(\propto T^{3/2})$ and $N_V(\propto T^{3/2})$ being the density of states at the conduction and valence band edge E_C and E_V , respectively, and the Boltzmann constant k_B [34]. The overall intrinsic charge carrier density n_i is then given by the mass-action law $n_i^2 = n_n n_p$

$$n_i = \sqrt{n_n n_p} = \sqrt{N_C N_V} \exp\left(-\frac{E_g}{2k_B T}\right) \quad \text{with} \quad E_g = E_C - E_V. \quad (2.48)$$

While the band gap energies of semiconductors are small enough with $E_{g,sc} \leq 1\text{eV}$ to be overcome at rather moderate temperatures ($n_{sc,intr} < 10^{14} \text{cm}^{-3}$), the band gap energies of insulators are too large with $E_{g,ins} \gg 1\text{eV}$ and only a negligible amount of free charge carriers can be thermally excited before the material starts to melt. For semimetals a virtually negative band gap is observed resulting in an overlap of conduction and valence band. Hence, both electrons and holes are present in such systems ($n_{sm} \approx 10^{18} - 10^{20} \text{cm}^{-3}$), which is detrimental to thermoelectric performance as will be discussed later for the Seebeck coefficient.

The forbidden band gap of metals lies far below E_f with E_f lying in the conduction band. Because of the already partially filled conduction band, no additional thermal excitation is needed for free charge carriers and such the free charge carrier density is only limited by the density of states near E_f ($n_{met} > 10^{20} \text{cm}^{-3}$).

Extrinsic materials

It is possible to control the position of the Fermi energy of a given intrinsic host material as shown in fig 2.2 by introducing additional allowed energy states to the band structure through insertion of foreign elements. This is called doping, most commonly used for semiconductors, and the resulting doped semiconductor is then called extrinsic. If already occupied states E_D are introduced and are close beneath the conduction band edge E_C , a n-type semiconductor is obtained with electrons being the majority of charge carriers. Contrarily, introduction of unoccupied states E_A above the valence band edge E_V leads to a p-type semiconductor with holes as majority charge carriers. Therefore, E_f will lie in between E_C and E_D or E_V and E_A , respectively, if the density of introduced states is still lower compared to the density of states of the respective band edge N_C or N_V and a non degenerate semiconductor is preserved. In consequence, the energy gap for carriers required to be thermally excited is significantly reduced and the charge carrier density n is governed by the

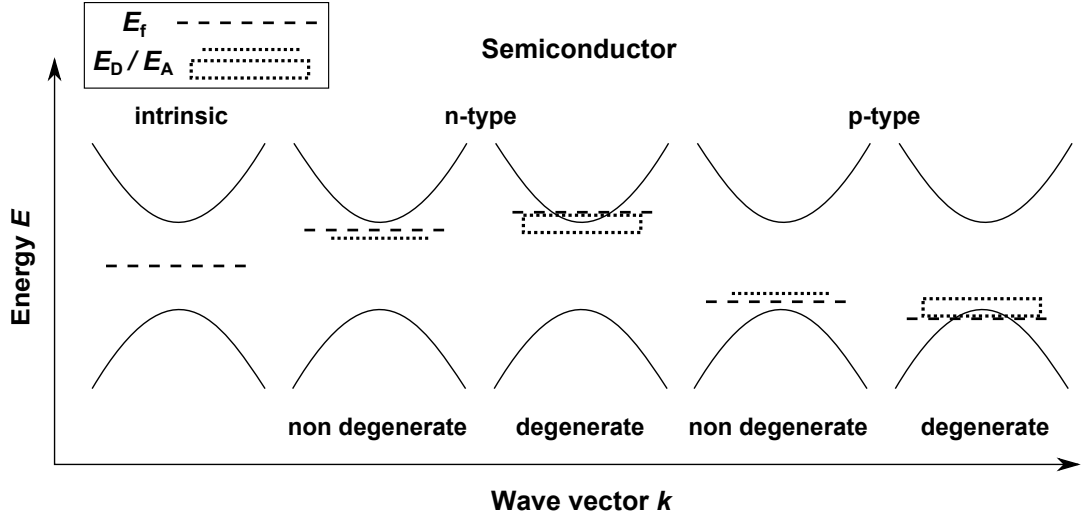


Figure 2.2: Position of Fermi energy E_f and donor or acceptor levels E_D and E_A for differently doped semiconductors.

doping density N_D or N_A . Equations (2.46) and (2.47) change to [34]

$$n_n \approx \sqrt{\frac{N_D N_C}{2}} \exp\left(-\frac{E_C - E_D}{2k_B T}\right), \quad (2.49)$$

$$n_p \approx \sqrt{\frac{N_A N_V}{2}} \exp\left(-\frac{E_A - E_V}{2k_B T}\right). \quad (2.50)$$

Charge carrier densities in the range of $10^{14} \text{ cm}^{-3} < n_{sc,dop} < 10^{18} \text{ cm}^{-3}$ can be achieved easily.

If the number of introduced foreign atoms and, therefore, the doping density of states becomes similar or even bigger than the density of states near the band edge, a degenerate semiconductor is obtained. For this case, the respective donor or acceptor states E_D and E_A do not only show isolated energy levels, but form complete impurity bands as the doping atoms start to interact with each other. These impurity bands then reach into the bands of the pristine semiconductor and also push the Fermi energy E_f into them. A state similar to a metal is achieved, where a partially filled band is available for electric transport phenomena with a temperature independent charge carrier density n . Consequently, degenerate semiconductors can be treated like metals regarding to their transport properties with charge carrier densities of $n_{sc,deg} > 10^{18} \text{ cm}^{-3}$ as long as the temperature is low enough for intrinsic excitation to be negligible.

2.2.2 Electrical conductivity

The electrical conductivity σ of a material is the reciprocal value of its resistivity ρ and directly related to its charge carrier density n and charge carrier mobility μ

$$\sigma = \frac{1}{\rho} = ne\mu. \quad (2.51)$$

The mobility μ can be expressed as

$$\mu = \frac{e\tau}{m^*} \quad (2.52)$$

with τ being the mean free time between collisions and m^* the effective mass of the charge carriers. The effective mass can be treated as virtually temperature independent, because of its dependence on the dispersion relation

$$m_{ij}^* = \frac{1}{\hbar^2} \frac{\partial^2 E(k)}{\partial k_i \partial k_j}. \quad (2.53)$$

The mean free time can be calculated by the Matthiessen rule

$$\tau = \left(\frac{1}{\tau_{\text{imp}}} + \frac{1}{\tau_{\text{ph}}} \right)^{-1}. \quad (2.54)$$

Hereby, τ_{imp} and τ_{ph} are the mean free times regarding collisions with impurities and phonons, respectively, and mark the main contributions at elevated temperatures.

Intrinsic insulators and semiconductors

It was shown that the respective contributions to the mobility given by the mean free time for non degenerate insulators and semiconductors equate to [35]

$$\mu_{\text{imp}} \propto \frac{T^{3/2}}{N_{\text{imp}} m^{*1/2}} \quad (2.55)$$

and [36]

$$\mu_{\text{ph}} \propto \frac{1}{m^{*5/2} T^{3/2}}. \quad (2.56)$$

Consequently, for lower temperatures the dominating contribution stems from ionized impurities while for higher temperatures phonons will be the main contributor. The characteristic temperature in that regard is called Debye temperature Θ_D [37]. Remembering equations (2.48)-(2.50) and knowing that for densities of states $N_i \propto T^{3/2}$ [34], the following temperature dependencies can be derived

$$\sigma_{sc} \propto T^3 \exp\left(-\frac{1}{T}\right) \quad \text{for } T \ll \Theta_D, \quad (2.57)$$

$$\sigma_{sc} \propto \exp\left(-\frac{1}{T}\right) \quad \text{for } T \gg \Theta_D. \quad (2.58)$$

Doped, non degenerate semiconductors

For lightly doped and therefore still non degenerate semiconductors, the same deductions are principally valid except for the temperature range where all doping states are already thermally excited and cannot generate any further free charge carriers, but also the temperature is still too low for intrinsic excitation to be noticeable. For this saturation range, the charge carrier density is temperature independent and only the mobility dependencies influence the electrical conductivity [34].

Metals and degenerate semiconductors

Metals and highly doped degenerate semiconductors exhibit temperature independent charge carrier densities. Hence, only the mobility needs to be considered with regard to their electrical conductivity. Added resistance due to impurities stems from crystal imperfections for that case and, thus, is a temperature independent offset

$$\tau_{\text{imp}}(T) = \text{const.} \quad (2.59)$$

The number of phonons in such systems grows linearly with temperature [38]. As the number of scatterers increases, the mean free time is reduced accordingly

$$\tau_{\text{ph}} \propto T^{-1}. \quad (2.60)$$

The electrical conductivity of a metal then follows

$$\sigma_{\text{met}} \propto T^{-1}. \quad (2.61)$$

This can be better understood when looking at the resistivity

$$\rho_{\text{met}} = \rho_{\text{imp}} + \rho_{\text{ph}}(T) \quad (2.62)$$

as a temperature independent, residual resistance due to impurities and the known linear increase of resistance due to increasing phonon numbers with temperature for metals. While this holds true for temperatures above the Debye temperature, a different behavior for lower temperatures can be observed as [38]

$$\rho_{\text{met}} \propto T^5. \quad (2.63)$$

2.2.3 Seebeck coefficient

The Seebeck coefficient α of a given system of independent electrons interacting with static scatterers is described by the Mott formula

$$\alpha = \frac{\pi^2 k_{\text{B}}^2 T}{3e} \left(\frac{d \ln \sigma(E)}{dE} \right)_{E=0}. \quad (2.64)$$

A detailed approach to this formula can be found in [39]. If a material exhibits more than one kind of charge carrier (e.g. multi band excitation [40], intrinsic excitation), the single Seebeck coefficients are weighted by the respective electrical conductivities [40]

$$\alpha_{\text{tot}} = \sum_i \frac{\sigma_i \alpha_i}{\sigma}. \quad (2.65)$$

This explains why semimetals are bad thermoelectric materials as the Seebeck coefficients of electrons and holes cancel each other out effectively.

Non degenerate insulators and semiconductors

The Seebeck coefficient of a n-type semiconductor is given by [41]

$$\alpha_n = \frac{k_B}{e} \left[\ln \left(\frac{N_C}{n_n} \right) + A_{\text{tr}} \right] \quad (2.66)$$

and of a p-type semiconductor by

$$\alpha_p = \frac{k_B}{e} \left[\ln \left(\frac{N_V}{n_p} \right) + A_{\text{tr}} \right]. \quad (2.67)$$

with A_{tr} being a transport constant lying in the range between 0 and 4. Please note that in this notation, a signed elementary charge e is used like in chapter 2.1.2 and such the Seebeck coefficient for n-type is of negative value. The charge carrier density for non degenerate semiconductors and insulators is very well temperature dependent and so is the Seebeck coefficient. Inserting equations (2.46) and (2.47) reveals that the Seebeck coefficient is indirectly proportional to the temperature for the intrinsic regime.

Metals and degenerate semiconductors

The solution of the Mott formula (2.64) leads to

$$\alpha_{\text{met}} = \frac{8\pi^2 k_B^2}{3eh^2} m^* T \left(\frac{\pi}{3n} \right)^{2/3} \quad (2.68)$$

in the case of metals and degenerate semiconductors [42]. This Seebeck coefficient shows a direct linear increase with temperature in contrast to the Seebeck coefficient of intrinsic semiconductors due to the effective mass m^* and charge carrier density n being temperature independent here.

2.2.4 Thermal conductivity

The thermal conductivity κ of any material is divided into a contribution of the charge carriers κ_{el} and the lattice κ_{lat}

$$\kappa = \kappa_{\text{el}} + \kappa_{\text{lat}}. \quad (2.69)$$

The electronic contribution has been discussed shortly in chapter 2.1.2 and it can be shown that the Wiedemann-Franz law can be derived from this [39]

$$\frac{\kappa_{\text{el}}}{\sigma} = LT \quad (2.70)$$

with the Lorenz number L . This explicitly showcases the interdependence of two thermoelectric performance parameters and that any change to the electronic part of the thermal conductivity has detrimental effects on the electrical conductivity and thus nullifies any influence on the figure of merit ZT . Therefore, only the lattice part κ_{lat} can be used as an optimization parameter. The lattice thermal conductivity is governed by the phonons present in the system. The number of phonons generally increases with temperature and thus a negative influence on the thermoelectric performance is received. Phonons itself can be viewed as lattice vibrations meaning that any distortion to the lattice hinders the phonon thermal transport. Hence, the principal of nanostructuring is used in the field of thermoelectrics to reduce the lattice thermal conductivity by introducing scattering centers for the phonons in the form of grain boundaries [43][26], superlattices [44][45][42], complex unit cell materials [46][42][47], and insertion of foreign atoms to the host lattice [48][49]. Nevertheless, every change to the phonon system potentially also influences the electron system by adding defects and additional scatterers and thus special care has to be taken that a reduction in lattice thermal conductivity is not outweighed by a decrease in electrical conductivity [50].

2.2.5 Figure of merit

The general dependence of the figure of merit ZT on the charge carrier density n is shown in fig. 2.3. It is revealed that insulators exhibit excellent values for thermal conductivity and Seebeck coefficient, but due to their poor electrical conductivity only small ZT values are achieved. In contrast, metals have very good electrical conductivity. However, small Seebeck coefficients and high thermal conductivities due to their high charge carrier density again lead to only small ZT values. An optimal ZT is reached for charge carrier densities of 10^{19} cm^{-3} to 10^{21} cm^{-3} [42]. This range is covered by heavily doped, degenerated semiconductors and semimetals with the latter being not suited for thermoelectrics due to compensated Seebeck coefficients. The general interdependence of the thermoelectric transport coefficients

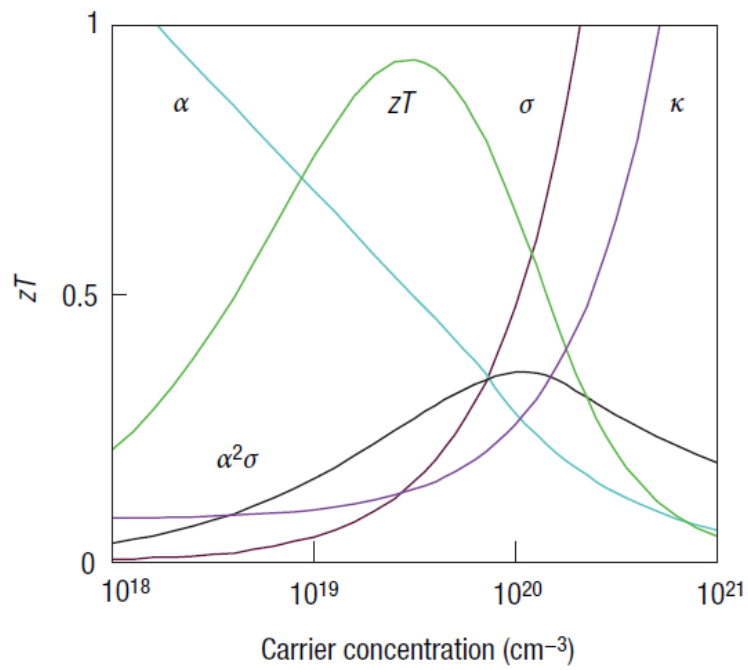


Figure 2.3: Correlation of the thermoelectric transport coefficients with respect to the charge carrier density n [42].

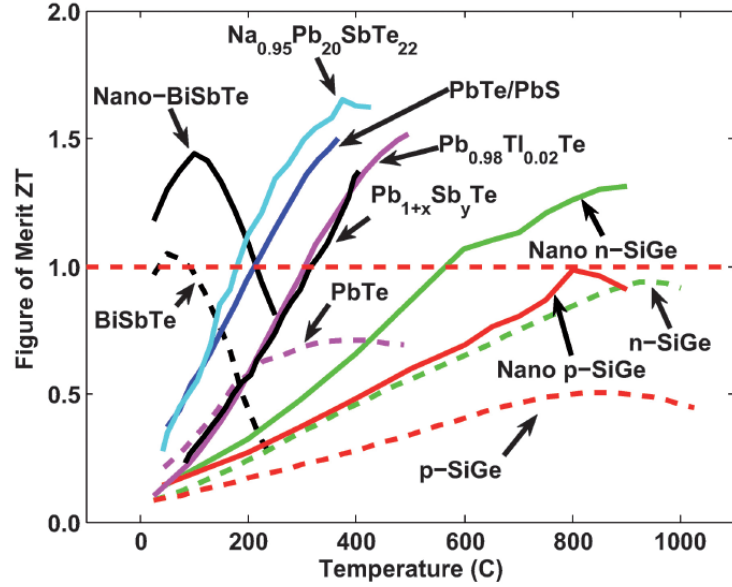


Figure 2.4: Comparison of the figure of merit for different materials [23]. Dashed lines indicate the maximum ZT for bulk state of the art materials while solid lines represent ZT values for bulk nanostructured materials.

led to a stagnation of $ZT \approx 1$ for decades [12]. In modern thermoelectrics research interest was reignited by utilizing nanostructures to e.g. effectively adopt quantum effects or decouple electronic and lattice conductivities [51]. A recent overview of different approaches to improve the figure of merit ZT can be found in [42]. A comparison of traditional bulk materials with modern bulk nanostructured materials is shown in fig. 2.4. The breakthrough with $ZT > 1$ displays the potential of the new nanostructuring approach.

2.3 The classical thermoelectric material SiGe

Caused by the interdependence of the thermoelectric transport parameters, materials only exhibit useful performances in a limited temperature range. Therefore, materials for thermoelectric modules need to be chosen with respect to the application temperature. One of the oldest and well known thermoelectric materials is the SiGe alloy with an optimal application in the high temperature region of 873 K to 1273 K [52]. Pure silicon and germanium are in principle also usable for thermoelectrics, but exhibit too high thermal conductivity to be of any practical use. An addition of only 5 at-% of Si to Ge or vice versa already lowers the thermal conductivity by

more than an order of magnitude to roughly 10 W/mK due to alloy scattering [53]. With Si and Ge being elemental semiconductors of the 4th main-group, control over the charge carrier density n is achieved by doping with elements of the 3rd and 5th main-group. Hence, the needed p-type and n-type legs for a thermoelectric module are achieved easily in this case, while n itself can be quantitatively adjusted directly via the doping density. This, combined with the evolution of advanced Si processing techniques, made SiGe to the first choice material of thermoelectric research in the past [54].

Physical properties of pure Si and Ge are summarized in table 2.1. Since Si and

Table 2.1: Properties of Si and Ge at room temperature [34][55].

	Si	Ge
crystal structure	diamond	diamond
lattice constant a	0.543102 nm	0.564613 nm
density ρ_d	2.329 g/cm ⁻³	5.323 g/cm ⁻³
atomic weight	28.09	72.6
melting temperature	1687 K	1210 K
Debye temperature Θ_D	640 K	374 K
band gap E_g	1.12 eV	0.66 eV
density of states N_C	$2.80 \cdot 10^{19}$ cm ⁻³	$1.03 \cdot 10^{19}$ cm ⁻³
density of states N_V	$2.65 \cdot 10^{19}$ cm ⁻³	$4.99 \cdot 10^{18}$ cm ⁻³
effective electron mass m_C^*	0.36 m_0	0.12 m_0
effective hole mass m_V^*	0.81 m_0	0.34 m_0
intrinsic carrier concentration n_i	$9.65 \cdot 10^9$ cm ⁻³	$2.0 \cdot 10^{13}$ cm ⁻³
intrinsic resistivity ρ_i	$3.2 \cdot 10^5$ Ω cm	46 Ω cm
thermal conductivity κ	156 W/mK	58 W/mK

Ge share the same crystal structure of face-centered diamond-cubic and have similar lattice constants, the SiGe alloy forms a completely miscible solid solution over the whole composition range (fig. 2.5). The lattice constant a of a $\text{Si}_{1-x}\text{Ge}_x$ mixed crystal then follows Vegard's law [56]

$$a_{\text{Si}_{1-x}\text{Ge}_x} = (1-x)a_{\text{Si}} + xa_{\text{Ge}}. \quad (2.71)$$

Most other properties of SiGe can also be estimated quite well by similar linear approximations of the pure elements properties.

A detailed study of the thermal and electrical properties of the SiGe alloy in dependence on the composition, doping, and temperature was carried out by Dismukes et al. [57]. Silicon-rich alloys hereby revealed better thermoelectric properties, because of a higher melting temperature and the suppression of unwanted intrinsic charge

carrier excitation due to a larger band gap. Additionally, SiGe is one of the most stable thermoelectric materials regarding its thermocyclic stability and has been proposed as a standard reference material at high temperatures [58].

Despite all the innate favorable properties of SiGe for high temperature thermoelectric application, $ZT > 1$ could barely be achieved for normal bulk SiGe. In the following, the most common approaches with respect to nanostructuring of modern thermoelectric SiGe will be presented:

- nanocrystalline SiGe

This approach tries to decouple the thermal and electrical conductivity by having grain sizes in the order of one hundred nanometer. Phonons have wave lengths matching this range and thus are scattered. In contrast, electrons' wave lengths are shorter lying in the one digit nanometer range and, accordingly, should not show any dependence [23]. Experimental implementation was often carried out by high energy ball milling of bulk SiGe to nanoparticles and subsequent sintering of those to bulk pellets [59][26]. Also the production of nanostructured SiGe by sintering of nanoparticles from gas phase synthesis has been accomplished [43].

- nanocomposite SiGe

The nanocomposite approach is in many regards similar to the nanocrystalline one as again interfaces are introduced to the system to decouple the thermal and electrical conductivity. Additionally though, further concepts like band engineering become possible due to the dependence of the band structure of the SiGe alloy on its composition. It was reported that the introduction of strained SiGe into Si can lead to the effect of modulation doping, where doped secondary Si(Ge) phases act as charge carrier donors in a SiGe matrix devoid of any impurities degrading the electrical conductivity [28][60]. Furthermore, composites of SiGe and materials of different crystal structures have been considered for thermoelectric application. Especially the combination of silicides and germanides with SiGe holds high potential for future applications [22].

- low dimensional SiGe

If the size of a thermoelectric material is reduced and approaches the nanometer length scale, it is possible for quantum-confinement to occur [24]. Distinct new physical phenomena can be experienced due to changes in the electronic density of states. Experimental realization for such structures was carried out in the form of superlattices [27], nanowires [61][62], and quantum dots [63] for SiGe. A review regarding the formation and properties of Si/Ge nanostructures

can be found in [64].

SiGe and Al

The most prominent element to achieve p-type doping for SiGe is Al. Al forms an eutectic phase diagram with Si and Ge and thus cannot be diluted completely in the SiGe system (fig. 2.5). The solubility limit of Al in SiGe is at about 0.05 at.-% depending on the composition of SiGe [66]. Practical realization of the doping process can be achieved by co-deposition of Al and SiGe (e.g. sputtering, plasma-enhanced chemical vapor deposition, molecular beam epitaxy), ion implantation of Al into SiGe, or diffusion of thin multi-layered $[\text{Al}/\text{SiGe}]_n$ systems followed by a post annealing step. In the latter case, the so called process of metal-induced crystallization is often used to assist the doping process and will be explained in the following chapter. Al as well as SiGe tend to form superficial, natural oxides when exposed to ambient air. This needs to be considered, when thinking about actual implementation of a high temperature, Al-doped, SiGe based thermoelectric module in terms of contacting and long term thermal stability. Interestingly, the Al_2O_3 oxide is chemically more stable than the SiO_2 oxide as the reduction reaction



starts to take place at temperatures higher than 800 K [67]. On the one hand this leads to a kind of buffering protection against oxidation, if a surplus of Al is present in the system, but on the other hand this also means that the comparatively few Al dopant atoms are attacked first, if diffusivity or porosity allows for contact with oxygen. Thus, special care has to be taken during high temperature exposure of the SiGe(Al) system regarding degradation by oxidization.

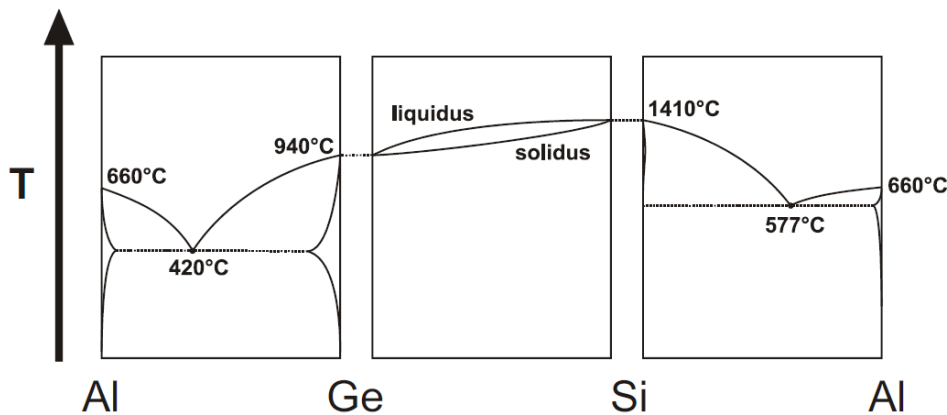


Figure 2.5: Binary phase diagrams for AlGe, SiGe, and AlSi alloys [65].

2.4 Metal-induced crystallization

The lowering of the crystallization temperature of an amorphous semiconductor in contact with a crystalline metal is known as the so called process of metal-induced crystallization (MIC) [29]. The process was first observed in 1969 by Oki et al. [68] for amorphous Ge (a-Ge) films, which crystallized at lower temperatures when being in contact with metals such as Al, Ag, Au, Cu, or Sn. Shortly afterwards, the same lowering of crystallization temperature for amorphous Si (a-Si) in contact with a metal was reported [69]. This laid the foundation for the low temperature processing of crystalline, thin film semiconductors, which are basic components for modern thin film photovoltaic applications, advanced flat panel displays, and optical data storage media [70].

Depending on the participating metal and semiconductor elements, two types of MIC processes can be differentiated [70]:

- MIC in eutectic binary systems

For this type of MIC, a eutectic phase diagram is observed for the binary metal semiconductor system. The MIC temperatures of such systems are typically lower than those of the other type. This kind of MIC is often accompanied by another process called metal-induced layer exchange (MILE), where the metal and semiconductor switch places during MIC [71]. Typical metals for this type of MIC include Al, Au, Ag, and Bi in contact with a-Si or a-Ge.

- MIC in compound-forming binary systems

For binary systems of metal and semiconductors forming a silicide or germanide compound, the second type of MIC can be observed. The MIC temperatures range from intermediate reductions close to the crystallization temperature of the pure semiconductor. As this process is mediated by a chemical reaction front of the formed compound, the so called side process of metal-induced lateral crystallization (MILC) can often be realized to form thin films with a preferred crystallization direction lying in plane of the thin film semiconductor [72]. Typical metals for this type of MIC include Ni, Pd, Pt, and Cu in contact with a-Si or a-Ge.

A short overview discussing the properties of the MIC process of the most important metals in conjunction with a-Si or a-Ge can be found in [73] and [74], respectively. Of course, a mixture of MIC capable elements can be utilized simultaneously in one system, but the metal with the lowest MIC temperature present would crystallize the amorphous semiconductor before metals with higher MIC temperatures would start to have an effect. Therefore, the only extension beyond binary systems until now was

to use Si and Ge concurrently in the form of amorphous SiGe alloys in contact with one metal [75][76][65].

It is empirically known that nature strives to always attain the state of lowest energy. Applying this to the case of a semiconductor, the amorphous state is less desirable because of its intrinsically higher Gibbs energy compared to the crystalline state caused by the lattice atoms interaction via the Lennard-Jones potential [38]. Nevertheless, not all semiconductor material exist in the crystalline state due to energy barriers preventing the transition from the amorphous to the crystalline state as interface energies have to be surmounted during the nucleation of a crystal germ. In the case of a-Si and a-Ge the rearrangement of the atoms is hindered by the strong covalent bonds between the semiconductor atoms (2.30 eV for Si-Si, 1.95 eV for Ge-Ge [77]). Thus, the activation energy for crystallization of pure a-Si and a-Ge can only be reached at high temperatures of 973 K and 573 K, respectively [78]. The so called phenomenon of Coulomb screening is capable of weakening the strong covalent semiconductor bonds and appears when a metal is brought in contact with a semiconductor. The wave function of the free electron gas of the metal extends into the adjacent semiconductor and such is able to partially screen the covalent bonds there. As this phenomenon is of very local nature, the metal-induced weakening has been estimated to be only effective at an interfacial layer of about 2 monolayers (ML) thickness [79]. If now a non compound-forming, eutectic binary system is assumed, the semiconductor atoms affected by metal-induced bond weakening exhibit greatly enhanced mobility as long as they stay in the metal's screening range and are therefore likely to initiate the crystallization process at the semiconductor-metal interface directly or along grain boundaries of the metal. Which of these processes is preferred, depends on the balance between bulk Gibbs energy reduction and emerging surface/interface energies during the transformation process.

In the case of Al as catalyst metal, the process of MIC is also known specifically as aluminum-induced crystallization (AIC). For Si/Al systems, the metal grain boundary mediated crystallization turns out to be the preferred mechanism. The involved interface and surface energies during the AIC process are highlighted in fig. 2.6(a). As the diffused a-Si is on both sides in contact with Al during AIC, the total thickness of the interfacial layer of metal-induced bond weakening is doubled to 4 ML. This result could be proven theoretically by Wang et al. [80]. In fig. 2.6(b), this theory was related to experimental results regarding the critical Si thickness $l_{\text{Si}}^{\text{critical}}$ for which the AIC process can be initiated along an Al grain boundary. For thick enough Al layers, $l_{\text{Si}}^{\text{critical}}$ turns out to be 4 ML as was predicted by theory. If the Al is too thin, the metal-induced bond weakening effect diminishes and a deviation to $l_{\text{Si}}^{\text{critical}} > 4 \text{ ML}$ accompanied by an increase of the resulting MIC temperature is obtained. Experimental verification of this solid state, diffusion process model was achieved by in-situ valence energy-filtered transmission electron microscopy during annealing of Si/Al systems [81].

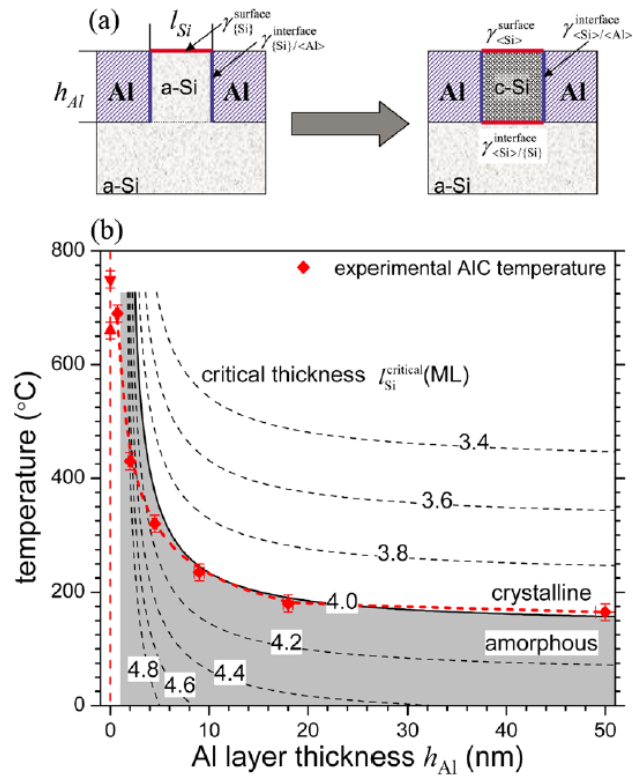


Figure 2.6: (a) Schematic representation of the occurring interface energies during the MIC process of a-Si along Al grain boundaries. (b) Dependence of the MIC temperature on the metal layer thickness in the Si/Al system [80].

3 Experimental Techniques

3.1 Sputter deposition for thin film approach

Deposition of thin films can be accomplished via utilization of sputtering [82]. Particles of a solid target material are ejected during the sputtering process by bombardment of the target with energetic particles. The incident particle transfers its momentum and energy to the solid's lattice by a cascade collision, which leads to breaking bonds in the solid and thus enables particles to leave the targeted solid through the transferred recoil. In conventional sputtering machines, the energetic particles are provided as ionized gas atoms (i.e. Ar, Xe). These are created by applying a negative high voltage to the target cathode, which accelerates naturally occurring free electrons. These then can ionize gas atoms by impact ionization resulting in a cascade of ionized gas atoms and thus a plasma. As enough time in between the collisions is needed to accelerate to sufficient energies for impact ionization, sputtering machines are operated at pressures in the range of 10^{-3} mbar to 10^{-1} mbar. The positively charged gas ions are then themselves accelerated by the applied negative high voltage towards the target and create a collision cascade in the target. If the energy of the incident ion is high enough, surface atoms of the target can be ejected due to recoil as shown in fig. 3.1. The substrate for thin film deposition is placed facing toward the target such that the ejected target particles are moving directly towards it and condensate there.

In the case of magnetron-sputtering, additional concentric, permanent ring magnets are placed behind the target. These force the accelerated electrons onto spiral curves above the target and a locally increased ionization rate resulting in a torus shaped plasma is achieved. The sputtering rate is therefore locally greatly increased and leads to preferential erosion in the form of typical sputtering trenches in the target. To prevent erosion of side parts of the sputtering source, the cathode is shielded except for the target. Heating of the target due to the collision cascades of the incident ions needs to be compensated by water cooling.

Sample preparation

The samples of this study were prepared in two different magnetron sputtering systems. A $\text{Si}_{80}\text{Ge}_{20}$ -alloy target (99.99%) and an Al-target (99.999%) were utilized in both cases for deposition of the individual layers. Thickness of individual layers was controlled via sputtering power and time.

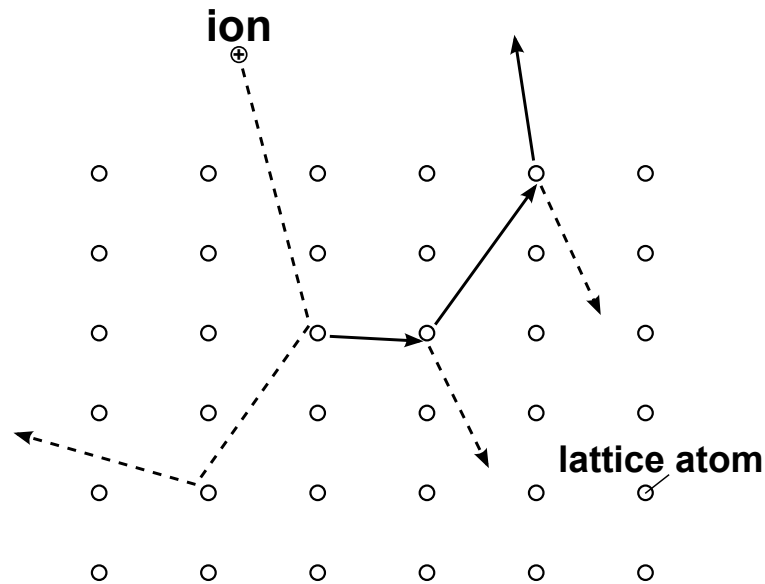


Figure 3.1: Cascade collision in a solid target caused by an incident ion.

All samples consisting of SiGe/Al multilayers were produced by the company *Oerlikon* (now *Evatec*) in Balzers, Liechtenstein. The Si₈₀Ge₂₀-alloy target was run in a DC-sputtering source with a power of 750 W and the Al-target in a RF-sputtering source at 250 W. The target-substrate distance was 130 mm. Ar was used as process gas with a flow of 100 sccm and 35 sccm, respectively.

All samples deposited in the form of SiGe/Al bilayers or SiGe/Al/SiGe trilayers were prepared with the sputter system *PLS 500* at the University of Augsburg. For this system, both targets were run with DC-sputtering sources at a power of 25 W. A flow of 30 sccm Ar was used during deposition resulting in a working pressure of 3 mbar. Contamination of the sputter targets regarding oxidation was reduced by pre-sputtering before actual deposition until stable voltage and current conditions were achieved. Substrates were cleaned for 10 min each in ethanol, isopropanol, and distilled water prior to deposition.

3.2 Secondary Neutral/Ion Mass Spectrometry

The effect of sputtering can also be utilized for quantitative elemental analysis of thin films samples by using the sample as the target for the sputtering process. The ejected particles then need to be analyzed with mass spectrometry to identify them regarding their elemental composition. The methods of Secondary Neutral Mass Spectrometry (SNMS) and Secondary Ion Mass Spectrometry (SIMS) emerged as

the two main investigation methods with in principle their only difference being in analyzing neutral or ionized emitted particles from the sample's sputtering process. A comprehensive introduction to the basic principles of SNMS and SIMS can be found in [83][84].

Experimental details

SNMS measurements were conducted at the University of Debrecen (Hungary) by G. L. Katona. A RF Ar plasma was used for extraction of Ar^+ ions for direct bombardment of the samples. A bias of 350 V using a 100 kHz square signal generator with a duty cycle of 80% was applied in all cases to avoid charging.

SIMS measurements were performed by H. Karl at the University of Augsburg. Cs^+ ions were used as incident particles under an angle of incidence of 60° . The detected ionized isotopes for each element were $^{27}\text{Al}^-$, $^{29}\text{Si}^-$, and $^{74}\text{Ge}^-$.

3.3 Rutherford Backscattering Spectrometry

Rutherford backscattering spectrometry (RBS) is a process for material analysis. It utilizes the elastic recoil of projectile ions at the nuclei of the sample's atoms to gather information about the sample's depth-resolved elemental composition. If projectile ions of mass M_1 and energy E_0 collide with a sample's nucleus of mass M_2 , elastic scatter processes under the laws of momentum and energy conservation will result in the recoil of the projectile ions under the angle θ with the energy E_1 . The kinematic factor K then follows as [85]

$$K = \frac{E_1}{E_0} = \left[\frac{(M_2^2 - M_1^2 \sin^2 \theta)^{1/2} + M_1 \cos \theta}{M_1 + M_2} \right]^2. \quad (3.1)$$

If the scattered ions are detected regarding their energy E_1 under a fixed angle θ while knowing E_0 and M_1 , it is possible to evaluate M_2 and therefore examine the sample's elemental composition. Best measurement resolution is obtained for angles θ close to 180° . The measurement principle of RBS is illustrated in fig. 3.2.

Equation (3.1) only holds for the projectile ion energy E_1 , if the scattering atomic nucleus is located at the sample's surface. For scattering processes with atoms inside the sample, another energy loss due to the Coulomb interaction of the projectile ions with the valence electrons of the sample's atoms has to be considered. This additional energy loss being dependent on the traveled distance of the projectile ion in the sample enables the depth-resolved analysis of the measured RBS spectra.

These depth dependent energy losses explain the occurrence of broadened peaks in the form of plateaus instead of sharp lines at the energy $E_0 K_{\text{element}}$ for each element.

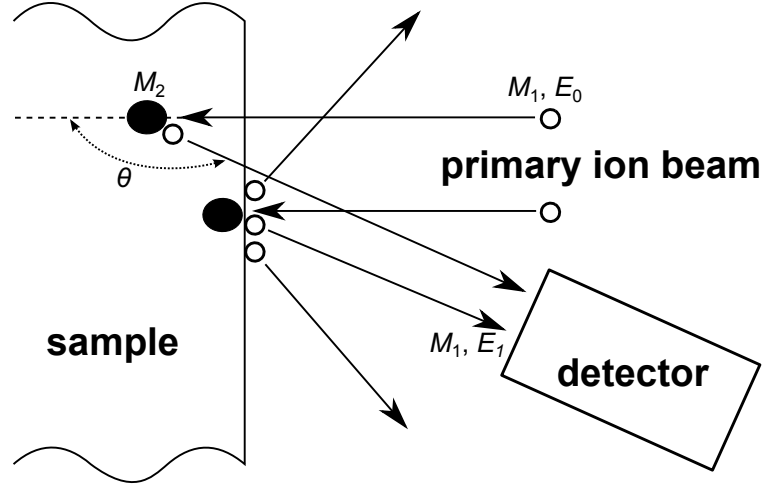


Figure 3.2: Schematic of the RBS measurement principle.

Analysis of the RBS spectra is generally done with simulation programs, which compute the atomic areal density N_a for each element by calculating the differential cross section in the lab system [85]

$$\frac{d\sigma}{d\Omega} = \left(\frac{Z_1 Z_2 e^2}{2E \sin^2 \theta} \right)^2 \frac{\left(\left\{ 1 - [(M_1/M_2) \sin \theta]^2 \right\}^{1/2} + \cos \theta \right)^2}{\left\{ 1 - [(M_1/M_2) \sin \theta]^2 \right\}^{1/2}}, \quad (3.2)$$

where E is the energy of the projectile ion and Z_1 and Z_2 are the atomic numbers of the projectile ion and the sample's atoms, respectively. The areal density N_a can be used to calculate the thickness d of a layer if its atomic density N is known

$$d = \frac{N_a}{N} = \frac{M_{\text{mol}} N_a}{\rho_d N_A} \quad (3.3)$$

where M_{mol} and ρ_d are the molar mass and mass density, respectively, and N_A is the Avogadro constant. The values of M_{mol} and ρ_d of the utilized elements are summarized in table 3.1.

Experimental details

The RBS measurements were conducted on the Tandem-Ion-Accelerator, HVEE (High Voltage Engineering Europe B. V.) at the University of Augsburg. Singly charged He ions (He^+) with an energy of 1.7 MeV were utilized as projectile ions.

Table 3.1: Mass density ρ_d and molar mass M_{mol} of the utilized elements [86].

element	ρ_d (g/cm ³)	M_{mol} (g/mol)
Si	2.33	28.09
Ge	5.90	72.61
Al	2.71	26.98

The detector had an energy resolution of 1.62 keV and detected ions under a scattering angle θ of 170° and a solid angle Ω of 1.08 msr. Simulation of the RBS spectra was carried out via the simulation program *SIMNRA* [87].

3.4 X-ray Diffraction

X-ray diffraction (XRD) is a measurement technique for structural analysis of materials. Atoms in a solid can act as local scattering centers for x-rays. If such atoms exhibit long-range ordering like in a crystalline material, constructive interference between the x-rays becomes possible. The so called Laue condition

$$\exp\left(i(\vec{K}' - \vec{K}) \cdot \vec{G}\right) = 1 \quad (3.4)$$

is the prerequisite and reveals that the difference between the diffracted and incident beam $(\vec{K}' - \vec{K})$ needs to be equal to a reciprocal lattice vector \vec{G} . An equivalent formulation is the Bragg-equation

$$n\lambda = 2d_{hkl} \sin(\theta_{hkl}), \quad (3.5)$$

which correlates the wave length λ of the incident x-rays to the lattice plane distance d_{hkl} of the crystalline material [88] as shown in fig. 3.3. A maximum in intensity of reflected x-rays is observed for the diffraction angle θ_{hkl} , if the path difference of x-rays diffracted at different, parallel lattice planes is an integral multiple of the wave-length λ . For cubic lattices like the diamond structure of SiGe, a linear relationship between the lattice plane distance d_{hkl} and the lattice constant a

$$d_{hkl} = \frac{a}{\sqrt{h^2 + k^2 + l^2}} \quad (3.6)$$

exists. Hereby, the Miller indices h, k, l indicate the lattice plane orientation. Crystallographic data of the crystalline systems investigated in this work is summarized in table 3.2.

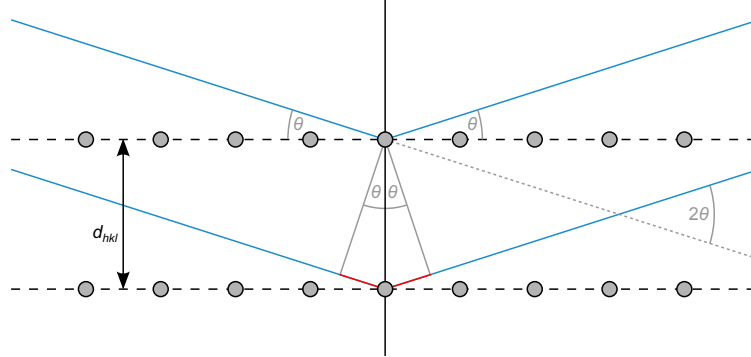


Figure 3.3: Schematic of Bragg-reflection for x-rays at lattice planes. The path difference of the lower x-rays is highlighted in red.

Apart from information regarding the crystal structure of a sample, XRD measurements can also be used to evaluate the grain size. The so called Scherrer formula [89]

$$\Delta(2\theta) = \frac{\lambda}{\cos(\theta)L} \quad (3.7)$$

hereby can be interpreted to identify the perpendicular coherence length L with the averaged grain size L_{gr} perpendicular to the reflecting lattice plane. This formula ignores contributions due to stress in the observed XRD patterns, which often itself are subject of XRD measurements on thin films [88]. Therefore, this approach should only be treated as a rough estimation for the grain size.

Experimental details

The XRD measurements were conducted on a *XRD 7* and a *XRD 3003 PTS* diffractometer of *Seifert* in para-focusing Bragg-Brentano-geometry as $\theta-2\theta$ -measurements. A copper cathode was used in both cases for x-ray generation. For the *XRD 7* a Ni-absorber was used as a filter, while Goebel-mirrors [91] were used for the *XRD 3003 PTS*, such that for both cases the Cu- K_{α} -doublet-line (1.5405 Å) could be utilized. Background subtraction and Rachinger correction (subtraction of the Cu- $K_{\alpha,2}$ -line) were carried out by the software *Rayflex*.

Additional in-situ x-ray diffraction measurements were performed during thermal annealing up to 1123 K at 3 K/s in a purified He atmosphere at beamline X20C of the National Synchrotron Light Source (Brookhaven National Laboratory, USA) by S.

Table 3.2: Crystallographic data [90].

Element	hkl	Diffracting angle 2θ (deg.)		Relative intensity
		$\lambda = 1.5405 \text{ \AA}$	$\lambda = 1.797 \text{ \AA}$	
Al	111	38.4721	44.8779	100
	200	44.7384	52.1875	47
	220	65.1334	75.9784	22
Si	111	28.4422	33.1780	100
	220	47.3023	55.1783	55
	311	56.1205	65.4648	30
Ge	111	27.2832	31.8249	100
	220	45.3049	52.8484	57
	311	53.6815	62.6197	39
Si ₈₀ Ge ₂₀	111	28.2112	32.9085	100
	220	46.9036	54.7133	55
	311	55.6342	64.8975	32

Raoux (Helmholtz-Zentrum Berlin, Germany). The XRD setup is equipped with an in-situ BN heater stage and the intensity of the XRD peaks is detected by a fast linear diode array detector that monitors the intensity of the XRD peaks over a 2θ range of 15° . The center of the detector was located at $2\theta = 31^\circ$, which allowed the detection of the SiGe(111) XRD peak at $2\theta = 33^\circ$ for the applied x-ray wavelength of 1.797 \AA during these measurements.

3.5 Electron Microscopy

Electron microscopes utilize accelerated electrons as source of illumination [92]. The wavelength of the electrons is tunable by changing the acceleration voltage and can reach wavelengths of several orders below conventional light. Thus, increased resolution can be achieved regarding the Abbe limit. Lenses of electron microscopes are built in the form of magnetic pole shoes to guide and collimate the electron beam to the desired sample spot. Concerning the used geometry of interaction between the incident electron beam and sample, the two principle cases of Scanning Electron Microscopy (SEM) and Transmission Electron Microscopy (TEM) can be differentiated.

3.5.1 Scanning Electron Microscopy

In the case of SEM, the electron beam is guided in a scanning pattern across the sample's surface [93]. The accelerated electrons interact with the surface near sample's atoms and produce secondary electrons (SE) and x-rays in the process. These SE can be detected by applying another acceleration voltage to the detector such that the SE are guided to it. The signal detected is dependent on the composition of the sample, electrical charges and the relative topography of the sample's surface to the detector alignment. The signal in the end is illustrated in gray-scale, while brighter regions indicate regions of higher SE yield.

3.5.2 Transmission Electron Microscopy

In contrast to SEM, where the incident electron beam of electrons creates detected SE, the electron beam is transmitted through the sample for TEM and the incident primary electrons are detected [94]. Therefore, TEM samples need to be prepared to thicknesses below 100 nm, because otherwise transmission of the electron beam would be impaired by interactions reducing the intensity. Only elastically scattered electrons are used for TEM as apertures are utilized to filter out inelastically scattered electrons. If TEM is conducted in the so called bright field (BF) mode used in this study, mainly two contrasts can be observed. First, the mass-thickness-contrast originates from the electrons' interaction with the sample's atoms. Regions of heavier atoms show increased interaction due to the Rutherford cross-section discussed in chapter 3.3 (mass-contrast), while thicker regions just scatter the electron beam stronger due to more scatterers being present (thickness-contrast). Apertures and the electron beam are aligned in BF mode to only account for directly transmitted electrons such that areas affected by the before mentioned contrast appear darker in the resulting image. Second, the so called diffraction contrast can also be observed in TEM and stems from diffraction of the electron beam at crystalline sample areas. Hence, the direction of the incident electron beam can also be changed by diffraction comparable to beam interactions discussed for XRD in chapter 3.4. This contrast can be used to image lattice planes in high resolution. All former image information is obtained when focusing on the image plane and thus leads to images of the actual real space. If the focus of the lens system is shifted to the diffraction plane, a diffraction image holding information about reciprocal space is obtained. Single crystalline samples exhibit spot-like reflexes arranged in a periodical pattern, while polycrystalline samples reveal concentric rings as diffraction images. If the underlying lattice structure of the sample is known, the lattice plane distance can be extracted from TEM diffraction images. Amorphous samples reveal strongly blurred rings in TEM diffraction images [95].

3.5.3 Energy Dispersive X-ray Spectrometry

As accelerated electrons interact with the sample, it is possible for electrons of the sample's atoms to be ejected from their respective atomic shell states by collision. If electrons are kicked out from inner shell states, electrons from higher energy states are able to drop into the lower, free energy states under emission of element specific radiation. This characteristic x-ray radiation can be used to qualitatively and quantitatively analyze samples regarding their elemental composition locally, if being detected for example by a semiconductor-detector regarding their energy, hence the name Energy Dispersive X-ray Spectrometry (EDX). The spatial resolution limit for this method lies in the range of μm for conventional SEM-EDX measurements and in the order of nm for TEM-EDX. The lower resolution for SEM-EDX stems from the raindrop like shape of interaction volume of the accelerated electrons below the sample's surface, while TEM samples are thinned out so much that basically only the area of the incident electron beam is of importance for the resolution. The detected EDX signals of every measurement area can be arranged graphically to create a elemental distribution map of the whole scanned sample area, which is called elemental mapping [95].

Experimental details

The SEM imaging was performed on a microscope of the type *Nova 200 NanoSEM* of *FEI Company*. The maximum acceleration voltage for the incident electron beam was 18 keV. Detection of the SE was carried out by a "through the lens"-detector. Imaging via TEM was partly conducted at the Universities of Chemnitz and Augsburg. In Chemnitz, a microscope of type *Philips CM20 FEG* was used, while a *JEOL 2100 F* was used in Augsburg. The acceleration voltage for the electrons in both cases amounted to 200 keV. Incident electrons were detected with a CCD-camera normally, while selected images were recorded by image plates due to better resolution.

3.6 Resistance measurement

The electrical resistivity ρ is measured in van der Pauw geometry [96]. The van der Pauw method can be used for continuous thin film samples of arbitrary shape and known thickness d . The basic geometry for a van der Pauw measurement is shown in fig. 3.4. The sample is contacted at the edge with four point contacts, where a current I_{AB} is sent through contacts A and B, while the voltage drop U_{CD} is measured between the contacts C and D. With this, the pseudo resistance $R_{AB,CD}$ can be calculated

$$R_{AB,CD} = \frac{U_{CD}}{I_{AB}}. \quad (3.8)$$

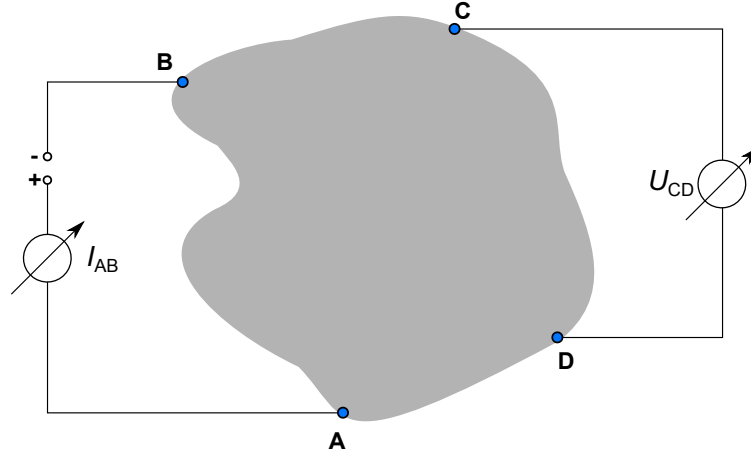


Figure 3.4: Basic geometry for a van der Pauw measurement to obtain the pseudo resistance $R_{AB,CD}$ of a continuous thin film sample of arbitrary shape by passing a current I_{AB} through contacts A and B while measuring the voltage drop U_{CD} between C and D.

Cyclical rotation of the contacts leads to another pseudo resistance $R_{BC,DA}$, for which the following relationship is valid

$$\exp\left(-\frac{\pi d}{\rho} R_{AB,CD}\right) + \exp\left(-\frac{\pi d}{\rho} R_{BC,DA}\right) = 1. \quad (3.9)$$

As this expression cannot be solved analytically, an approximation in the form of

$$\rho = \frac{\pi d}{\ln 2} \cdot \frac{R_{AB,CD} + R_{BC,DA}}{2} f \quad (3.10)$$

is made, where f is a correction factor. This correction factor itself is related to the ratio of the pseudo resistances as

$$\cosh\left(\frac{R_{AB,CD}/R_{BC,DA} - 1}{R_{AB,CD}/R_{BC,DA} + 1} \cdot \frac{\ln 2}{f}\right) = \frac{1}{2} \exp\left(\frac{\ln 2}{f}\right) \quad (3.11)$$

and the numerical approximation is shown in fig. 3.5. Then equation (3.10) can be used to calculate the resistivity ρ , if the thickness d of the sample is known.

Experimental details

The resistance measurements were carried out on the home built "HTS" system, which is presented in detail in [97][98]. Samples of size $(10 \times 10) \text{ mm}^2$ are used and directly placed on top of a copper block connected to a heating stage. The four contacts to the

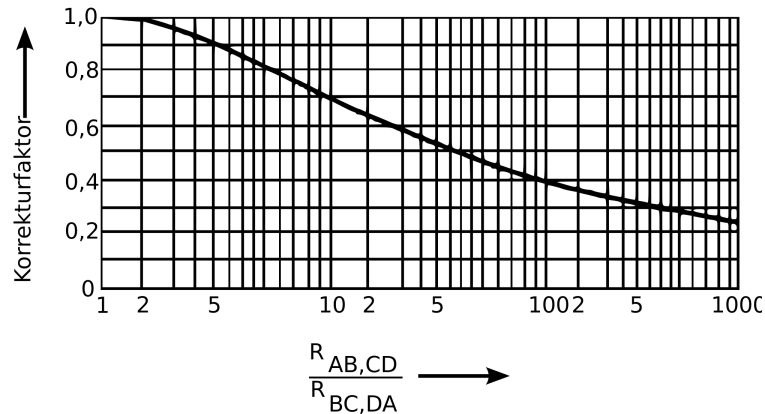


Figure 3.5: Numerical approximation for the correction factor f in van der Pauw measurements [96].

sample are realized as tungsten springs pressing on the sample's corners. Additionally, a thermocouple type-K is also placed in direct contact to the sample's surface to measure the temperature of the sample during the heating process. Temperatures between room temperature and 723 K can be reached at heating/cooling rates of up to 30 K/min. In this work, heating/cooling rates were chosen to be 2 K/min. The setup is placed in a recipient, which can be pumped down to pressures of $p < 10^{-6}$ mbar to prevent oxidation of the sample. The recipient is flooded with nitrogen up to $p \approx 10$ mbar to enable thermal coupling via nitrogen. A switch box system measures all 4 cyclical rotations of the pseudo resistances while also inverting the current flow for each, giving in total 8 measurements per measurement step. A maximum current of 1 mA is applied to the sample. If the maximal compliance voltage of 12 V is not sufficient to drive the current through the sample, the current is halved until the needed compliance voltage drops below 12 V. The minimum current needed for reliable measurements with respect to leakage currents lies in the range of 100 nA.

3.7 Hall Effect measurement

The van der Pauw geometry cannot be only used to determine the resistance of a thin film sample, but also bears the possibility to gather information about the charge carrier density n . The Hall effect [99] needs to be utilized for this by applying a magnetic field \vec{B} perpendicular to the surface of the sample in addition to the normal van der Pauw geometry (cf. fig. 3.6). If a current I_H is passed through contacts A and C, then the Hall voltage U_H can be measured between contacts B and D due to the Lorentz force

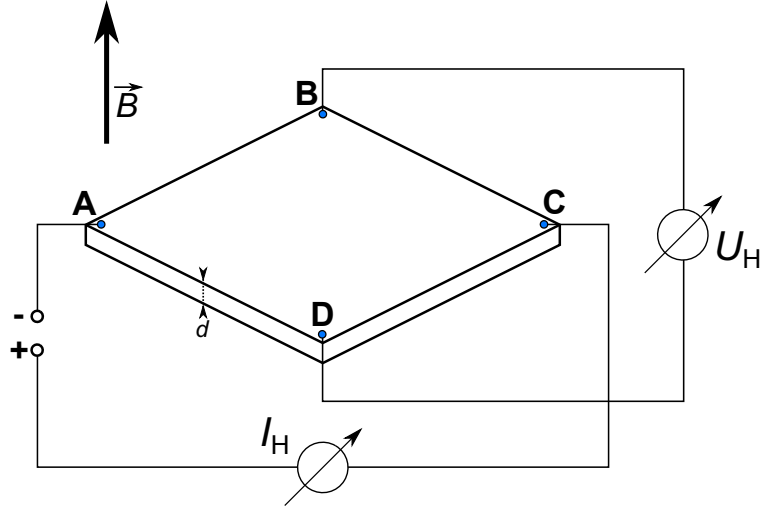


Figure 3.6: Hall measurement in van der Pauw geometry.

$$\vec{F}_{\text{Lor}} = q \cdot \vec{v}_d \times \vec{B} \quad (3.12)$$

with \vec{v}_d being the drift velocity of the charge carriers. This leads to a shift of charges, which builds up a compensating electric field $\vec{\mathcal{E}}_H$

$$q\vec{\mathcal{E}}_H = q \cdot \vec{v}_d \times \vec{B}. \quad (3.13)$$

As only parts perpendicular to

$$\vec{v}_d = \frac{1}{qn} \cdot \vec{J}_{\text{el}} \quad (3.14)$$

contribute to the charge shift, a measurement geometry with perpendicular arrangement of contacts \overline{AC} and \overline{BD} is preferred. Under these conditions, the measured Hall voltage follows as

$$U_H = - \int_D^B \vec{\mathcal{E}}_H \cdot (d\overline{BD}) = - \int_D^B \frac{BI_H}{qnd\overline{BD}} \cdot (d\overline{BD}) = \frac{BI_H}{qnd}. \quad (3.15)$$

The charge carrier density n then equals

$$n = \frac{BI_H}{qdU_H} = \frac{1}{qR_H}, \quad \text{with} \quad R_H = \frac{d}{B} \frac{U_H}{I_H} \quad (3.16)$$

being the Hall constant R_H . Combination of a resistivity and charge carrier density measurement enables evaluation of the charge carrier mobility μ by equation (2.51).

Experimental details

The Hall measurement setup is home built and operates at ambient conditions. Magnetic fields in the range of -0.8 T up to 0.8 T are supplied by a Helmholtz coil. Maximum currents I_H of 2 mA were used. As no perfect perpendicular alignment between \overline{AC} and \overline{BD} can be expected and even small fluctuations in the surface temperature of the sample can result in distinctive parasitic voltage drops during a Hall measurement when characterizing thermoelectric materials, the contacts for current supply and voltage measurement were cyclically rotated and also inverted regarding the current flow with a switch box system. The inverted measurements were used to extract only the symmetric part of the U_H measurement, because asymmetric contributions are due to parasitic effects. The averaged symmetric contributions of U_H/I_H then were plotted against the magnetic field strength B to calculate the charge carrier density n from the linear slope using equation (3.16).

3.8 Seebeck measurement

Seebeck measurements at first sight seem to be straight forward as only voltages and temperatures need to be measured to determine $S = dU/dT$ (compare eq. (2.28)). In practice though, special care has to be taken for example to ensure that the thermal voltages and temperatures are measured at the same sample spot without too much time delay and any parasitic voltage influences. Important measurement aspects especially for thin films are discussed in [100]. In the following, the influence of measurement conditions on the obtained Seebeck coefficients shall be discussed exemplarily for the case of the measurement setup used for this study, operated at different base pressures of below 10^{-6} mbar and at 10^1 mbar.

The "HTS" system was designed to operate at pressures below 10^{-6} mbar to prevent oxidation of samples during high temperature exposure. Participation in the round robin test for electrical conductivity and Seebeck measurements on thin films of the *NanoCaTe* project led to the discovery that the Seebeck values measured with our "HTS" system are underestimated by 20% to 25% in absolute value. Investigations revealed that the thermal coupling to the sample was of poor quality and thus a discrepancy between actual and measured temperature at the two probing spots of the Seebeck sample occurred when measuring under vacuum. This is highlighted for a Seebeck measurement in fig. 3.7a) where the Seebeck voltages U_{NiCr} and U_{Ni} measured across the NiCr and Ni legs of the type K thermocouples are shown. After the initial heating pulse generated a temperature difference of 8 K across the Seebeck sample, a linear relaxation for the Seebeck voltages is observed with decreasing temperature difference as expected. During this relaxation, the "HTS" was being evacuated starting from atmospheric pressure. When a pressure of $p < 10^{-3}$ mbar was reached for $\Delta T < 3.5$ K, a change in slope was observed for the measured Seebeck voltages. This

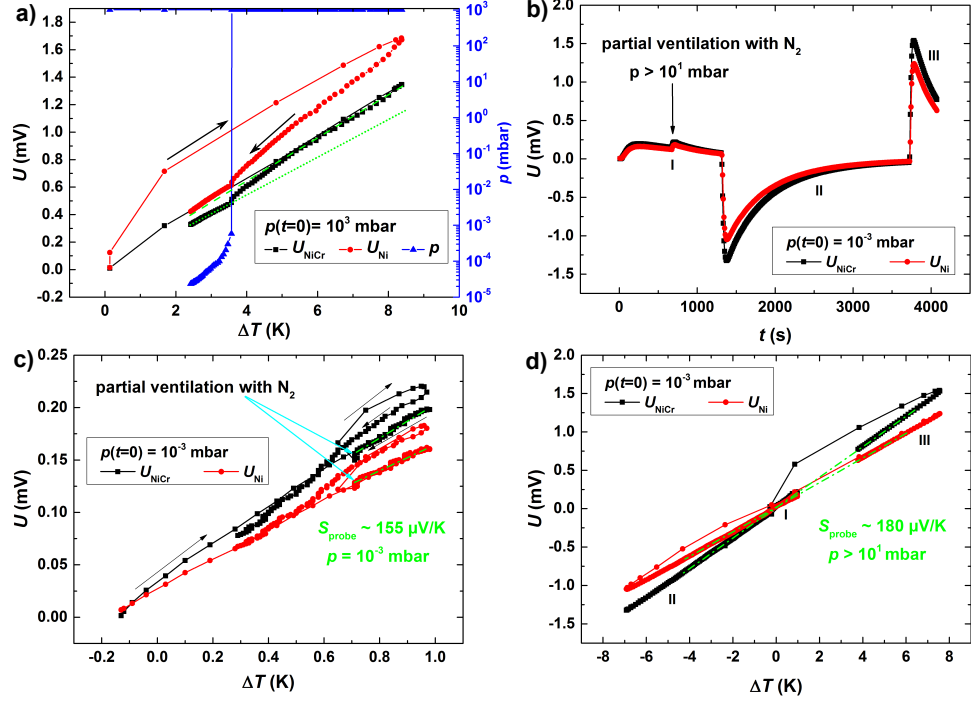


Figure 3.7: Seebeck measurements performed on a typical thermoelectric sample at room temperature showing the Seebeck voltages measured across the NiCr and Ni legs of the type K thermocouples. a) Seebeck voltage measurement starting at atmospheric pressure followed by pumping the system. A change in slope of the Seebeck voltages is observed during pumping and guides to the eyes are added for the different slopes in form of a dashed and dotted green line for the values of U_{NiCr} . Please note that the read out for pressure values is only available for pressures of $p \leq 10^{-3}$ mbar and otherwise the pressure is set to $p = 10^3$ mbar. b) Seebeck measurement starting at $p = 10^{-3}$ mbar. During the first interval, the recipient was partially vented with N_2 . c) Plot of $U - \Delta T$ for only interval I and d) for all 3 intervals of the measurement shown in b). The respective linear plots for calculation of the Seebeck coefficient before and after ventilation are illustrated as dashed green lines.

clearly showcases the underestimation of the Seebeck coefficient caused by the poor thermal coupling of the sample to its environment, if no ambient gas is present. A similar behavior could be observed, if a Seebeck measurement was started at lower pressure and ventilation with dry N_2 was conducted during the measurement process. This is shown in fig. 3.7b) at the beginning of the measurement (interval I), when a sudden change in the measured Seebeck voltages to higher values is observed at the starting point of ventilation. This change to higher Seebeck voltages again indicates that the sample was not in equilibrium with its environment in the evacuated state. The ambient gas improved the thermal coupling to the sample and thus the temperature difference along the Seebeck voltages increased in value. This can also be observed at the point of ventilation in fig. 3.7c). The different slopes of dU_{Ni}/dT before and after ventilation are highlighted in fig. 3.7c) and d) as dashed green lines. In the evacuated state, a Seebeck coefficient of $155 \mu V/K$ is measured for the sample, while a Seebeck coefficient of $180 \mu V/K$ is measured when the sample is exposed to N_2 atmosphere. This correlates to the observed underestimation of 20% to 25%. All Seebeck measurements presented in this study **up to chapter 4.2** were carried out in the "HTS" system operating at $p < 10^{-6}$ mbar and hence are underestimated by 20% to 25%. As this systematic error was constant in value no further measurements were repeated in N_2 atmosphere. Seebeck measurements **presented onwards from chapter 4.3** were carried out at $p \approx 10^1 - 10^2$ mbar in dry N_2 atmosphere.

Experimental details

Seebeck measurements were also performed on our home built "HTS" system. Seebeck samples of size $(2 \times 10) \text{ mm}^2$ are placed along a slit between two copper blocks, which can be heated separately to generate a thermal gradient along the Seebeck sample. Thermocouples type-K are fed through a recess area in the copper blocks, where they are fixed in position with a high temperature resistant, electrically insulating glue. The Seebeck sample is directly placed face down on the joints of the thermocouples. A switch box system is used to measure the thermal voltages generated by each thermocouple pairing corresponding to the sample's local surface temperature as well as the Seebeck voltages generated by the thermal gradient along the sample by connecting the respective same legs of each thermocouple. This ensures that the temperature and Seebeck voltage measurements are taken at the same respective sample spot. The actual Seebeck measurement is performed in a quasi-steady-state by applying alternating temperature gradients [101]. This is achieved by alternating every 15 min between one heater holding the applied temperature constant and the other changing its output power to increase or decrease the applied temperature continuously during a heating or cooling cycle, respectively. Heating rates are chosen as 2 K/min. The sample's temperatures and Seebeck voltages are recorded approximately every 5 seconds and the Seebeck coefficient is calculated using equation (2.28) from the slope

of the measured Seebeck voltages versus applied temperature difference at the thermocouples for each time period. Seebeck measurements were - as explained earlier - taken at pressures below $< 10^{-6}$ mbar or at 10^1 mbar of dry N_2 atmosphere.

3.9 Thermal conductivity measurement

Thermal conductivity measurements of thin films are not trivial, because the little amount of material to measure makes typical steady-state methods for bulk materials unreliable as a steady heat flow through the thin film cannot be guaranteed. Specialized methods for thin films like the so called 3ω -method requiring sophisticated measurement geometries and delicate time-resolved voltage measurement have emerged. The 3ω -method is used to measure the thermal conductivity κ of bulk materials (solid, liquid) and also thin films [102]. A thin metal strip/wire is deposited onto the thin film sample on top of an added isolation layer and acts as an AC-heater (fig. 3.8 a)). If an AC-current

$$I(t) = \Delta I \cdot \cos(\omega t) \quad (3.17)$$

of the current amplitude ΔI and frequency ω is applied to the metal strip, a time dependent voltage

$$U(t) = R(t) \cdot I(t) \quad (3.18)$$

following Ohm's law can be measured. This current leads to Joule heating of the metal strip, where a temperature oscillation

$$T(t) = T_0 + \Delta T \cdot \cos(2\omega t + \phi) \quad (3.19)$$

around T_0 with temperature amplitude ΔT , doubled frequency 2ω , and a phase shift ϕ depending on the underlying sample can be observed. The doubling of the frequency is due to both polarizations of the current contributing equally to the Joule heating. The temperature oscillation infers a resistance change

$$R(t) = R_0 [1 + \alpha_R \cdot T(t) - T_0] = R_0 + \Delta R \cdot \cos(2\omega t + \phi) \quad ; \quad \Delta R = \alpha_R \cdot R_0 \cdot \Delta T. \quad (3.20)$$

Hereby, α_R is the temperature coefficient of the resistance of the metal strip. Inserting equations (3.17) and (3.20) into (3.18) leads to

$$\begin{aligned} U(t) &= [R_0 + \Delta R \cos(2\omega t + \phi)] \cdot \Delta I \cdot \cos(\omega t) \\ &= R_0 \Delta I \cos(\omega t) + \frac{\Delta R \Delta I}{2} \cdot [\cos(3\omega t + \phi) + \cos(\omega t + \phi)] \end{aligned} \quad (3.21)$$

giving tripled frequency 3ω . If a thin film needs to be evaluated, first a 3ω measurement on the substrate without the thin film is needed. The observed in-phase

component of the temperature amplitude of the substrate is [102]

$$\Delta T_{\text{subst}} = \frac{P_{\text{heater}}}{\pi l \kappa_{\text{subst}}} \left[\frac{1}{2} \ln \left(\frac{\kappa_{\text{subst}}}{C_{\text{subst}} (w/2)^2} \right) + \eta - \frac{1}{2} \ln(2\omega) \right] \quad (3.22)$$

where κ_{subst} , C_{subst} , w , l , and P_{heater} are the thermal conductivity of the substrate, heat capacity of the substrate, width of the heater, length of the heater, and amplitude of the heater power per unit length, respectively. If then the sample (substrate and thin film) is measured with the 3ω -method, the thin film can be treated as an additional thermal resistance under the condition $\kappa_{\text{subst}} \gg \kappa_{\text{tf}}$ increasing the amplitude of the temperature oscillation by [102]

$$\Delta T_{\text{tf}} = \frac{P_{\text{heater}}}{\kappa_{\text{tf}}} \frac{d}{w} \quad (3.23)$$

with the thermal conductivity κ_{tf} and thickness d of the thin film (compare fig. 3.8 b)).

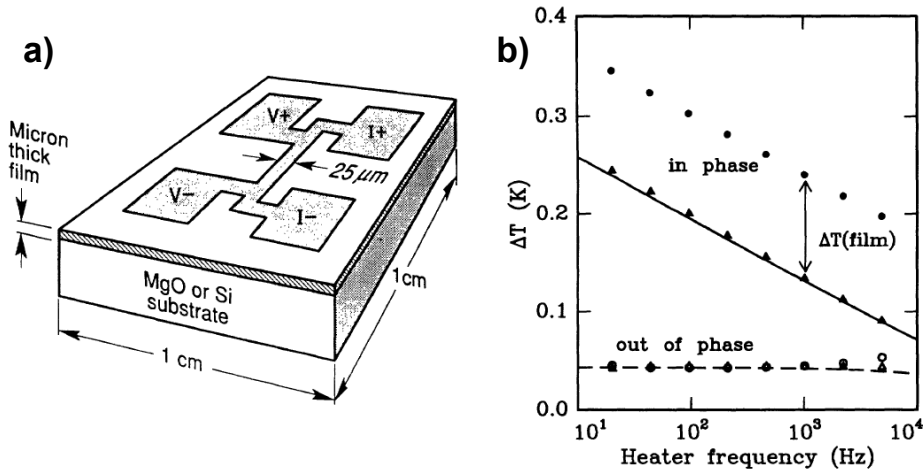


Figure 3.8: a) Geometry for thin film thermal conductivity measurements using the 3ω -method [103]. b) Amplitude of the temperature oscillation of a 3ω measurement of a MgO substrate (triangles) and for a $0.5 \mu\text{m}$ thick a-Si:H film on a MgO substrate (circles) [103].

Experimental details

All 3ω measurements have been performed by Matthias Ikeda in the group of Prof. E. Bauer at the Vienna University (Austria).

4 Results and Discussion

4.1 Characterization of SiGe/Al multilayer systems on thermally oxidized Si substrates

In this chapter, the process of MIC will be verified for thin film SiGe/Al multilayer systems. The structure of the samples is $[\text{Al}(d_{\text{Al}})/\text{Si}_{80}\text{Ge}_{20}(10\text{ nm})]_{50}/\text{SiO}_2(200\text{ nm})/\text{Si}(001)$ with d_{Al} being the nominal layer thickness of the individual Al layers. A multilayer approach was chosen to start the process of MIC at each layer individually and to reduce the time needed for diffusion as well as to impinge the crystal growth of each SiGe layer to control the grain size. The influence of the MIC process on the structural and transport properties will be discussed comparing as-deposited films with the post-annealed ones. Annealing time was kept constant at 1 h, while annealing temperatures T_{a} in the range of 573 K to 873 K were applied. Additionally, the importance of the Al layer thickness d_{Al} for the MIC process will be discussed. The results of this chapter have been partially published in [104].

4.1.1 Verification of MIC in SiGe/Al multilayer systems

For the as-deposited films, TEM BF images of sample $[\text{Al}(1\text{ nm})/\text{Si}_{80}\text{Ge}_{20}(10\text{ nm})]_{50}/\text{SiO}_2(200\text{ nm})/\text{Si}(001)$ taken in cross section are shown in fig. 4.1. At low magnification, no SiGe/Al multilayer structure is apparent in fig. 4.1a). The interface between the SiGe/Al multilayer and the substrate is sharp and of high quality, while the top layer of the SiGe/Al multilayer is not perfectly flat revealing thickness variations in the range of 2 nm. For higher magnifications, the multilayer structure could be observed at the interface between the SiGe/Al multilayer and the substrate. This is shown in fig. 4.1b). The Al appears brighter due to its lower mass in comparison to the averaged mass of $\text{Si}_{80}\text{Ge}_{20}$. The multilayer structure could be observed for up to 6 repetitions of SiGe/Al bilayers starting at the substrate-multilayer interface. Due to defects during growth and potential intermixing of the multilayer system, the interfaces between the individual SiGe and Al layers become more and more blurred and, matching the surface roughness of the top SiGe layer, cannot be distinguished anymore further away from the substrate. The inset in fig. 4.1a) shows a diffraction pattern taken at the area of the SiGe/Al multilayer. Blurred diffraction rings matching the theoretical values for $\text{Si}_{80}\text{Ge}_{20}$ are observed indicating the amorphous state of the SiGe.

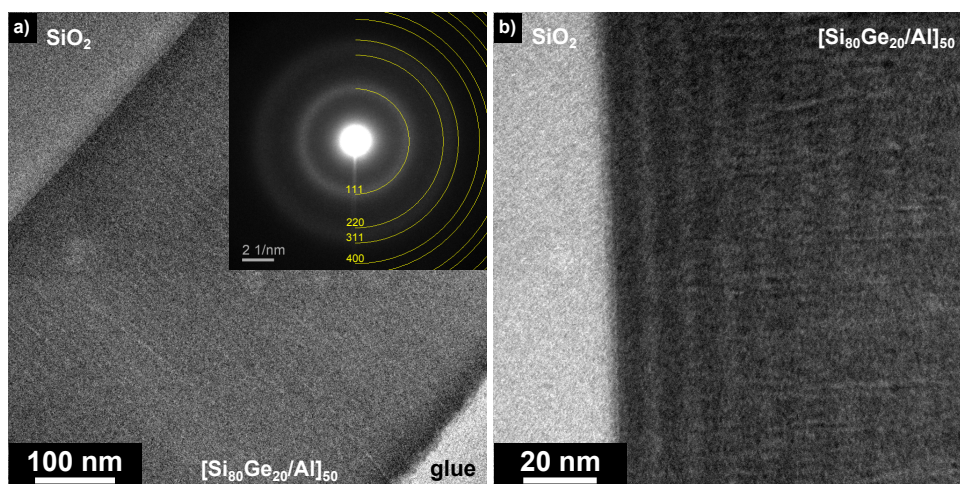


Figure 4.1: TEM BF images of sample $[\text{Al}(1 \text{ nm})/\text{Si}_{80}\text{Ge}_{20}(10 \text{ nm})]_{50}/\text{SiO}_2(200 \text{ nm})/\text{Si}(001)$ in the as-deposited state taken at a) low magnification and b) high magnification [104]. The inset in a) shows a diffraction pattern taken at the area of the multilayer with yellow lines representing the theoretical diffraction rings of $\text{Si}_{80}\text{Ge}_{20}$.

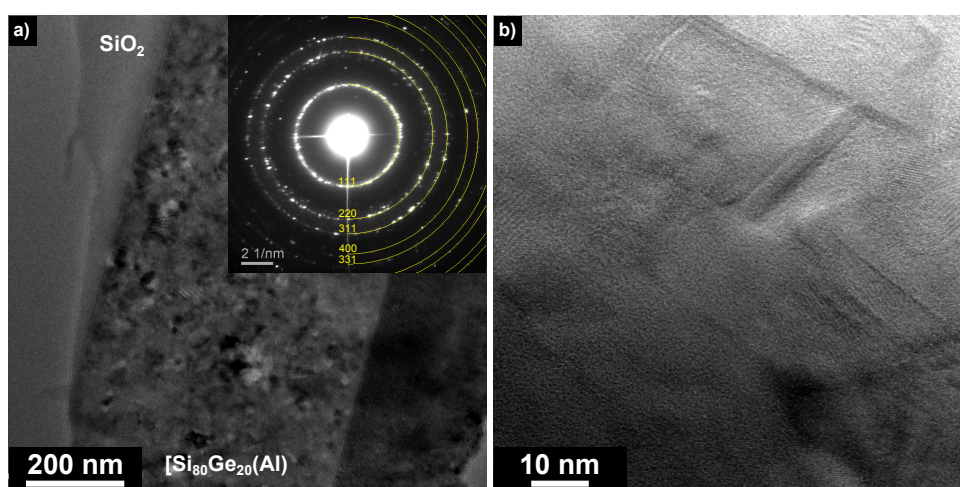


Figure 4.2: TEM BF images of sample $[\text{Al}(1 \text{ nm})/\text{Si}_{80}\text{Ge}_{20}(10 \text{ nm})]_{50}/\text{SiO}_2(200 \text{ nm})/\text{Si}(001)$ after annealing at 873 K taken at a) low magnification and b) high magnification [104]. The inset in a) shows a diffraction pattern taken at the area of the initial multilayer with yellow lines representing the theoretical diffraction rings of $\text{Si}_{80}\text{Ge}_{20}$.

TEM BF images of sample [Al(1 nm)/Si₈₀Ge₂₀(10 nm)]₅₀/SiO₂(200 nm)/Si(001) taken after annealing at 873 K reveal no signs of a multilayer structure in fig. 4.2. At lower magnification, the area of the initial SiGe/Al multilayer in fig. 4.2a) now shows additional diffraction contrast and even isolated Moiré patterns can be observed indicating the presence of crystalline material. Such features are also observed at higher magnification in fig. 4.2b) in the form of Moiré patterns, lattice planes, and stacking faults. The inset in fig. 4.2a) shows a diffraction pattern taken at the area of the initial SiGe/Al multilayer. The previously blurred rings now appear as reflexes forming rings clearly indicating the presence of a polycrystalline phase. The theoretical diffraction rings for Si₈₀Ge₂₀ are matching and thus proof a transition from amorphous SiGe in the as-deposited state to crystalline SiGe after annealing at 873 K. The structural properties of sample [Al(1 nm)/Si₈₀Ge₂₀(10 nm)]₅₀/SiO₂(200 nm)/Si(001) were also characterized by SNMS. The as-deposited multilayer sample is shown in fig. 4.3a), where the signal of Al, Si, and Ge were recorded at a sputtering rate of roughly 0.4-0.5 nm/s. For the Al signal, 7 layer repetitions are visible, while for the Si signal 3 repetitions are hardly distinguishable. As only comparatively little amounts of Ge are present, the Ge signal appears to be of constant value despite the multilayer structure of the sample. The difference in quality of the Al and Si signal can be explained by the actual thickness of the individual layers. The Al layers are 10 nm away from each other, while the Si layers are only separated by 1 nm which reaches the resolution limit of this technique. Nevertheless, SNMS and TEM investigations have shown, that both near the surface and the substrate a SiGe/Al multilayer structure is present and also matches the expected layer thickness values.

The SNMS results for the sample annealed at 573 K are shown in fig. 4.3b). Difference in signal intensities compared to the as-deposited sample is due to difference in size of the sample pieces analyzed. The multilayer structure of the sample seems to be fading, as only 3 layer repetitions in the Al signal and 1 repetition for the Si signal are distinguishable. It appears that already at this temperature diffusion has led to partial intermixing of the multilayer structure. After annealing at 673 K and 873 K, the multilayer structure has completely vanished in the observed SNMS depth profile in fig. 4.3c) and d), respectively. Only an accumulation of Al at the surface can be observed, while the signals of Si and Ge appear at constant values after a slow increase at the beginning caused by matrix effects. This vanishing of the multilayer structure is consistent with the structural changes observed by TEM imaging and was already reported by Konno et al. [105], who observed the dissolution of Al/a-Si multilayers using in-situ TEM during annealing at 493 K.

The accumulation of Al at the surface was also confirmed by X-ray Photoelectron Spectroscopy (XPS). The detected XPS spectrum near the binding energy of the Al-2p peak is shown in fig. 4.4 for the same sample after being annealed at different temperatures T_a . In the as-deposited state and for $T_a = 573$ K, no Al-2p signal is observed. For $T_a \geq 673$ K, the Al-2p peak develops, but is shifted to higher energies

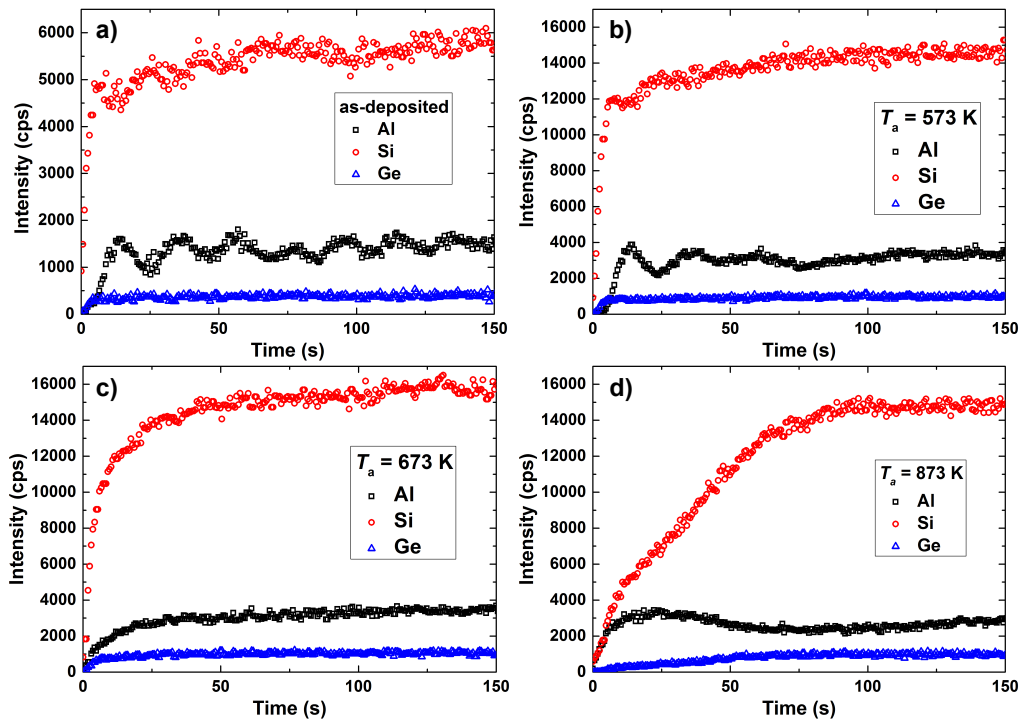


Figure 4.3: SNMS depth profile of sample $[\text{Al}(1 \text{ nm})/\text{Si}_{80}\text{Ge}_{20}(10 \text{ nm})]_{50}/\text{SiO}_2(200 \text{ nm})/\text{Si}(001)$ a) in the as-deposited state and after annealing at b) 573 K, c) 673 K, and d) 873 K [104].

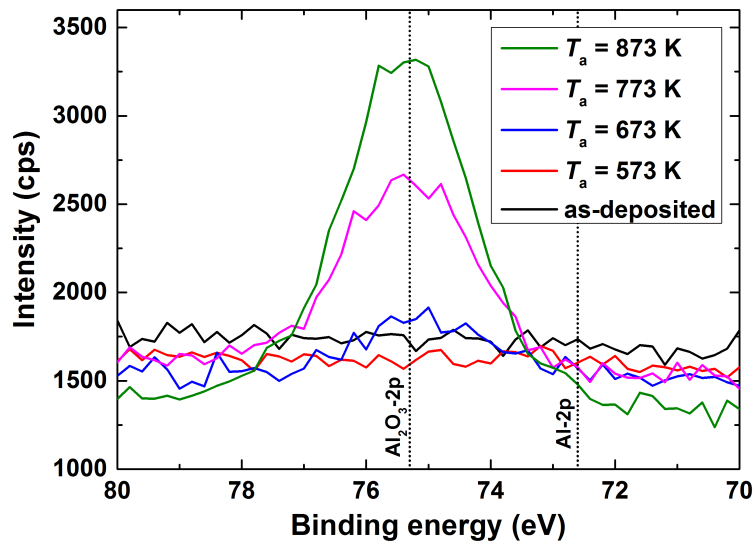


Figure 4.4: XPS spectrum near the binding energy of the Al-2p peak of sample [Al(1 nm)/Si₈₀Ge₂₀(10 nm)]₅₀/SiO₂(200 nm)/Si(001) a) in the as-deposited state and after annealing at b) 573 K, c) 673 K, and d) 873 K [104]. Reported binding energies for Al-2p and Al₂O₃-2p are indicated by dashed lines [106].

as compared to the typical Al-2p binding energy. This shift can be attributed to the oxidation of Al to Al_2O_3 [106].

The multilayer stack could be fully resolved by SIMS in the as-deposited state as shown in fig. 4.5. While the signals of Al and Ge were generally too low to allow for any layer distinction, the Si signal revealed 50 oscillations corresponding to the 50 SiGe layers of sample $[\text{Al}(1 \text{ nm})/\text{Si}_{80}\text{Ge}_{20}(10 \text{ nm})]_{50}/\text{SiO}_2(200 \text{ nm})/\text{Si}$. The decrease in intensity for the Si signal was most likely caused by matrix effects and not related to an actual decrease in Si content of the sample.

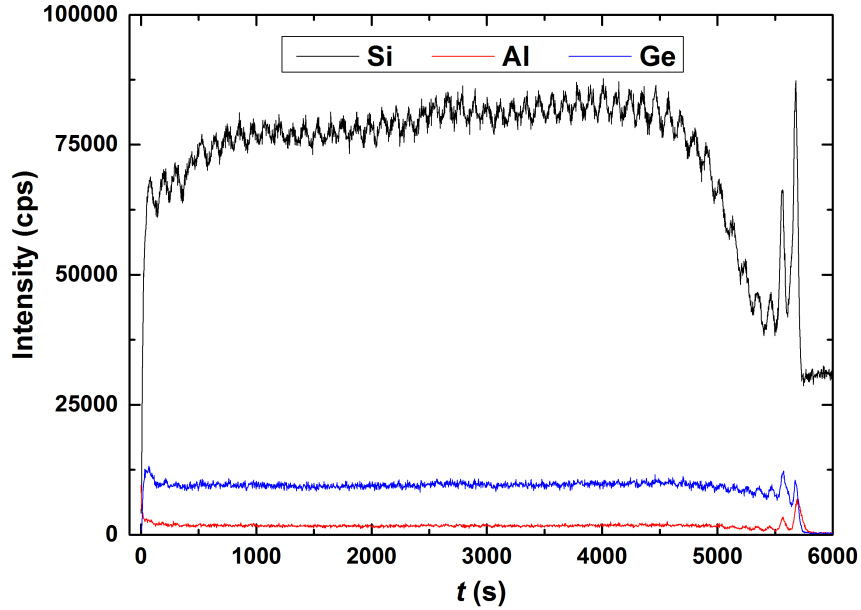


Figure 4.5: SIMS depth profile for elements Si, Al, and Ge of sample $[\text{Al}(1 \text{ nm})/\text{Si}_{80}\text{Ge}_{20}(10 \text{ nm})]_{50}/\text{SiO}_2(200 \text{ nm})/\text{Si}$ in the as-deposited state.

The samples were also analyzed by XRD to directly verify the success of the MIC process regarding crystallization of the SiGe. The diffraction patterns of sample $[\text{Al}(1 \text{ nm})/\text{Si}_{80}\text{Ge}_{20}(10 \text{ nm})]_{50}/\text{SiO}_2(200 \text{ nm})/\text{Si}(001)$ are compared in fig. 4.6 with respect to different annealing temperatures T_a . A peak close to 62° is observed for all measurements which can be attributed to the Cu-K_β excitation of the Si(004) substrate peak. No further peaks can be observed in the as-deposited state and for the sample annealed at 573 K. This agrees with the TEM and SNMS results that no MIC has taken place for these samples up to an annealing temperature of 573 K. For $T_a \geq 673 \text{ K}$, 3 peaks corresponding to crystalline $\text{Si}_{80}\text{Ge}_{20}$ are observed despite T_a being lower than the reported range of crystallization temperature for SiGe of $823 \text{ K} \leq T_{\text{cryst, SiGe}} \leq 1073 \text{ K}$ (depending on SiGe composition, deposition method,

and annealing time) [107][108][70]. The peaks develop with increasing annealing temperature. Additionally, no signs of double peaks are revealed despite the annealing temperatures exceeding the eutectic temperature of the Al-Si and Al-Ge systems of $T_{\text{eut,AlSi}} = 850$ K and $T_{\text{eut,AlGe}} = 693$ K, respectively [65]. Therefore, no decomposition into different $\text{Si}_{1-x}\text{Ge}_x$ phases is observed.

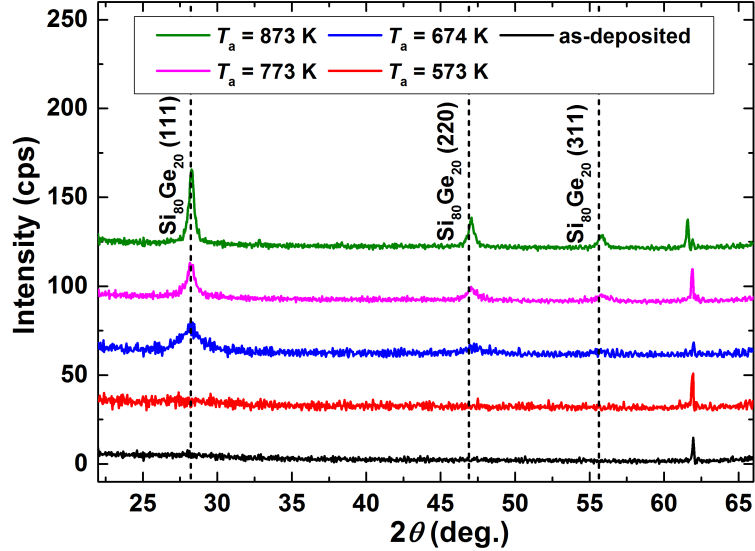


Figure 4.6: Comparison of the XRD ($\theta - 2\theta$) patterns for sample $[\text{Al}(1 \text{ nm})/\text{Si}_{80}\text{Ge}_{20}(10 \text{ nm})]_{50}/\text{SiO}_2(200 \text{ nm})/\text{Si}(001)$ annealed at different temperatures T_a [104]. The theoretical diffraction peak positions for crystalline $\text{Si}_{80}\text{Ge}_{20}$ for the utilized $\text{Cu-K}\alpha$ wavelength are indicated by dashed lines.

The diffraction patterns shown in fig. 4.7 highlight the influence of the Al thickness d_{Al} on the MIC process. Again, the $\text{Cu-K}\beta$ excitation of the $\text{Si}(004)$ substrate peak is observed in all diffraction patterns. The sample with Al thickness of $d_{\text{Al}} = 0.18$ nm exhibits no peaks corresponding to the $\text{Si}_{80}\text{Ge}_{20}$ phase and thus can be assumed to be (x-ray) amorphous. The 3 observed $\text{Si}_{80}\text{Ge}_{20}$ peaks develop for increasing d_{Al} showing the beneficial influence of Al on the crystallization process for the SiGe via MIC. The $\text{Si}_{80}\text{Ge}_{20}$ grain size L_{gr} was estimated by the Scherrer formula (eq. 3.7) for samples with detectable $\text{Si}_{80}\text{Ge}_{20}$ peaks and the results are summarized in table 4.1. The grain size increases both for increasing d_{Al} and increasing T_a . This, together with a reduction of the crystallization temperature for the $\text{Si}_{80}\text{Ge}_{20}$ down to 673 K, verifies the MIC process.

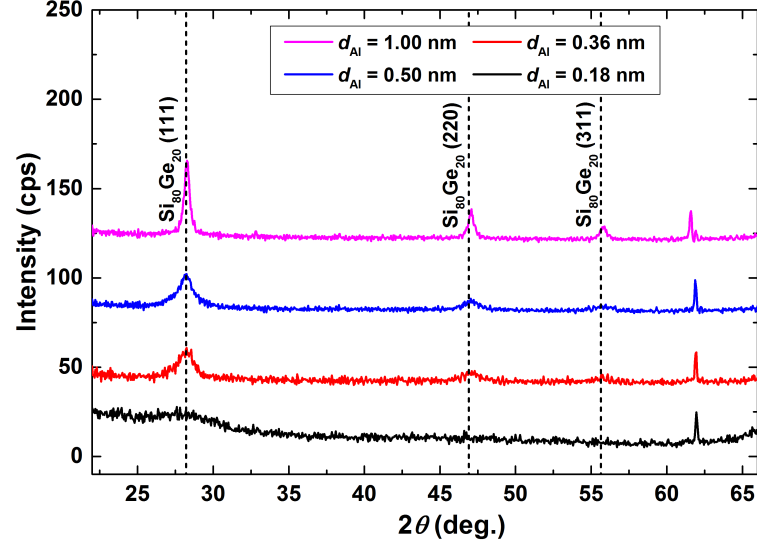


Figure 4.7: Comparison of the XRD ($\theta - 2\theta$) patterns for samples $[\text{Al}(d_{\text{Al}})/\text{Si}_{80}\text{Ge}_{20}(10\text{ nm})]_{50}/\text{SiO}_2(200\text{ nm})/\text{Si}(001)$ with different Al thicknesses d_{Al} after annealing at 873 K for 1h [104]. The theoretical diffraction peak positions for crystalline $\text{Si}_{80}\text{Ge}_{20}$ for the utilized Cu- K_α wavelength are indicated by dashed lines.

Table 4.1: Results of Scherrer analysis for estimation of the $\text{Si}_{80}\text{Ge}_{20}$ grain size L_{gr} for samples $[\text{Al}(d_{\text{Al}})/\text{Si}_{80}\text{Ge}_{20}(10\text{ nm})]_{50}/\text{SiO}_2(200\text{ nm})/\text{Si}(001)$ as function of Al thickness d_{Al} and applied annealing temperature T_{a} .

d_{Al} (nm)	$\text{Si}_{80}\text{Ge}_{20}$ grain size L_{gr} (nm)				
	as-dep.	573 K	673 K	773 K	873 K
0.18	-	-	-	-	-
0.36	-	-	-	-	5
0.50	-	-	-	5	11
1.00	-	-	7	7	18

4.1.2 Transport properties

The values of the electrical resistivity ρ measured at room temperature for the previously discussed samples is summarized in table 4.2. Samples that had no detectable $\text{Si}_{80}\text{Ge}_{20}$ peaks showed insulating behavior and thus could not be measured with our setup. The lower limit of resistivity for these samples can only be estimated as $10^6 \text{ m}\Omega\text{cm}$. Samples that revealed crystalline $\text{Si}_{80}\text{Ge}_{20}$ have room temperature resistivity in the range of $5 \cdot 10^1 \text{ m}\Omega\text{cm}$ to $2 \cdot 10^2 \text{ m}\Omega\text{cm}$. The resistivity decreases with increasing annealing temperature T_a as well as increasing Al thickness d_{Al} . This correlates to increased crystallinity and the $\text{Si}_{80}\text{Ge}_{20}$ grain size presented in table 4.1. Together, this can be interpreted as a negative influence on the resistivity by the increased scattering of charge carriers at more frequent grain boundaries or crystal defects.

Table 4.2: Comparison of room temperature resistivity ρ of samples $[\text{Al}(d_{\text{Al}})/\text{Si}_{80}\text{Ge}_{20}(10 \text{ nm})]_{50}/\text{SiO}_2(200 \text{ nm})/\text{Si}(001)$ with different Al thickness d_{Al} and applied annealing temperature T_a .

d_{Al} (nm)	resistivity ρ (m Ωcm)				
	as-dep.	573 K	673 K	773 K	873 K
0.18	$> 10^6$	$> 10^6$	$> 10^6$	$> 10^6$	$> 10^6$
0.36	$> 10^6$	$> 10^6$	$> 10^6$	$> 10^6$	$2.0 \cdot 10^2$
0.50	$> 10^6$	$> 10^6$	$> 10^6$	$1.2 \cdot 10^2$	$1.1 \cdot 10^2$
1.00	$> 10^6$	$> 10^6$	$1.7 \cdot 10^2$	$5.4 \cdot 10^1$	$5.7 \cdot 10^1$

Measurements to find optimal heating rates in the range from 0.1 K/min to 2 K/min were conducted on sample $[\text{Al}(1 \text{ nm})/\text{Si}_{80}\text{Ge}_{20}(10 \text{ nm})]_{50}/\text{SiO}_2(200 \text{ nm})/\text{Si}(001)$ annealed at 873 K for 1 h, the sample with the lowest resulting resistivity after MIC. The influence of the applied heating rate on the measured resistivity can be seen in fig. 4.8a). Measurements were conducted consecutively without recontacting in order from highest to lowest applied heating rate. The difference between resistivity values during heating and cooling becomes visible and indicates bad thermal coupling between sample and heaters. This difference decreases for lower heating rates and stays nearly constant for heating rates down from 1 K/min. As the thermal coupling between samples and heaters could not be improved for our measurement system at this point, a heating rate of 1 K/min was chosen for all following measurements, because the increased measurement time due to lower heating rates would not warrant the miniscule reduction of the hysteresis between heating and cooling cycles.

Looking at the Arrhenius-plot of the resistivity measurements in fig. 4.8b), two linear regions separated by a kink between 500 K to 600 K become apparent. Furthermore, the resistivity increases with every completed heating cycle indicating still ongoing

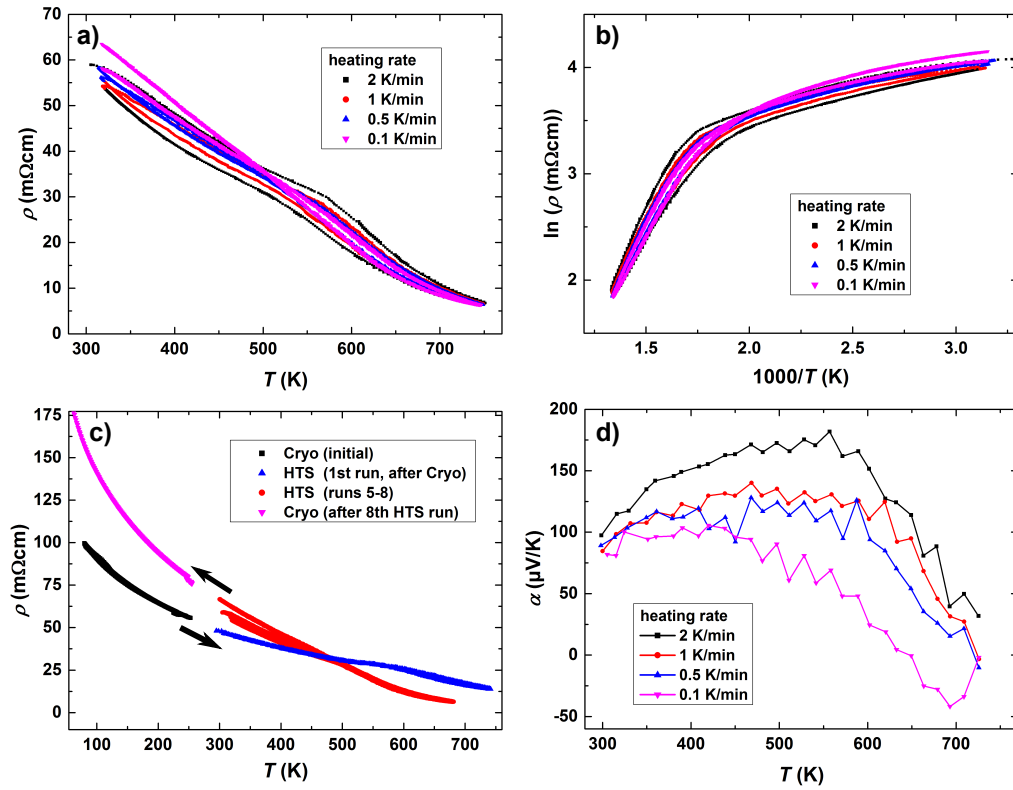


Figure 4.8: a) Measurement of the electrical resistivity ρ at different heating rates for sample $[\text{Al}(1 \text{ nm})/\text{Si}_{80}\text{Ge}_{20}(10 \text{ nm})]_{50}/\text{SiO}_2(200 \text{ nm})/\text{Si}(001)$ annealed at 873 K for 1 h. b) Arrhenius-plot of the data presented in a). c) Comparison of the resistivity measurements at low and high temperatures. d) Measured Seebeck coefficient α corresponding to the measurement cycles presented in a).

structural changes in the sample at elevated temperatures. This resistivity increase is also shown in fig.4.8c). Here the measurement was performed at low temperatures in a cryostat and compared to high temperature results obtained in the HTS system. The sample was first measured in the cryostat revealing exponentially decreasing resistivity with increasing temperature. The then following high temperature measurement in the HTS system shows matching resistivity values and an ongoing decrease in resistivity. Seven additional measurement cycles were performed on the sample with cycles 5 to 8 being the previously discussed cycles highlighted in fig. 4.8a) and b). Cycles 2 to 4 are not shown, because results were of too noisy quality due to bad sample contacts. After the eight high temperature measurement cycles in the HTS system, the sample was reintroduced to the cryostat. There the sample showed qualitatively the same exponential resistivity behavior as before but at increased values seamlessly connecting to the high temperature region, which proofs structural changes in the sample and rules out a systematic error in the HTS system. Additional Hall measurements on the sample in the cryostat revealed positive, constant charge carrier concentration in the range of $6 \cdot 10^{19} \text{ cm}^{-3}$ to $9 \cdot 10^{19} \text{ cm}^{-3}$ over the whole low temperature range. A charge carrier concentration of that order should result in a Seebeck coefficient of roughly $150 \mu\text{V/K}$ for SiGe at room temperature linearly increasing with temperature up to at least 1100 K [57].

The Seebeck coefficient, which was measured simultaneously during measurement cycles 5 to 8, is shown in fig. 4.8d). The Seebeck coefficient shows the same qualitative temperature dependence for all heating rates, but decreases in value for every heat-

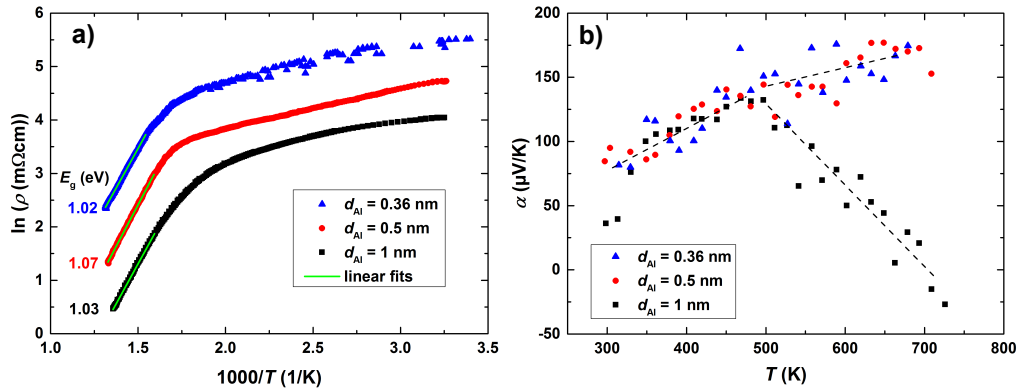


Figure 4.9: Measured a) resistivity ρ as Arrhenius-plot and b) Seebeck coefficient for samples with different Al thickness d_{Al} annealed at 873 K for 1 h [104]. Linear fits to the high temperature region in the Arrhenius-plot were added as green lines with the corresponding estimation of the band gap energy E_g . Dashed lines in b) are guides to the eye.

ing cycle completed. Room temperature values for the Seebeck coefficient are in the range of $80 \mu\text{V}/\text{K}$ to $100 \mu\text{V}/\text{K}$. The Seebeck coefficient first increases with temperature, but then starts to decrease drastically and partially even negative values are reached. As the Seebeck coefficient is lower than expected and even deviates from the expected linear increase with temperature, the most likely assumption would be a compensation of the positive charge carriers by negative charge carriers. The resistivity and Seebeck coefficient of the three samples after MIC transformation annealed at 873 K for 1 h are compared in fig. 4.9a) and b), respectively. The resistivity shows the same qualitative temperature dependence for all three samples with a kink in resistivity around 500 K to 600 K . Only a shift to lower resistivity values for higher Al contents distinguishes the samples. Linear fits to the high temperature regions were added. The slope was used to calculate the band gap energy E_g using equations (2.48), (2.51), and (2.56) with E_g lying in the range of 1.02 eV to 1.07 eV . These values are smaller than the value of $E_{g,\text{Si}} = 1.12 \text{ eV}$ for Si at room temperature. This reduction could either be explained by the SiGe carrying the intrinsic current and having a smaller band gap than pure Si [109] or by pure Si having its band gap reduced at elevated temperatures [110]. Nevertheless, the assumption of intrinsic carrier excitation is also supported by the Seebeck measurements. All three samples exhibit linearly increasing Seebeck coefficients up to temperatures of about 500 K . After that a decrease in slope is observed with the sample of the highest Al content even showing a negative slope thus again indicating charge carrier compensation.

Another piece of sample $[\text{Al}(1 \text{ nm})/\text{Si}_{80}\text{Ge}_{20}(10 \text{ nm})]_{50}/\text{SiO}_2(200 \text{ nm})/\text{Si}(001)$ annealed at 873 K for 1 h was sent to Fraunhofer IPM for comparison measurements, which

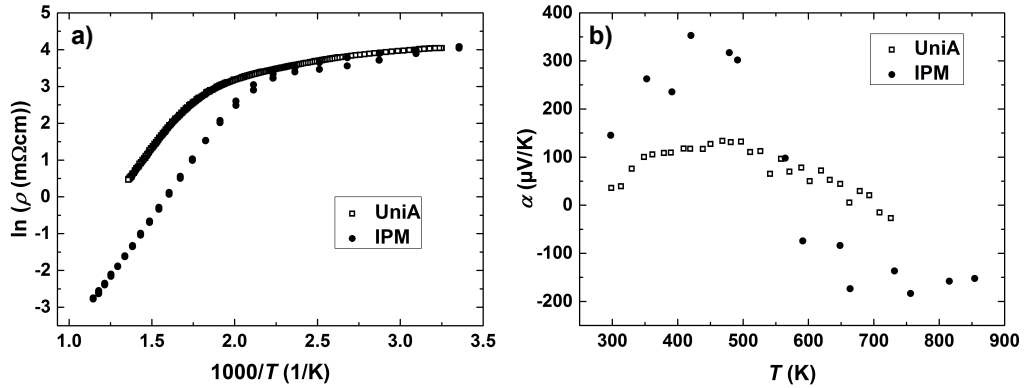


Figure 4.10: Comparison of a) electric resistivity and b) Seebeck coefficient for sample $[\text{Al}(1 \text{ nm})/\text{Si}_{80}\text{Ge}_{20}(10 \text{ nm})]_{50}/\text{SiO}_2(200 \text{ nm})/\text{Si}(001)$ annealed at 873 K for 1 h measured at the University of Augsburg (UniA) and the Fraunhofer IPM (IPM).

are shown in fig. 4.10. The resistivity measurement reveals the same behavior except for the kink appearing at lower temperatures around 450 K. This discrepancy could be explained by the bad thermal coupling in the HTS system mentioned earlier. The Seebeck coefficients measured by the Fraunhofer IPM are generally of greater absolute values compared to the values measured by the HTS system, most likely again indicating bad thermal coupling of the sample. Nevertheless, a similar change in temperature dependent behavior of the Seebeck coefficient was also observed in the measurement conducted at the Fraunhofer IPM as the Seebeck coefficient started to show compensation around 450 K and even changed its sign to negative for higher temperatures.

At Fraunhofer IPM, also Hall measurements at high temperatures were carried out. The results are shown in fig. 4.11. A constant charge carrier density of $n = +3 \cdot 10^{19} \text{ cm}^{-3}$ up to temperatures of 425 K is revealed. At 450 K, the charge carrier density changes abruptly to $n = -1 \cdot 10^{19} \text{ cm}^{-3}$ with the negative sign now signifying electrons as charge carriers instead of holes. The charge carrier density then increases exponentially in absolute value with increasing temperatures. This behavior is expected for intrinsic semiconductors. Still the question arises why intrinsic charge carrier excitation takes place at such low temperatures as the expected intrinsic charge carrier concentration of Si would be only of the order of $n_i = 10^{14} \text{ cm}^{-3}$ in the temperature range of 450 K to 500 K [110]. The intrinsic charge carrier density of Si(Ge) should be negligible compared to a charge carrier density of $n = +3 \cdot 10^{19} \text{ cm}^{-3}$ up to temperatures of at least 1100 K [110].

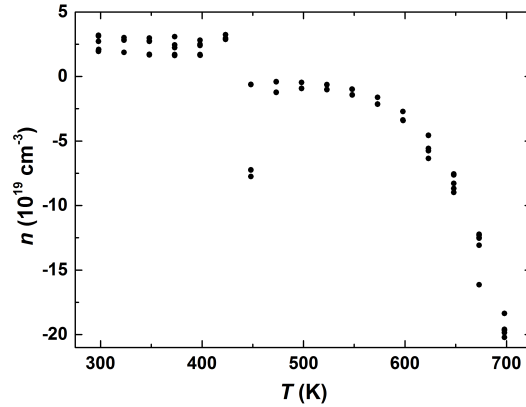


Figure 4.11: Charge carrier density of sample $[\text{Al}(1 \text{ nm})/\text{Si}_{80}\text{Ge}_{20}(10 \text{ nm})]_{50}/\text{SiO}_2(200 \text{ nm})/\text{Si}(001)$ annealed at 873 K for 1 h measured at Fraunhofer IPM [104].

This contradiction can only be solved by having the Si substrate in electrical contact to the measured thin film system. According to equation (2.72), it is possible for Al

to chemically reduce SiO_2 to Si. Since the nominal thickness of the SiO_2 isolation layer was 200 nm and the added up thickness of all Al layers in the multilayer system of the sample with the highest Al content amounted only to 100 nm, it was assumed that a short circuit to the substrate would not be possible. In-situ TEM observations of interconnections forming in a Al/ SiO_2 /Si interface through the SiO_2 layer during MIC have been shown by Kim and Lee [111] and highlighted that a SiO_2 layer can be partially penetrated thus reducing the amount of Al needed to build electrical contacts. Additional evidence for an electrical short circuit of the thin film system to the Si substrate is given by the charge carrier density at elevated temperatures. The measured charge carrier densities for temperatures higher than 450 K were in absolute value greater than $|n| > 10^{19} \text{ cm}^{-3}$, which is 5 orders of magnitude too large compared to the expected value of $n_i = 10^{14} \text{ cm}^{-3}$. The thickness d of a sample analyzed by Hall measurements is indirect proportional to the calculated charge carrier density n via equation (3.16). The thickness for the calculation was assumed to be the combined thickness of all SiGe layers $d_{\text{SiGe, total}} = 1000 \text{ nm}$ over the whole temperature range. If now electrical contact to the substrate is assumed, the values determined for charge carrier density (and also resistivity) would need to be corrected to accustom for the different layer thickness, which then would be at least 3 orders of magnitude greater as the substrate was roughly of 1 mm thickness. One also has to account for the possibility of the initial thickness to be overestimated due to the SiGe not being fully crystallized as the required amount of Al compared to Si for a complete MIC was determined to be $d_{\text{Al}}/d_{\text{Si}} = 1$ [71] instead of the ratios of $d_{\text{Al}}/d_{\text{Si}} \leq 0.1$ for the samples presented here. This totals in an overestimation of the charge carrier concentration of at least 4 orders of magnitude such that the real charge carrier concentration would be in the range of $10^{14} \text{ cm}^{-3} < |n| < 10^{15} \text{ cm}^{-3}$ which corresponds to the expected intrinsic charge carrier density for this temperature range.

For temperatures below 450 K, the electric transport properties are mainly governed by the SiGe thin film. For temperatures higher than 450 K, the resistivity of the Si substrate is already lowered sufficiently that the actual resistance of the substrate is smaller than the resistance of the SiGe film and hence in the case of a parallel circuit the current is mainly carried by the channel with the smaller resistance, here being the substrate. Since the mobility of electrons in Si is higher than of holes, the resulting Seebeck sign for intrinsic Si is negative. As the SiGe is always in direct electrical contact to the Si substrate after formation of conducting short circuits through the SiO_2 layer during annealing, this combination of Si substrate, SiO_2 isolation layer, and MIC capable Al/SiGe multilayer thin film system is not suitable for thermoelectric application at high temperatures. Also the measured transport properties below temperatures of 450 K are of questionable trustworthiness as interactions between the Si substrate and SiGe thin film cannot be ruled out even when the current is mainly carried by the SiGe. To exclude any further influence of the substrate on the thermoelectric active SiGe thin film, the substrate was changed from this point on to

aluminum oxide based ceramics, which cannot be reduced by Al and are insulating even at elevated temperatures.

4.2 Characterization of SiGe/Al multilayer systems on aluminum oxide based substrates

In the following chapter, all samples analyzed were deposited onto aluminum oxide based substrates. This change was caused by the reduction of the SiO₂ isolation layer of the Si substrate via Al as discussed in the previous chapter. Three commercially available substrates were utilized being low temperature co-fired ceramics (LTCC), ADS-996 (ADS), and sapphire (Sap). All three substrates have in common that they are electrically insulating. LTCC is normally used for printable multilayer packaging in electronic microsystems [112]. The whole microsystem consisting of the ceramic support structure and any circuits are co-fired (sintered) in one step. For LTCC the sintering temperature generally is below 1200 K. In this work, already sintered sheets of LTCC were utilized as substrates. ADS is a ceramic provided by the company CoorsTek [113] and was specifically intended for thin film application. The used sapphire substrates were single-sided polished and of (0001) orientation. Results will be presented primarily on the LTCC based samples, while only discussing the other substrates when significantly different results were obtained. The thin film systems analyzed in this chapter are again sputter deposited multilayer samples $[\text{Al}(d_{\text{Al}})/\text{Si}_{80}\text{Ge}_{20}(d_{\text{SiGe}})]_N$ in the as-deposited case. Results of this chapter have been partially published in [114][115].

4.2.1 Microstructure and morphology

The morphology of the as-deposited sample $[\text{Al}(1\text{ nm})/\text{Si}_{80}\text{Ge}_{20}(10\text{ nm})]_{100}/\text{LTCC}$ was imaged by SEM. At lower magnification, a coarse grained surface consisting of trenches and hillocks is observed in fig. 4.12a). LTCC as a sintered ceramic is expected to have a rather rough surface and seemingly even the deposition of more than 1 μm film is not enough to fully compensate the pristine surface roughness. This becomes even more pronounced for higher magnification as can be seen in fig. 4.12b). The trenches between the big grains can have sharp edges and are even so deep that no signal from their bottom can be detected. The bigger grains are at least 1 μm in lateral size and consist of fine grains of size 1 nm to 10 nm themselves. Except for the obvious bigger trenches, the bigger grains appear to be in physical contact to each other.

After annealing at 873 K for 1 h, the surface morphology is preserved as shown in fig. 4.12c). It appears, as if the sample was partially melted during the annealing process as the number of deep trenches decreased. While hillocks in the form of

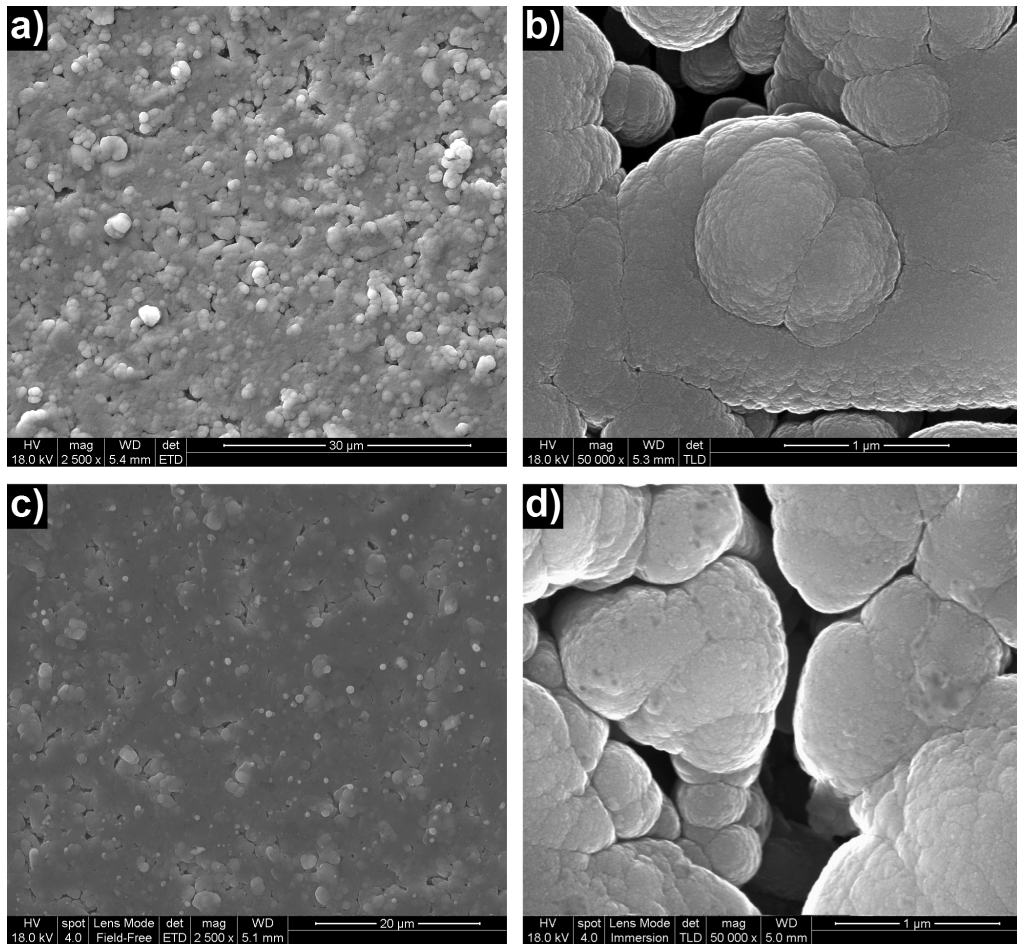


Figure 4.12: SEM images of sample $[\text{Al}(1 \text{ nm})/\text{Si}_{80}\text{Ge}_{20}(10 \text{ nm})]_{100}/\text{LTCC}$ a),b) in the as-deposited state and c),d) after annealing at 873 K for 1 h.

bigger grains can still be found, the surface of the bigger grains itself appears to be smoothed out. This becomes more pronounced at higher magnification in fig. 4.12d), where the fine grained surface structure partially vanished and was replaced by a flat area in the middle right of the image. Despite the partial surface melting, the trenches and their sharp edges remain without being filled.

Since it was not possible to reach the bottom of the trenches with conventional AFM, a specially prepared cross section was used for SEM imaging. Pieces of sample [Al(1 nm)/Si₈₀Ge₂₀(10 nm)]₁₀₀/LTCC, that had been annealed at 873 K for 1 h, were prepared by means of conventional TEM sample preparation: Two stripes were cut out with a diamond saw and glued together with the deposited thin films facing each other. Then this cross section stack was mechanically ground down to a thickness of several microns. As first SEM experiments revealed strong charging effects obscuring the images, an additional thin Pt layer of 50 nm thickness was deposited on top of the cross section to improve conductivity of the sample. The cross section covered by the thin Pt layer is shown in fig. 4.13a). At first glance, three areas can be differentiated with a broad, dark stripe horizontally separating two brighter regions at the bottom and top of the image. Numerous smaller flakes and cracks are apparent. Upon closer view, the brighter regions have another subregion, which appears to be smooth avoid of any flakes except for mechanically damaged areas. As this region is of roughly 1 μm vertical width, this two areas have to be the SiGe thin films with the darker region presenting the glue interface. This is proven by elemental maps for the elements Si, Ge, and Al presented in fig. 4.13b)-e). Selective points of higher intensity in the elemental maps are an artifact caused by the software due to bad statistical evaluation and should not be perceived as spots of element agglomerations. The elemental maps for Si and Ge reveal the same local distribution for both elements. Both, the top and bottom layer, have a discontinuity in form of a trench. It becomes obvious, that these discontinuities are caused by trenches in the LTCC substrate itself as in both cases the area of the glue interface reaches into the LTCC substrate. Since the edges of these trenches are still covered by SiGe, they are no artifact of the grinding preparation. In the bottom layer, a hillock is also observed. This hillock is caused by a big grain of the LTCC substrate reaching out of its surface and thus bending the SiGe layer. Looking at the Al elemental map, this grain mainly consists of Al. Another similar Al based grain can be found in the top LTCC substrate making it unlikely that the grain causing the hillock is due to Al segregation from the Al/SiGe multilayer system. Most probably such Al based grains are harder than the other components of the LTCC substrate and when being polished remain as hillocks or are broken out leaving trenches behind. Samples deposited onto ADS ceramic substrates showed qualitatively the same morphology with trenches and hillocks due to the same coarse grained surface structure of a (polished) sintered ceramic. Samples deposited onto polished sapphire substrates had completely flat surfaces with roughness being lower than 3 nm.

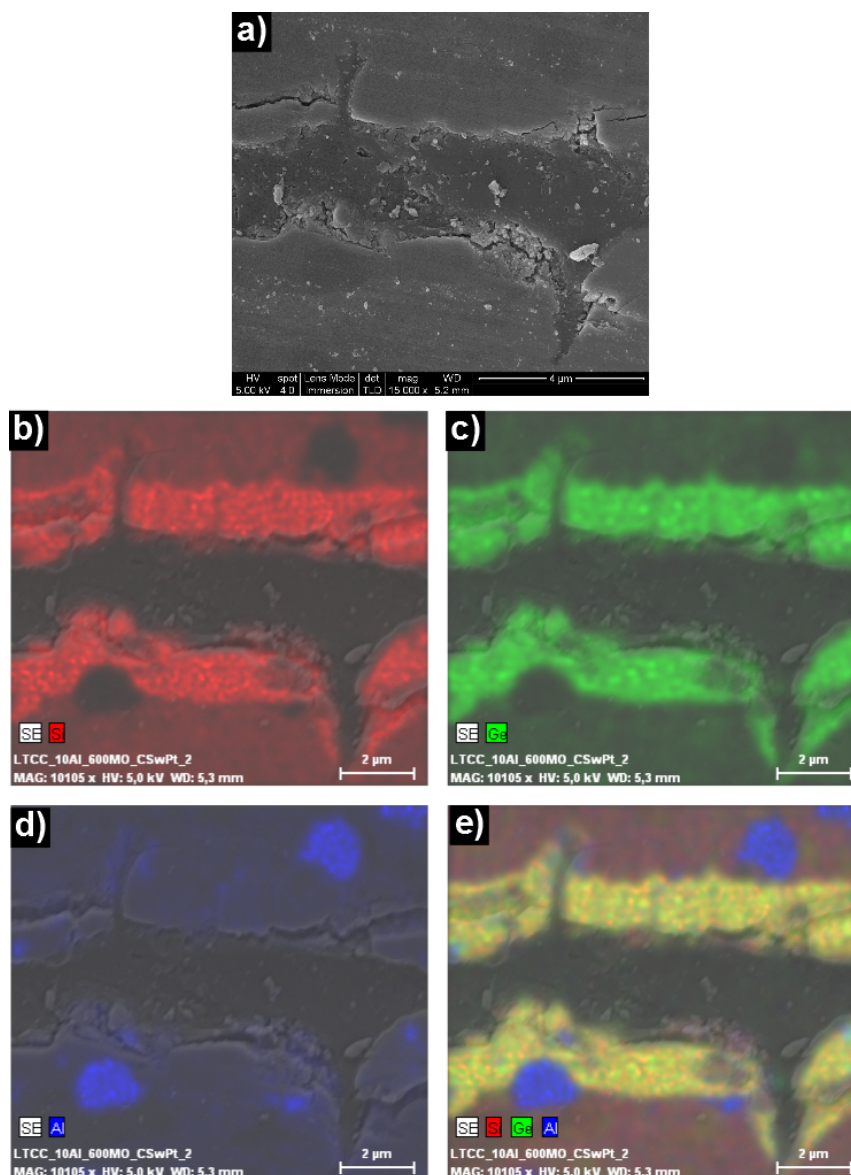


Figure 4.13: a) SEM cross section image of two pieces of sample $[Al(1\text{ nm})/Si_{80}Ge_{20}(10\text{ nm})]_{100}/LTCC$ that were annealed at 873 K for 1 h and glued together for TEM preparation. The prepared cross section was covered with a thin Pt film ($\approx 50\text{ nm}$) to increase its conductivity and thus reduce charging effects. Elemental mappings overlaid with the region shown in a) for the elements b) Si, c) Ge, d) Al, and e) all of the three prior elements together.

Nevertheless, it was shown that trenches in the SiGe thin film indeed reach down to the substrate in the case of LTCC. Therefore, the presence of holes in the SiGe thin film with a partially non-uniform thickness have to be kept in mind for all measurements involving the knowledge of the film thickness like resistivity measurements. Two samples with different thicknesses for the individual SiGe and Al layers were investigated by TEM. The ratio of $d_{\text{Al}}/d_{\text{SiGe}}$ is the same for both samples with the individual layer thicknesses being $d_{\text{SiGe}} = 10 \text{ nm}$, $d_{\text{Al}} = 1 \text{ nm}$ and $d_{\text{SiGe}} = 40 \text{ nm}$, $d_{\text{Al}} = 4 \text{ nm}$. In the as-deposited state two different microstructures are observed. In the case of the thicker sample with an Al layer thickness of 4 nm, continuous layers in multilayer structure are observed in fig. 4.14b). Contrary to this, the thinner sample with an Al layer thickness of 1 nm exhibits an assembly of Al nanodots as shown in fig. 4.14a). Additionally, it is apparent for both samples that the Al layers appear darker than the remaining parts of the sample. With a layer thickness ratio of $d_{\text{Al}}/d_{\text{SiGe}} = 0.1$, the majority of the samples is expected to be SiGe and to appear darker in a TEM bright field image due to higher average atomic mass compared to Al. Nonetheless, the Al parts reveal darker contrast in comparison. This can be resolved by fig. 4.15, where a high resolution image of the nanodots of the thin layered sample is presented. Lattice planes are distinguishable in the nanodots, corresponding to crystalline Al and such added diffraction contrast makes the Al appear darker than the amorphous SiGe [114].

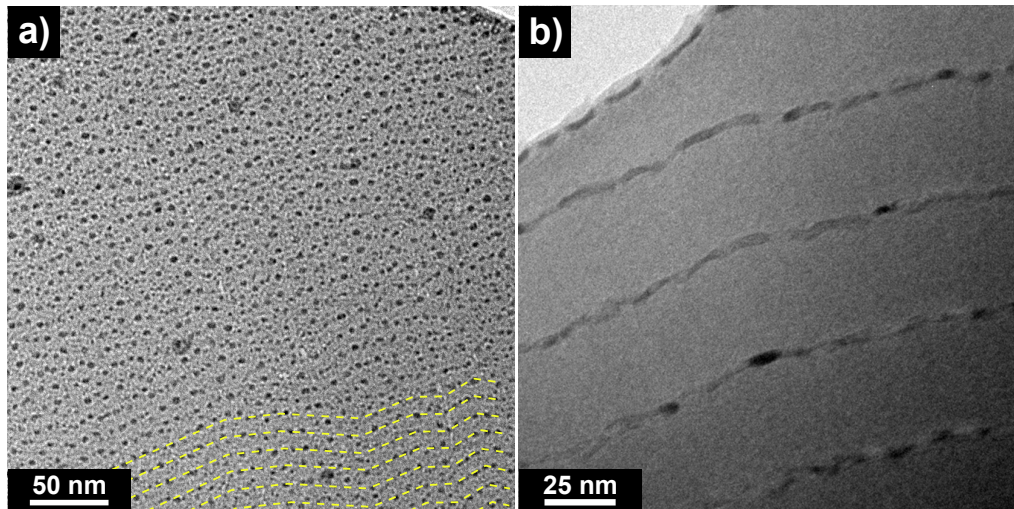


Figure 4.14: TEM BF images of samples a) $[\text{Al}(1 \text{ nm})/\text{Si}_{80}\text{Ge}_{20}(10 \text{ nm})]_{100}/\text{LTCC}$ and b) $[\text{Al}(4 \text{ nm})/\text{Si}_{80}\text{Ge}_{20}(40 \text{ nm})]_{50}/\text{LTCC}$ in the as-deposited state [114] taken in cross section. Dashed lines indicate the multilayered structure.

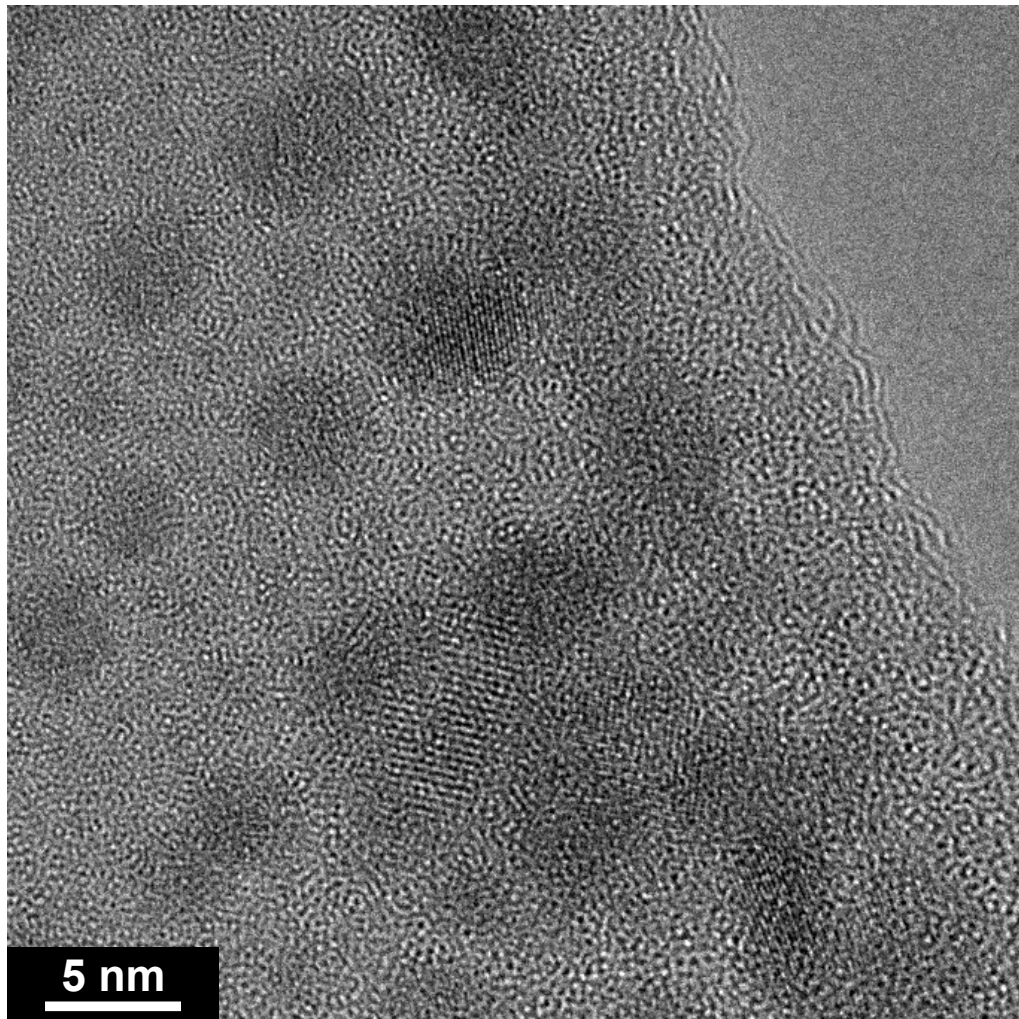


Figure 4.15: TEM BF cross section image of sample $[\text{Al}(1 \text{ nm})/\text{Si}_{80}\text{Ge}_{20}(10 \text{ nm})]_{100}/\text{LTCC}$ in the as-deposited state taken at high resolution [114].

After being annealed at 873 K for 1 h, both samples do not show any signs of their prior microstructures in fig.4.16a),c). Both the nanodot and multilayer structure have vanished and been replaced by diffractive contrast features. Additionally, high resolution images in fig. 4.16b),d) reveal grains and lattice planes of different orientations. This matches the results for samples deposited on thermally oxidized Si substrates of section 4.1.1.

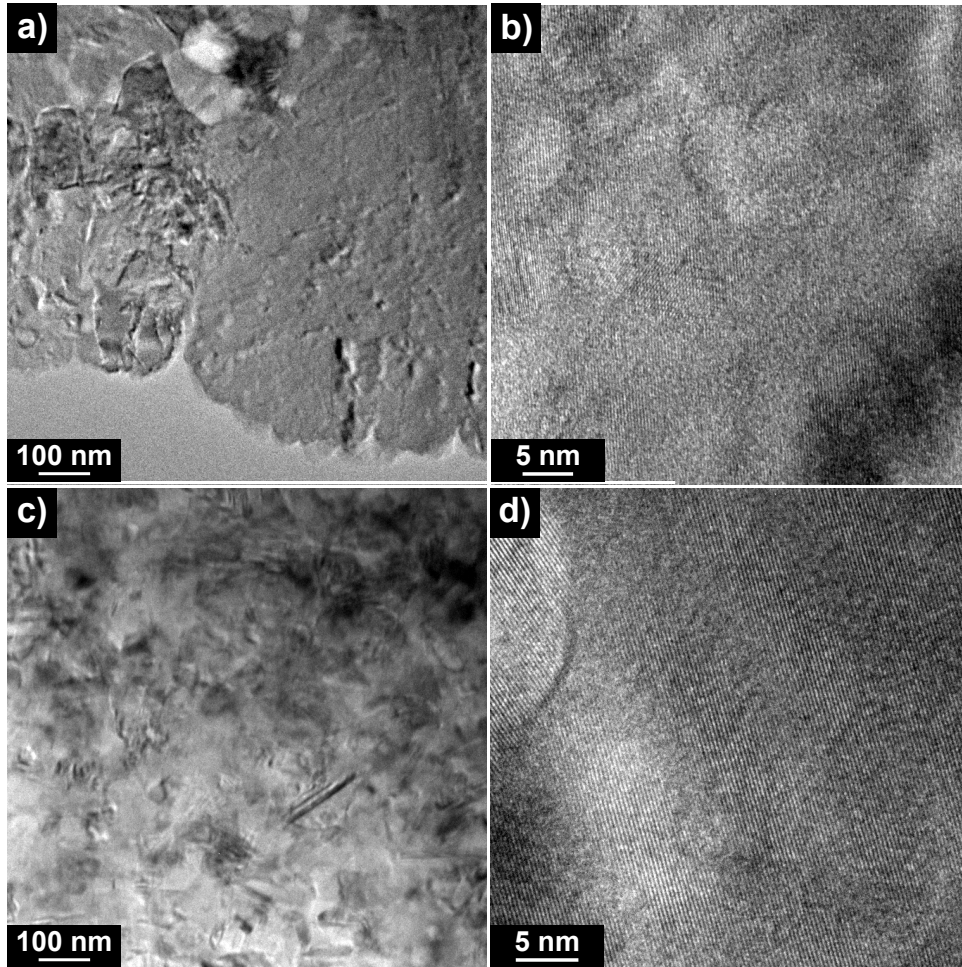


Figure 4.16: TEM BF images of samples a),b) [Al(1 nm)/Si₈₀Ge₂₀(10 nm)]₁₀₀/LTCC and c),d) [Al(4 nm)/Si₈₀Ge₂₀(40 nm)]₅₀/LTCC after annealing at 873 K for 1 h taken in cross section [115].

The series of samples with a constant ratio d_{Al}/d_{SiGe} was also analyzed by $\theta-2\theta$ XRD. Only the XRD patterns for the samples annealed at 873 K for 1 h are shown in fig. 4.17

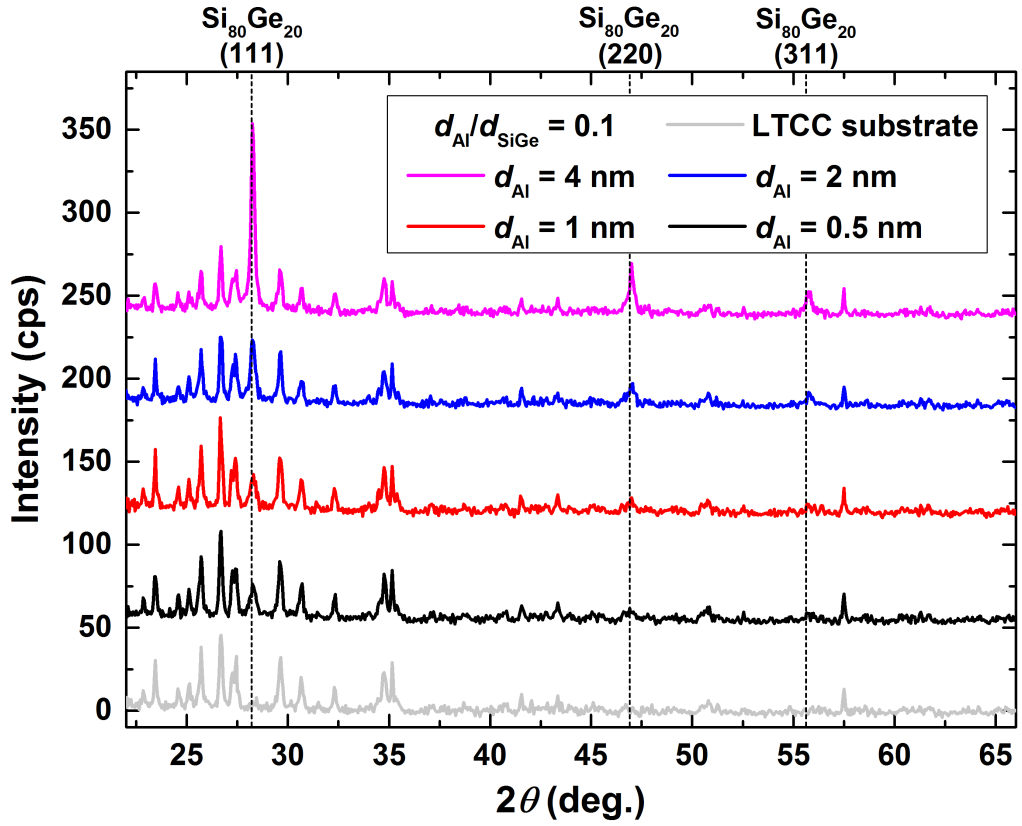


Figure 4.17: Comparison of the XRD ($\theta - 2\theta$) patterns for samples $[\text{Al}(d_{\text{Al}})/\text{Si}_{80}\text{Ge}_{20}(d_{\text{SiGe}})]_N/\text{LTCC}$ with fixed ratio $d_{\text{SiGe}}/d_{\text{Al}} = 0.1$ and different Al thicknesses d_{Al} after annealing at 873 K for 1 h. The theoretical diffraction peak positions for $\text{Si}_{80}\text{Ge}_{20}$ for the utilized Cu- K_α wavelength are indicated by dashed lines.

as the as-deposited samples showed no diffraction peaks except for LTCC substrate peaks. Every sample showed a $\text{Si}_{80}\text{Ge}_{20}(111)$ peak with only the $d_{\text{Al}} = 4$ nm sample clearly showing also the (220) and (311) peaks. Due to an mistake during deposition, this sample had double the total thickness of $2 \mu\text{m}$ for all combined SiGe layers compared to the other samples with $1 \mu\text{m}$ as the amount of bilayer repetitions was forgotten to be reduced by 2 from the prior deposition. Therefore, due to more crystalline SiGe being present, the intensity of the SiGe peaks is distinctively increased. The relative intensity of the SiGe peaks matches the expected values for untextured, polycrystalline SiGe. With this, it can be concluded that from a microstructure point of view no differences for the MIC process can be observed, regardless if the catalytic

Al is present in the form of continuous layers or nanodots.

4.2.2 Transport properties during MIC phase change

For the two previously discussed samples with fixed $d_{\text{Al}}/d_{\text{SiGe}}=0.1$ and the respective Al thickness $d_{\text{Al}} = 1 \text{ nm}$ and $d_{\text{Al}} = 4 \text{ nm}$, the resistivity was measured in-situ during annealing. Both samples were introduced to the HTS system in the as-deposited state and only resistivity measurements without Seebeck measurements were carried out. Electrical contacting of sample $[\text{Al}(1 \text{ nm})/\text{Si}_{80}\text{Ge}_{20}(10 \text{ nm})]_{100}/\text{LTCC}$ was rather difficult as the resistance of the sample was too high for a reliable measurement at the beginning. The driving current I_{ctrl} sent through the sample had to be reduced significantly down to at least $I_{\text{ctrl}} = 10^{-5} \text{ A}$ before any reasonable values could be obtained. The resistivity as function of temperature for this sample is shown in fig. 4.18a). At the beginning, a resistivity of more than $1 \text{ }\Omega\text{m}$ is observed while steadily decreasing to $10^{-1} \text{ }\Omega\text{m}$ at 650 K . The applied driving current I_{ctrl} is shown in the inset and highlights that shortly after starting the measurement I_{ctrl} had to be reduced down to 10^{-6} A by the automatic current adaption of the HTS system indicating that contacts were not completely stable for this measurement. This is also illustrated by several kinks and jumps over the course of the resistivity measurement. As the resistivity decreased during the annealing process, the driving current I_{ctrl} was increased accordingly. At 650 K the resistivity started to suddenly decrease stronger marking the beginning of the MIC phase change. The resistivity decreased down to $6 \cdot 10^{-4} \text{ }\Omega\text{m}$ at a temperature of 725 K . At this point, I_{ctrl} had also been increased to its maximum value of 10^{-3} A and stayed there for the rest of the measurement. Over the course of cooling down back to room temperature, the resistivity increases (except for two kinks due to contacts shifting) steadily up to $2 \cdot 10^{-3} \text{ }\Omega\text{m}$. The high resistivity values prior to the annealing procedure indicate insulating behavior and match the observed microstructure of an Al nanodot pattern, where only an amorphous, high resistance SiGe matrix can carry the electrical current. During the MIC phase change, the SiGe crystallizes and is also doped by the Al and, therefore, the resistivity is drastically lowered compared to the as-deposited state.

The MIC phase change was also observed for sample $[\text{Al}(4 \text{ nm})/\text{Si}_{80}\text{Ge}_{20}(40 \text{ nm})]_{50}/\text{LTCC}$ by an in-situ resistivity measurement shown in fig. 4.18b). Contrary to the other sample, the resistivity for this sample is close to be metallic with $\rho = 2.41 \cdot 10^{-5} \text{ }\Omega\text{m}$. Due to the initially low resistivity of this sample, contacting of this sample was easy, no jumps or kinks in measured resistivity values were observed, and I_{ctrl} could be kept at 10^{-3} A during the whole measurement. With increasing temperature, the resistivity started to increase slowly at the beginning up to $\rho = 2.48 \cdot 10^{-5} \text{ }\Omega\text{m}$ at 400 K . For higher temperatures, the rate of resistivity change increased drastically up to 530 K with a resulting maximum in resistivity of $8.94 \cdot 10^{-4} \text{ }\Omega\text{m}$. Afterwards the resistivity decreased steadily down to $9.37 \cdot 10^{-5} \text{ }\Omega\text{m}$ at 800 K . During subsequent

cooling down, the resistivity increased to $1.74 \cdot 10^{-4} \Omega\text{m}$. After reaching its maximum in resistivity, the temperature dependence is qualitatively the same for both samples. The metal like resistivity at the beginning of the annealing is no surprise, as continuous Al layers were found by TEM imaging for this sample in the as-deposited state. During MIC phase change, the multilayer structure is destroyed by diffusion and replaced by an Al doped polycrystalline SiGe matrix. The origin of the observed resistivity maximum during the MIC process will be discussed in the following paragraphs.

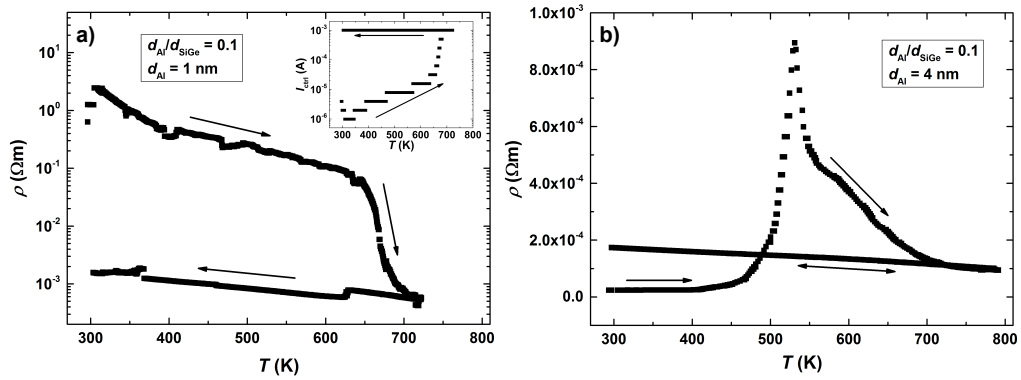


Figure 4.18: In-situ resistivity measurements in the HTS system of samples a) $[\text{Al}(1 \text{ nm})/\text{Si}_{80}\text{Ge}_{20}(10 \text{ nm})]_{100}/\text{LTCC}$ and b) $[\text{Al}(4 \text{ nm})/\text{Si}_{80}\text{Ge}_{20}(40 \text{ nm})]_{50}/\text{LTCC}$ during MIC phase change [114]. The inset in a) highlights the current I_{ctrl} sent through the sample over the course of the annealing procedure.

Another in-situ measurement run for sample $[\text{Al}(4 \text{ nm})/\text{Si}_{80}\text{Ge}_{20}(40 \text{ nm})]_{50}/\text{LTCC}$ was performed in the HTS system presented in fig. 4.19, but this time the resistivity and Seebeck coefficient were measured simultaneously for two sample pieces. The course of the resistivity is qualitatively the same like in the previous in-situ measurement except that the resistivity now exhibits a steplike behavior. This steplike behavior due to the measurement procedure results in the resistivity maximum now appearing as a sharp peak at 484 K. The Seebeck coefficient has a value of $-3 \mu\text{V}/\text{K}$ and stays in this range up to 450 K. The Seebeck coefficient then suddenly increases with ongoing annealing to a value of $91 \mu\text{V}/\text{K}$ at 480 K. After this transition, the Seebeck coefficient exhibits a completely reversible linear increase with increasing temperature typical for degenerated semiconductors. The range of the Seebeck coefficient is $65 \mu\text{V}/\text{K}$ at 350 K up to $172 \mu\text{V}/\text{K}$ at 710 K. The steplike course of the measured resistivity is caused by the simultaneous Seebeck measurement. To create an alternating temperature gradient to the sample piece of the Seebeck measurement, one of the heaters holds its designated temperature until the other heater overtakes

by a certain temperature threshold and the roles are reversed repeatedly. As the sample piece of the resistivity measurement is heated by one of these two heaters, the course of the temperature applied to it is of steplike nature and is reflected in the measured resistivity values. This means that every time a step is observed in the resistivity, the sample changes its resistivity due to structural changes despite temporarily constant temperature. This is in agreement to MIC theory, since after the activation temperature of MIC is reached, only time is needed to complete the phase change and higher temperatures only increase the rate of crystallization. The MIC phase change started regarding the in-situ resistivity measurement for the sample with $d_{\text{Al}} = 1$ nm at least at 650 K. The first irreversible resistivity change for the sample with $d_{\text{Al}} = 4$ nm appeared around 400 K. Reduction of the onset temperature for activation of the MIC process with increasing Al thickness has been reported repeatedly [80][73][74] and will be discussed in detail for another sample series in section 4.2.4.

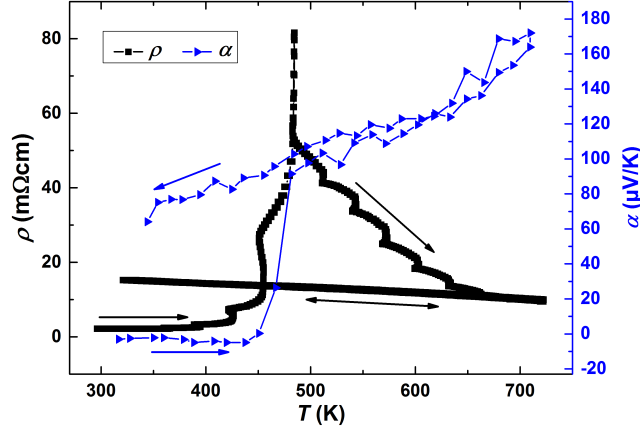


Figure 4.19: Simultaneous measurement of resistivity and Seebeck coefficient for sample $[\text{Al}(4 \text{ nm})/\text{Si}_{80}\text{Ge}_{20}(40 \text{ nm})]_{50}/\text{LTCC}$ [115].

After transition to the increased Seebeck values, it is safe to assume that all continuous Al layers have been dissolved by diffusion via the MIC phase change, since - in analogy to eq. (2.65) - the Seebeck coefficient of a material with high electrical conductivity would outweigh the Seebeck coefficient of low electrical conductivity materials if connected in parallel circuit. This again implies that before this transition is completed, continuous Al layers were still present and carrying the electrical current. It would be unreasonable to assume that pure Al changes its resistivity on such a scale. The observed irreversible steplike changes before the resistivity maximum have to be interpreted in a different way. The thickness of a sample investigated by van der Pauw measurement needs to be known for calculation of the resistivity using

eq. (3.10). If the Al layers start to dissolve, their thickness will decrease over time despite a constant layer thickness being assumed for the calculation. This leads to an increasing overestimation of the resistivity the more the Al layers are thinned out by diffusion. This changes at the very moment when no more continuous Al layers are present. From this point on, the electrical current will be carried solely by the SiGe matrix. As the SiGe is still not fully crystallized at this point, the resistivity will start to decrease as the left over amorphous sample parts crystallize. The resistivity maximum, therefore, has to be treated as an measurement artifact caused by assuming an incorrect layer thickness for calculation of the resistivity. This becomes even more obvious when comparing to the measurement presented in fig. 4.18a) as the resistivity decreased monotonously while heating up. Furthermore, the thickness used for calculation of the resistivity was the combined nominal thickness of all SiGe layers $d_{\text{SiGe,tot}} = 2 \mu\text{m}$ for the measurement presented in fig. 4.19 over the whole measurement range. With this, the resistivity of the sample is overestimated by one order of magnitude at the beginning as $d_{\text{Al}}/d_{\text{SiGe}} = 0.1$. Compared to the resistivity of pure aluminum ($\rho_{\text{Al,RT}} = 2.687 \cdot 10^{-8} \Omega\text{m}$ [116]), the corrected resistivity at room temperature, $\rho = 2.15 \cdot 10^{-6} \Omega\text{m}$, at the beginning of the annealing procedure would still be two orders too high indicating that the effective thickness of a single Al layer is even lower than 4 nm most probably due to roughness and amorphization at the layer interfaces [115]. As the Al thickness and its changing rate caused by diffusion are not known, a recalculation of the affected measurement regions was not carried out.

The resistivity and Seebeck coefficients for all samples with $d_{\text{Al}}/d_{\text{SiGe}} = 0.1$ after annealing at 873 K for 1 h are shown in fig. 4.20a) and b), respectively. All samples

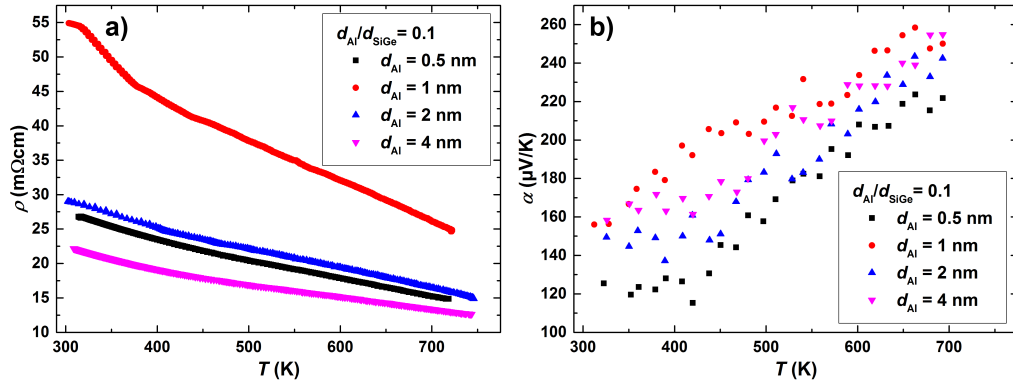


Figure 4.20: a) Resistivity and b) Seebeck coefficient for samples $[\text{Al}(d_{\text{Al}})/\text{Si}_{80}\text{Ge}_{20}(d_{\text{SiGe}})]_N/\text{LTCC}$ with fixed ratio $d_{\text{SiGe}}/d_{\text{Al}} = 0.1$ and different Al thicknesses d_{Al} after annealing at 873 K for 1 h.

exhibit in principle the same resistivity and Seebeck coefficient for temperatures of 300 K to 750 K with values in the range of 10 mΩcm to 60 mΩcm and 120 μV/K to 260 μV/K, respectively. Solely the measured resistivity of the sample with $d_{\text{Al}} = 1$ nm is roughly double the value compared to the other samples. The only possible explanation for this outlier at this point could be given by the previously discussed general morphology of the thin films with trenches perhaps having a stronger statistical influence on the electrical transport for this sample. Nevertheless, it is evident that the resulting transport properties in general are not affected by whether the sample starts with Al nanodots or continuous layers as long as the ratio $d_{\text{Al}}/d_{\text{SiGe}} = 0.1$ remains fixed. The influence of the ratio $d_{\text{Al}}/d_{\text{SiGe}} = 0.1$ will be discussed in the next section.

4.2.3 Influence of the ratio Al:SiGe on the resulting transport properties after MIC phase change

In this section the influence of the ratio $d_{\text{Al}}/d_{\text{SiGe}}$ on the resulting transport properties after MIC phase change will be discussed. For this, a sample series with different d_{Al} but constant $d_{\text{SiGe}} = 10$ nm was prepared. First three samples with $d_{\text{Al}} = \{0.5; 0.7; 1\}$ nm were analyzed regarding their resistivity and Seebeck coefficient for the temperature range of 300 K to 750 K. The results of the resistivity measurement are shown in fig. 4.21a) with resistivity being in the range of 10 mΩcm to 180 mΩcm. All samples exhibit negative temperature coefficients for the resistivity while the absolute temperature coefficients becomes smaller for higher d_{Al} . Additionally, lower d_{Al} results in higher resistivity with $\rho(d_{\text{Al}} = 0.5 \text{ nm})$ being more than one

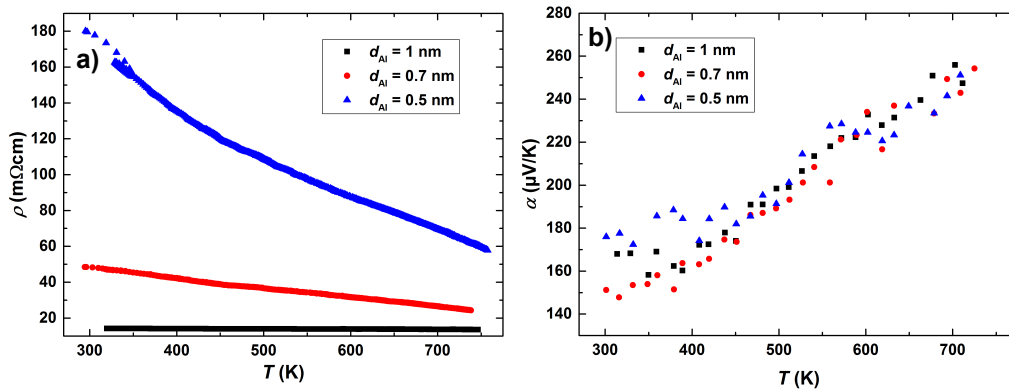


Figure 4.21: a) Resistivity and b) Seebeck coefficient for samples $[\text{Al}(d_{\text{Al}})/\text{Si}_{80}\text{Ge}_{20}(10 \text{ nm})]_{100}/\text{LTCC}$ with $d_{\text{Al}} = \{0.5; 0.7; 1\}$ nm after annealing at 873 K for 1 h [115].

order of magnitude larger than $\rho(d_{\text{Al}} = 1 \text{ nm})$ at room temperature. The Seebeck coefficient presented in fig. 4.21b) reveals the same values for all three samples. A positive, linear with temperature increasing Seebeck coefficient is observed ranging from $145 \mu\text{V/K}$ to $275 \mu\text{V/K}$. This is unexpected as resistivity and Seebeck coefficient normally both show the same sign for their temperature coefficients, because both are in general indirectly dependent on the charge carrier density. Hall measurements at room temperature revealed charge carrier densities in the range of $7 \cdot 10^{19} \text{ cm}^{-3}$ to $10 \cdot 10^{19} \text{ cm}^{-3}$ for these samples. The charge carrier density was also measured for the sample with $d_{\text{Al}} = 1 \text{ nm}$ in the low temperature regime in a cryostat system. A nearly temperature independent charge carrier density ranging from $8.0 \cdot 10^{19} \text{ cm}^{-3}$ to $9.5 \cdot 10^{19} \text{ cm}^{-3}$ is observed as shown in fig. 4.22. This together with the typical behavior of the Seebeck coefficient for a degenerately doped semiconductor (cf. eq. (2.68)) leads to the conclusion that the observed decrease in resistivity at elevated temperatures has to be caused by the charge carrier mobility, since intrinsic charge carrier excitation should be negligible up to at least 1100 K [110]. The decrease in resistivity for higher d_{Al} could be explained by the SiGe most likely not being fully crystallized as a ratio of $d_{\text{Al}}/d_{\text{SiGe}} = 1$ is needed for a complete MIC [71]. This is further supported by the data presented in table 4.3, where the resulting room temperature resistivity with respect to annealing temperature and Al thickness is compared. As the resulting room temperature resistivity decreases both for increasing annealing temperature and Al thickness for all samples, ratios of $d_{\text{Al}}/d_{\text{SiGe}} \leq 0.1$ appear to cause incomplete crystallization of the SiGe with amorphous parts most likely impairing the charge carrier mobility.

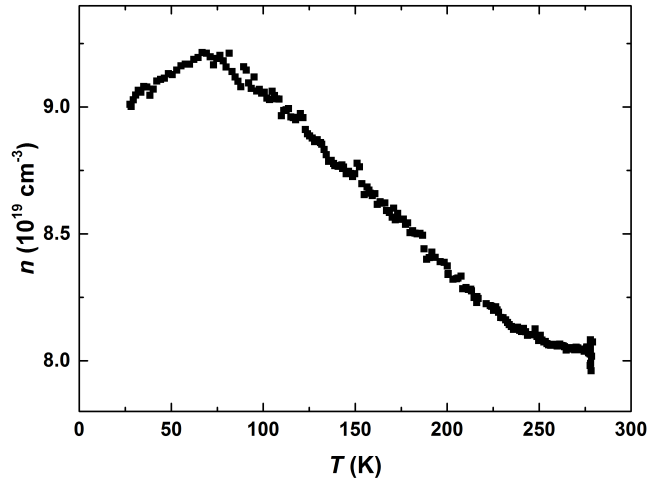


Figure 4.22: Low temperature measurement of the charge carrier density for sample $[\text{Al}(1 \text{ nm})/\text{Si}_{80}\text{Ge}_{20}(10 \text{ nm})]_{100}/\text{LTCC}$ after annealing at 873 K for 1 h .

Table 4.3: Room temperature resistivity ρ of samples $[\text{Al}(d_{\text{Al}})/\text{Si}_{80}\text{Ge}_{20}(10\text{ nm})]_N/\text{LTCC}$ depending on their Al thickness d_{Al} and applied annealing temperature T_{a} .

d_{Al} (nm)	resistivity ρ (m Ω cm)				
	as dep.	573 K	673 K	773 K	873 K
0.5	$> 10^6$	$> 10^6$	$> 10^6$	$4.1 \cdot 10^2$	$2.0 \cdot 10^2$
0.7	$> 10^6$	$> 10^6$	$3.5 \cdot 10^2$	$7.9 \cdot 10^1$	$4.5 \cdot 10^1$
1.0	$> 10^6$	$> 10^6$	$1.6 \cdot 10^2$	$4.1 \cdot 10^1$	$1.5 \cdot 10^1$

Since the Seebeck coefficient showed no dependency on the Al content for $d_{\text{Al}}/d_{\text{SiGe}} \leq 0.1$ and the resistivity decreased with increasing Al contents, the sample series with fixed $d_{\text{SiGe}} = 10\text{ nm}$ was continued with another set of samples to see how far the thermoelectric efficiency could be improved by increasing the ratio $d_{\text{Al}}/d_{\text{SiGe}}$. The chosen Al thicknesses were $d_{\text{Al}} = \{1; 2.5; 5; 7.5; 10\}$ nm such that ratios up to $d_{\text{Al}}/d_{\text{SiGe}} = 1$ were reached. The respective XRD patterns of these samples after being annealed at 873 K for 1 h are shown in fig. 4.23. XRD patterns of the as-deposited case are not shown, because no peaks except for substrate peaks could be detected. For $d_{\text{Al}}/d_{\text{SiGe}} = 0.1$, only a small (111)-peak of the SiGe phase was detectable further supporting the assumption of an incomplete crystallization of the SiGe for such low $d_{\text{Al}}/d_{\text{SiGe}}$. For higher $d_{\text{Al}}/d_{\text{SiGe}}$, the SiGe peak intensity increases, and in addition, the (220) and (311) SiGe peaks occurred, which indicates an increase in the fraction of crystalline SiGe. Please note that all SiGe peaks are slightly shifted to larger angles, which will be discussed in section 4.2.4 in detail.

As the Al content in the samples increases and the Al can only be redistributed in the thin film without being consumed, it is expected that the resulting transport properties will switch from semiconducting to metallic-like as metallic Al short circuits will remain after the MIC phase change. This is already highlighted by the comparison of the room temperature resistivity and Seebeck coefficient before and after annealing at 873 K for 1 h presented in table 4.4. In the as-deposited state, insulating behavior is observed for $d_{\text{Al}}/d_{\text{SiGe}} = 0.1$ as expected due to non continuous Al nanodots. An already metallic-like Seebeck coefficient is revealed for a ratio of $d_{\text{Al}}/d_{\text{SiGe}} = 0.25$, while the resistivity is still rather high being in the $10^2\text{ m}\Omega\text{cm}$ range most likely due to rather rough Al interlayers barely being continuous. For ratios of $d_{\text{Al}}/d_{\text{SiGe}} > 0.5$, clearly metallic-like values are observed for both the resistivity and Seebeck coefficient. After annealing, a change in transport properties to semiconducting behavior is obtained for ratios of $d_{\text{Al}}/d_{\text{SiGe}} = 0.1$ and $d_{\text{Al}}/d_{\text{SiGe}} = 0.25$. The respective samples exhibit resistivity and Seebeck coefficients in the order of $10^1\text{ m}\Omega\text{cm}$ and $10^2\text{ }\mu\text{V/K}$. Contrary to that, all samples with ratios of $d_{\text{Al}}/d_{\text{SiGe}} \geq 0.5$ exhibit after annealing nearly metallic-like values in the range of $\rho < 1\text{ m}\Omega\text{cm}$ and $S < 20\text{ }\mu\text{V/K}$. This is

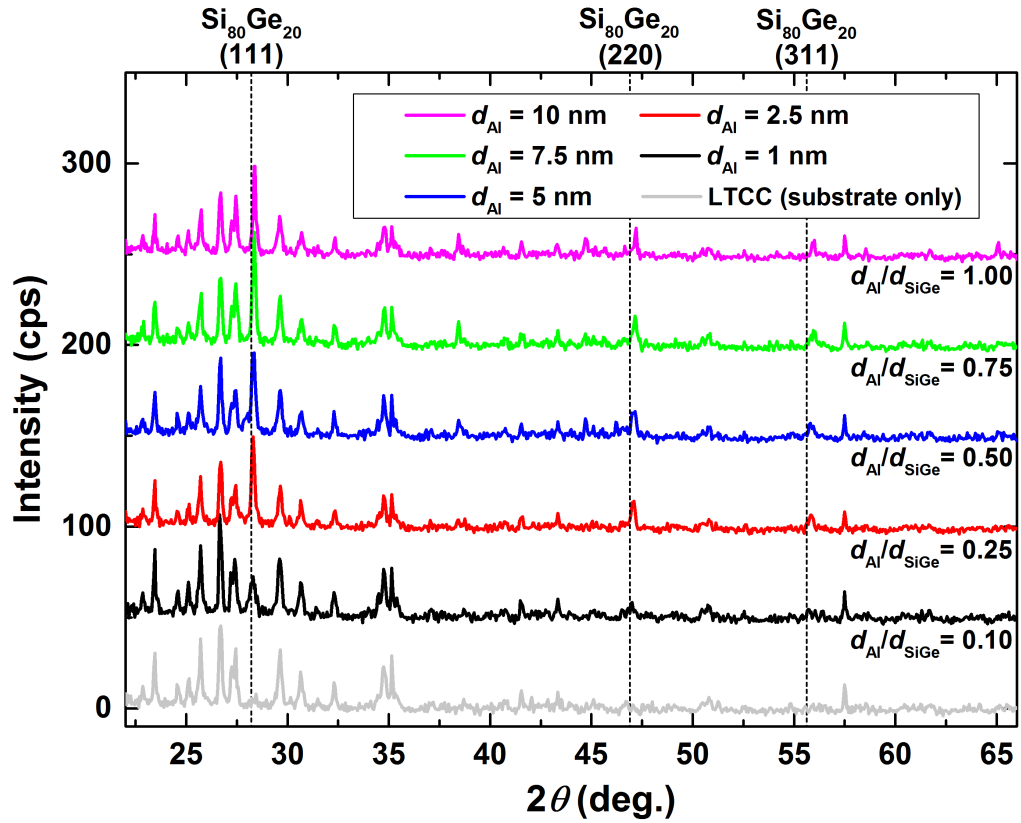


Figure 4.23: Comparison of the XRD ($\theta-2\theta$) patterns of samples with different ratios of $d_{\text{Al}}/d_{\text{SiGe}}$ [115]. The theoretical diffraction peak positions for $\text{Si}_{80}\text{Ge}_{20}$ for the utilized Cu- K_{α} wavelength are indicated by dashed lines.

another proof for the diffusive dissolution of the continuous Al layers during the MIC phase change. If the ratio $d_{\text{Al}}/d_{\text{SiGe}}$ is kept low enough, an Al-doped, crystalline SiGe matrix with isolated Al clusters can be expected after annealing. For higher $d_{\text{Al}}/d_{\text{SiGe}}$ ratios though, the amount of Al cannot be fully redistributed and thus excess Al forms electrical short circuits. The semiconducting transport properties of the Al-doped SiGe are then masked by the presence of these Al short circuits. Regarding those results, the switching point between semiconducting and metallic-like transport properties after MIC phase change is expected to be in the range of $0.25 \leq d_{\text{Al}}/d_{\text{SiGe}} \leq 0.5$.

Table 4.4: Room temperature resistivity and Seebeck coefficient of samples with different ratios of $d_{\text{Al}}/d_{\text{SiGe}}$ in the as-deposited state and after annealing at 873 K for 1 h.

Sample		As-deposited		Annealed (873 K, 1 h)	
d_{Al} (nm)	$d_{\text{Al}}/d_{\text{SiGe}}$	ρ (m Ω cm)	S (μ V/K)	ρ (m Ω cm)	S (μ V/K)
1	0.1	$> 10^6$	>100	55.70	152
2.5	0.25	194.5	2	13.29	124
5	0.5	0.17	2	0.69	17
7.5	0.75	0.05	1	0.64	12
10	1	0.03	1	0.16	7

The sample with $d_{\text{Al}}/d_{\text{SiGe}} = 0.5$ was chosen to test how far the MIC was completed during annealing at 873 K for 1 h. The already annealed sample was introduced to the HTS system for further resistivity and Seebeck measurements. The course of temperature of the annealing procedure is presented in fig. 4.24a). The measurement was divided into four intervals. Intervals (I) and (III) were used for annealing at a constant temperature of 740 K for 3 h and 48 h, respectively. Seebeck measurements were conducted during intervals (II) and (IV). The maximum temperature for interval (II) was chosen to be 475 K, because first deviations from the expected linear behavior of a metallic-like resistivity occurred at a temperature of 520 K during interval (I). For higher temperatures, a deviation from the metallic temperature dependence of the resistivity was observed as a stronger than linear change with temperature and, to not induce any irreversible changes during interval (II), the temperature was kept lower. The evolution of the resistivity for the whole annealing process with respect to the applied temperature is shown in fig. 4.24b). The resistivity of the already annealed sample started at 0.6 m Ω cm at room temperature and increased to 1.3 m Ω cm when reaching 740 K with the largest change occurring for temperatures above 650 K. While holding the temperature at 740 K for 3 h, the resistivity increased further to 1.6 m Ω cm. For the following cooling and heating virtually no temperature dependence of the resistivity was observed during interval (II). After the

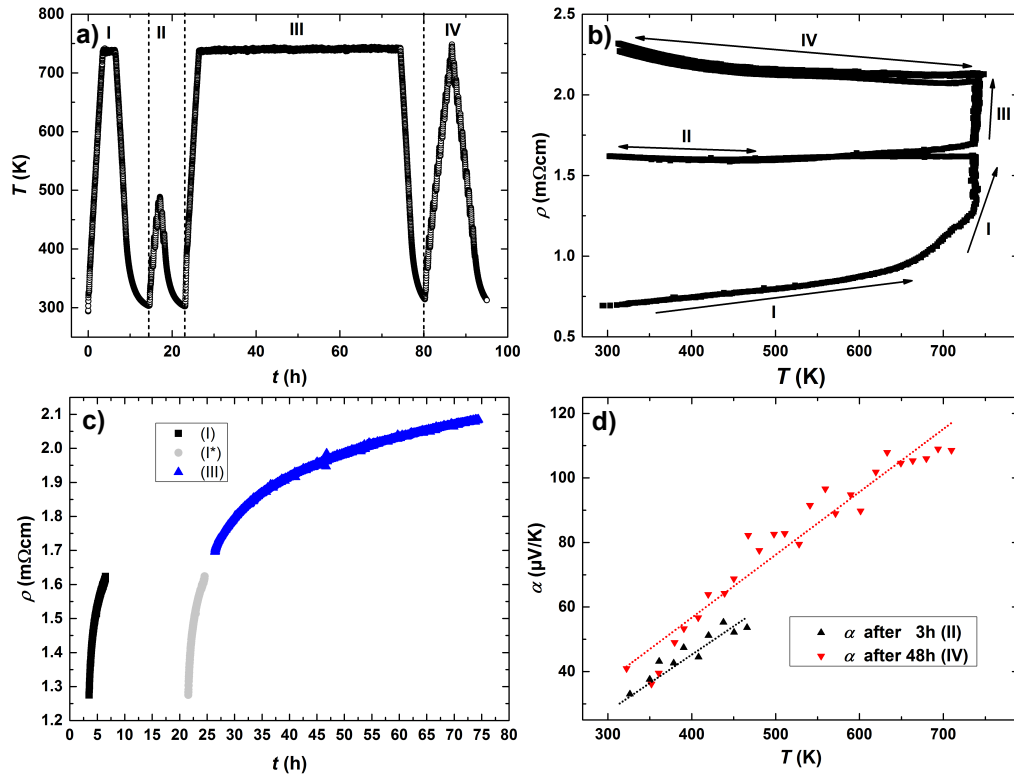


Figure 4.24: Measurements performed on an already at 873 K for 1 h annealed sample $[\text{Al}(5 \text{ nm})/\text{Si}_{80}\text{Ge}_{20}(10 \text{ nm})]_{100}/\text{LTCC}$ in the HTS system. a) Course of the applied temperature with separation into four measurement intervals (I)-(IV) [115]. b) Measured resistivity for the whole annealing process with respect to the four measurement intervals [115]. c) Change of resistivity with time at constant, maximum annealing temperature of 740 K during measurement intervals (I) and (III). (I*) represents the data of section (I) shifted in time with respect to the elapsed time during interval (II). d) Measured Seebeck coefficients for measurement intervals (II) and (IV) with dashed lines as guides to the eye [115].

sample was reheated to 740 K for interval (III), the resistivity kept increasing until reaching 2.2 mΩcm after 48 h of annealing. The resistivity finally exhibits a negative temperature coefficient during interval (IV). The change of resistivity with respect to the elapsed time while being annealed at the maximum temperature of 740 K during intervals (I) and (III) is displayed in fig. 4.24c). Only the parts where the temperature is kept constant at 740 K of intervals (I) and (III) are shown. The time of interval (II) leads to a shift in between the two parts on the time axis. The measured data of interval (I) was, therefore, shifted with respect to the elapsed time of interval (II) and indexed with (I*). A small gap between the data of (I*) and (III) is observed due to the sample also changing during the MIC process of the cooling and heating parts of (I) and (III), respectively. Neglecting this, a continuously slowing down resistivity change is revealed. The saturation for the resistivity can be estimated to lie in between 2.2 mΩcm and 2.3 mΩcm. Because of the small and diminishing resistivity change, the measurement was not continued after interval (IV), despite another increase in resistivity during interval (IV) indicating a still incomplete MIC transformation. The results of the Seebeck measurement are presented in fig. 4.24d). At room temperature, the Seebeck coefficient increases from 17 μV/K to 26 μV/K and 38 μV/K after intervals (II) and (IV), respectively. Additionally, a general increase of the Seebeck coefficient for extended annealing times is observed, but still being distinctively lower than the values of the samples presented in fig. 4.21b). This still ongoing increase in resistivity and Seebeck coefficient can be interpreted as the still unfinished dissolution of Al layers and thus a change from metallic to semiconducting behavior.

Another piece of sample [Al(5 nm)/Si₈₀Ge₂₀(10 nm)]₁₀₀/LTCC was used for long time

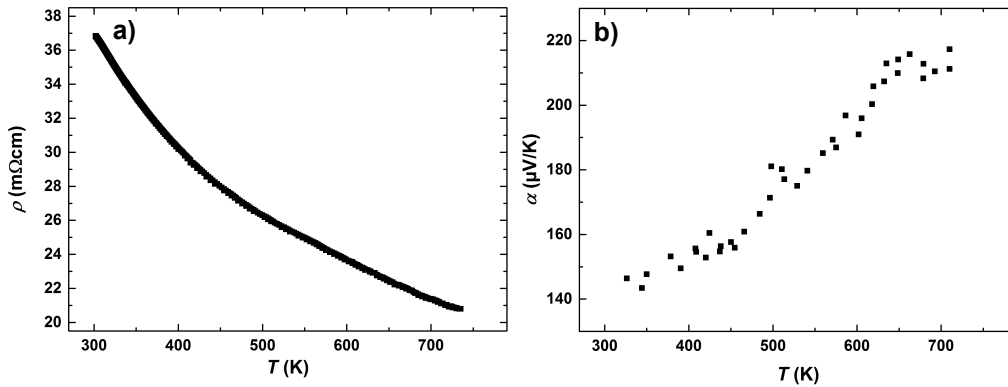


Figure 4.25: Measured a) resistivity and b) Seebeck coefficient of sample [Al(5 nm)/Si₈₀Ge₂₀(10 nm)]₁₀₀/LTCC after annealing at 873 K for 70 h [115].

annealing in a quartz tube furnace. Annealing time and temperature were increased to 873 K and 70 h, respectively. The resistivity and Seebeck coefficient of this sample are shown in fig. 4.25. At room temperature, the resistivity and Seebeck coefficient are 37 m Ω cm and 140 μ V/K, respectively. This sample with $d_{\text{Al}}/d_{\text{SiGe}} = 0.5$ has the same resistivity and Seebeck coefficient as the samples with $d_{\text{Al}}/d_{\text{SiGe}} = 0.1$ presented in fig. 4.20. The increase in annealing time from 1 h to 70 h is thus sufficient enough to dissolve the Al layers even for a ratio of $d_{\text{Al}}/d_{\text{SiGe}} = 0.5$. For the other two samples with $d_{\text{Al}}/d_{\text{SiGe}} \geq 0.75$, only metallic-like transport properties could be achieved even for this increased annealing time.

4.2.4 Influence of the Al thickness on MIC

The following section will cover the influence of the Al thickness d_{Al} on MIC itself with the discussion directly being quoted from [115]. In-situ x-ray diffraction measurements during annealing revealed a two-step process for the metal-induced crystallization of the SiGe layer, as was already observed by Knaepen et al. [73][74]. This process is shown for sample [Al(5 nm)/Si₈₀Ge₂₀(10 nm)]₁₀₀/LTCC in fig. 4.26a), where two distinctive steps in diffracted intensity for a diffraction angle of 33°, which corresponds to the SiGe(111) reflection, can be observed at temperatures of about 500 K and 750 K. The onset temperatures of the respective crystallization steps, $T_{\text{MIC},1}$ and $T_{\text{MIC},2}$, for samples with different d_{Al} are summarized in fig. 4.26b). A decrease for both onset temperatures is observed with increasing Al layer thickness and results in a saturation of $T_{\text{MIC},1} \approx 480$ K and $T_{\text{MIC},2} \approx 720$ K. The theory for this behavior was already shortly summarized in chapter 2.4. The inset in fig. 4.26b) highlights the beginning of the in-situ resistivity measurement during annealing of sample [Al(5 nm)/Si₈₀Ge₂₀(10 nm)]₁₀₀/LTCC previously presented in fig. 4.24. A dashed line was added as a guide to the eye to show the expected metallic linear dependence of the resistivity with temperature for the still continuous Al layers. Deviation from this expected behavior is observed for temperatures at about 520 K, which corresponds to the onset temperature of MIC ($T_{\text{MIC},1} = 515$ K) for this sample. This indicates that the irreversible changes observed in resistance are indeed due to diffusion caused by MIC. The second onset temperature $T_{\text{MIC},2}$ is generally about 150 K to 250 K higher than $T_{\text{MIC},1}$ and even exceeds the normal crystallization temperature of SiGe of roughly 950 K[117] with $T_{\text{MIC},2} = 1050$ K for $d_{\text{Al}} = 0.5$ nm. This second step was attributed by Knaepen et al.[73] to an increase in crystallization rate assisted by the occurrence of a liquid phase. As both Si and Ge form a eutectic system with Al, a liquid phase can be expected for temperatures higher than the respective eutectic temperatures $T_{\text{eut,SiAl}} = 850$ K and $T_{\text{eut,GeAl}} = 693$ K in such systems [65]. The decrease of crystallization temperature with d_{Al} saturates at about 720 K and is very close to the eutectic temperature of the GeAl system. Even though a Si₈₀Ge₂₀ composition is used in this work and therefore a eutectic temperature close to $T_{\text{eut,SiAl}}$

is expected, the actual value close to $T_{\text{eut,GeAl}}$ could be explained by fluctuations in the SiGe composition on the microscopic scale, such that sample parts with a locally higher Ge content would already melt at lower temperatures compared to the rest of the sample.

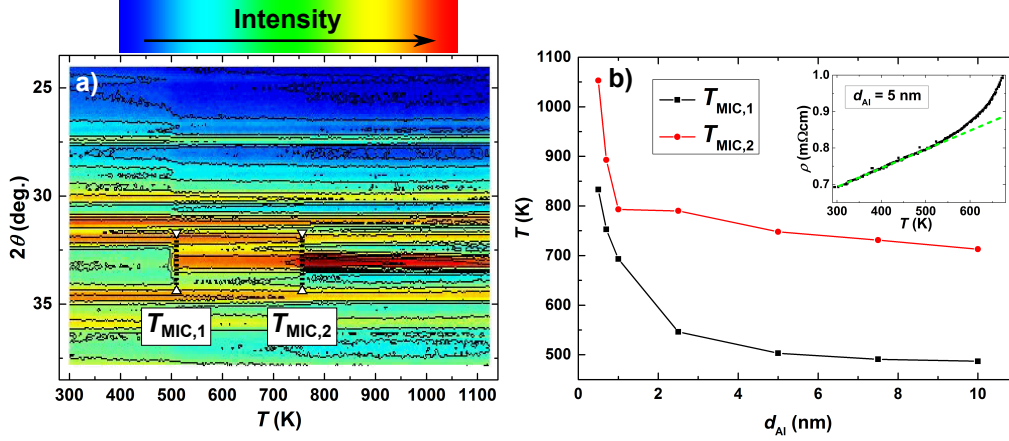


Figure 4.26: a) In-situ XRD (θ - 2θ) measurement during annealing of sample $[\text{Al}(5 \text{ nm})/\text{Si}_{80}\text{Ge}_{20}(10 \text{ nm})]_{100}/\text{LTCC}$ using a wavelength of 0.1797 nm [115]. b) Influence of the aluminum layer thickness on the crystallization temperature for the MIC process as measured by in-situ XRD during annealing [115]. The inset shows the beginning of the annealing process in the HTS system of the already annealed sample $[\text{Al}(5 \text{ nm})/\text{Si}_{80}\text{Ge}_{20}(10 \text{ nm})]_{100}/\text{LTCC}$ with the dashed line being a guide to the eye for the initial typical linear metallic resistivity dependence. The SiGe layer thickness was kept constant at 10 nm for all samples.

If parts of the sample are melting during annealing, a separation of SiGe phases with different compositions would be expected. The comparison of the diffraction patterns of sample $[\text{Al}(5 \text{ nm})/\text{Si}_{80}\text{Ge}_{20}(10 \text{ nm})]_{100}/\text{LTCC}$ obtained before and after annealing during the in-situ XRD measurements is shown in fig. 4.27. For both diffraction angles where $\text{Si}_{80}\text{Ge}_{20}$ peaks are expected, the emergence of a diffraction peak corresponding to $\text{Si}_{80}\text{Ge}_{20}$ after annealing is observed with a shift to higher angles. In reference to the just discussed possible local melting of the sample, this shift to higher angles would indicate a Si-enriched SiGe phase and thus an additional Ge-enriched SiGe phase shifted to lower angles should be present. Indeed, an increase in intensity is also observed for lower angles just left of the expected diffraction peaks of $\text{Si}_{80}\text{Ge}_{20}$, but is unfortunately superimposed by diffraction signals originating from the LTCC substrate making it impossible to clearly state if this change is due to the emergence of a second Ge-enriched SiGe phase. To clarify this matter, another set of samples

was prepared on ADS substrates. The comparison of diffraction patterns of sample $[\text{Al}(10\text{ nm})/\text{Si}_{80}\text{Ge}_{20}(10\text{ nm})]_{100}/\text{ADS}$ before and after annealing at 873 K for 1 h is shown in fig. 4.28a). No diffraction peaks due to the substrate are observed close to the expected $\text{Si}_{80}\text{Ge}_{20}$ peak positions. For better visibility, the difference between the two diffraction patterns is shown in fig. 4.28b). The SiGe diffraction peaks observed at angles around 28° and 47° clearly show a double peak and thus demonstrate the existence of two different SiGe compositions in this sample. Additionally, a crystalline Al phase is also detected after annealing by diffraction peaks at angles around 38° and 45° . Please note that double peaks for SiGe only appeared in diffraction patterns after annealing at 873 K for 1 h for samples with $d_{\text{Al}} \geq 5\text{ nm}$, which due to the fixed SiGe thickness d_{SiGe} of 10 nm for this sample series equals to $d_{\text{Al}}/d_{\text{SiGe}} = 0.5$. Regarding the values for $T_{\text{MIC},2}$, a phase separation for SiGe due to partial melting would be expected even for $d_{\text{Al}} \approx 1\text{ nm}$, since only for $d_{\text{Al}} \leq 0.7\text{ nm}$ does $T_{\text{MIC},2}$ exceed the applied annealing temperature of 873 K. However, the Ge-enriched SiGe phase exhibits significantly lower intensity compared to the Si-enriched phase and thus

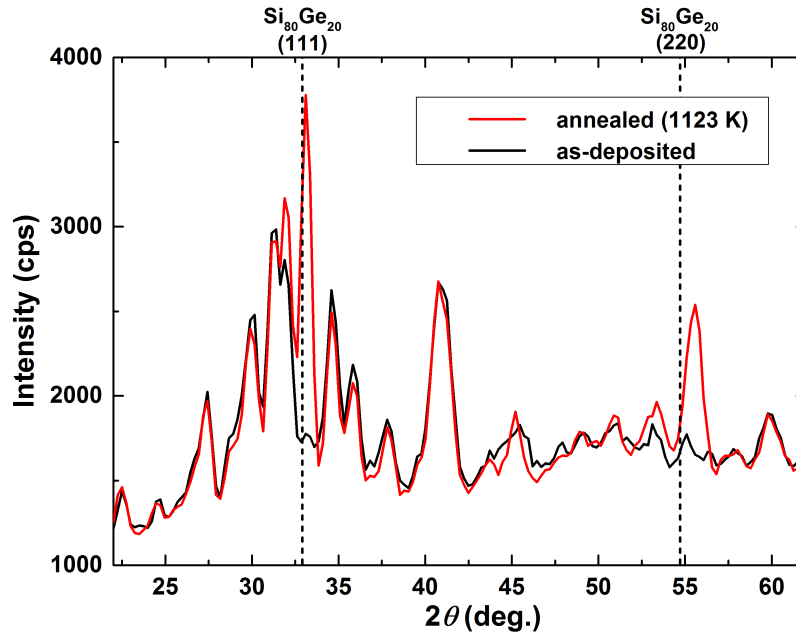


Figure 4.27: Comparison of the XRD ($\theta - 2\theta$) patterns of sample $[\text{Al}(5\text{ nm})/\text{Si}_{80}\text{Ge}_{20}(10\text{ nm})]_{100}/\text{LTCC}$ before and after the annealing process up to 1123 K. The theoretical diffraction peak positions of $\text{Si}_{80}\text{Ge}_{20}$ for the utilized wavelength of $\lambda = 0.1797\text{ nm}$ are indicated by dashed lines [115].

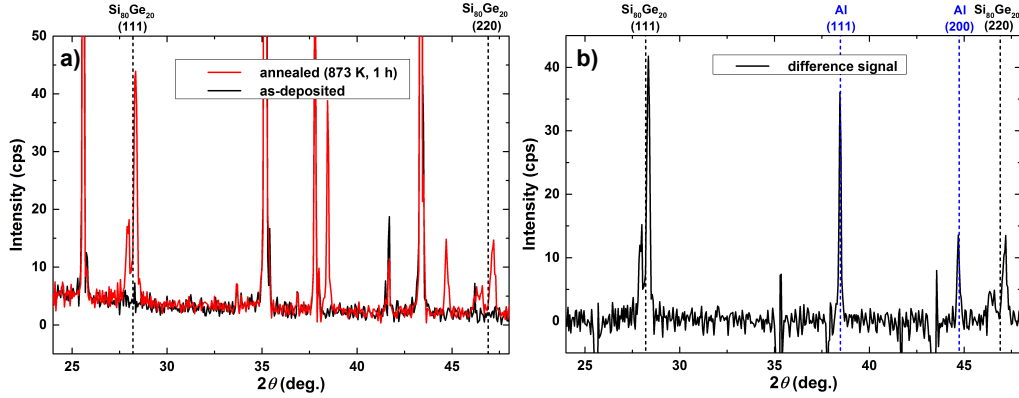


Figure 4.28: a) Comparison of the XRD ($\theta - 2\theta$) patterns of sample $[\text{Al}(10\text{ nm})/\text{Si}_{80}\text{Ge}_{20}(10\text{ nm})]_{100}/\text{ADS}$ before and after annealing at 873 K for 1 h [115]. b) Difference of the two diffractions patterns presented in a). The respective theoretical diffraction peak positions of $\text{Si}_{80}\text{Ge}_{20}$ and Al for the utilized $\text{Cu-K}\alpha$ wavelength are indicated by dashed lines [115].

might not be detectable by XRD due to the limited MIC for lower Al thickness. The presence of multiple compositional phases might be of advantage, providing a possible route for further improving the thermoelectric figure of merit for $\text{Si}_{1-x}\text{Ge}_x$ systems by reducing the thermal conductivity without impairing the electrical properties as demonstrated for $\text{Si}_{1-x}\text{Ge}_x$ bulk systems with different compositional phases [118].

4.2.5 Thermal conductivity measurements

Thermal conductivity measurements via the 3ω -method were first tried for samples deposited on LTCC substrates. A ratio of $d_{\text{Al}}/d_{\text{SiGe}} = 0.1$ was chosen for all samples here, as only detrimental effects for higher $d_{\text{Al}}/d_{\text{SiGe}}$ ratios were previously observed regarding the electrical transport properties. It was measured that the LTCC substrates only have a thermal conductivity in the range of $1\text{ Wm}^{-1}\text{K}^{-1}$ to $2\text{ Wm}^{-1}\text{K}^{-1}$. With that, LTCC would be a good candidate for practical application of thermoelectric thin film SiGe as the thermal conductivity of modern nanostructured SiGe typically is around $2\text{ Wm}^{-1}\text{K}^{-1}$ [26][43]. Hence, LTCC would not cause a thermal short circuit along the substrate and the heat would be transferred through the thermoelectric active thin film SiGe. Unfortunately, it is a prerequisite for the 3ω -method while measuring thin films that the thermal conductivity of the substrate is distinctly bigger than the thin film's thermal conductivity (cf. chapter 3.9), which is not the case for LTCC and SiGe. Therefore, no measurements of samples deposited on

LTCC substrates could be measured via the 3ω -method. The ADS and sapphire substrates however were suitable due to their higher thermal conductivity. Another problem that occurred was the large surface roughness of the samples deposited on ADS substrates (, which had the same morphology as LTCC substrates). A comparison of the prepared lithography for 3ω measurements for samples deposited on ADS or sapphire substrates is shown in fig. 4.29. The lithography in the case of sapphire substrates is in general continuous with only rare and isolated spots not impairing the measurement circuits. For ADS substrates though, the coarse grained surface structure is problematic as the measurement circuits prepared by lithography are quite thin and thus tend to not be continuous for such large surface roughness as can be seen by many darker edges of coarse grains interrupting the bright conduction channel. This technical difficulty led to only one ADS sample being measurable. The results of the 3ω measurements are presented in fig. 4.30. The thickness used for calculation of the thermal conductivity was the nominal thickness of the whole multilayer, so of all SiGe and Al layers combined. Samples in the as-deposited state have thermal conductivity around $1.4 \text{ Wm}^{-1}\text{K}^{-1}$ at room temperature exhibiting direct proportionality to the applied temperature with respect to the analyzed temperature range of 200 K to 330 K. As the 3ω -method measures the cross-plane thermal conductivity, the presence of continuous in-plane Al layers is of negligible influence. Most of the sample is amorphous SiGe permeated by Al layers most likely adding additional thermal resistance and thus resulting in such low values. After annealing, the samples exhibit thermal conductivity in the range of $2.4 \text{ Wm}^{-1}\text{K}^{-1}$ to $3.0 \text{ Wm}^{-1}\text{K}^{-1}$ at room temperature. Again the thermal conductivity increases linearly with temperature as expected for this temperature range. The measured thermal conductivities are directly comparable to values of typical nanostructured SiGe [26][43].

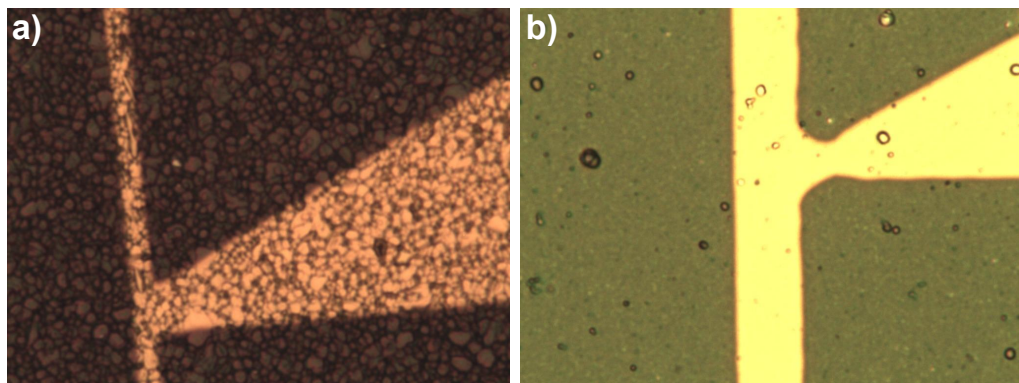


Figure 4.29: Optical microscope images of the surface of 3ω samples deposited on a) ADS and b) sapphire substrates. Parts of the lithography are recognizable as bright structures.

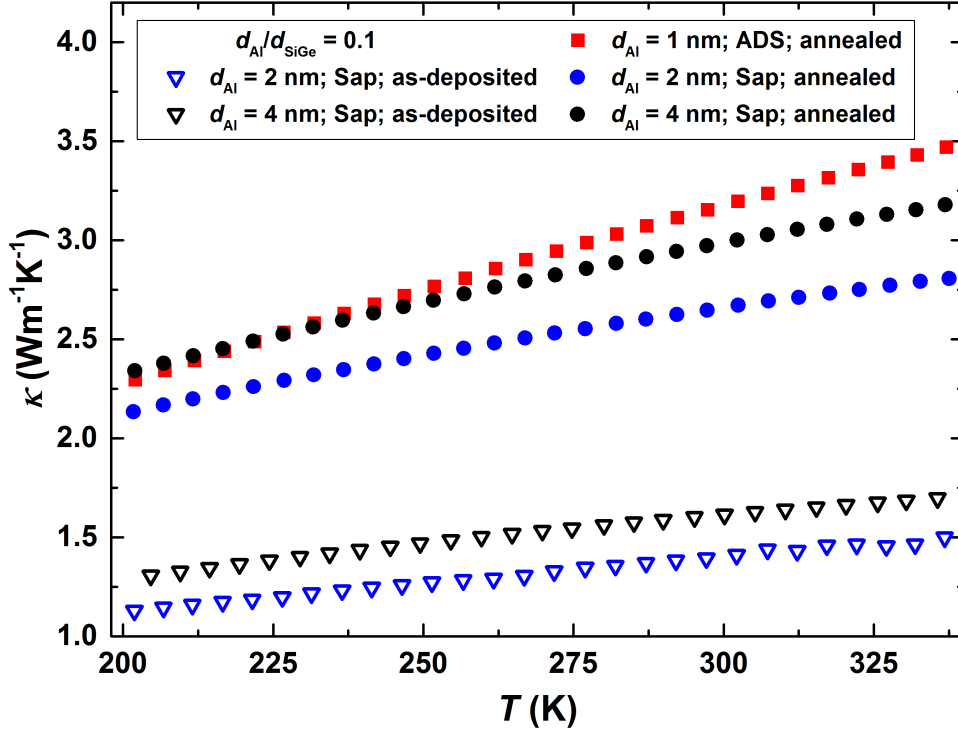


Figure 4.30: Thermal conductivity of various multilayer samples $[\text{Al}(d_{\text{Al}})/\text{Si}_{80}\text{Ge}_{20}(d_{\text{SiGe}})]_{100}$ deposited onto either ADS or sapphire substrates measured in the as-deposited state and after annealing at 873 K for 1 h. The ratio $d_{\text{Al}}/d_{\text{SiGe}}$ was kept constant at 0.1 for all samples.

4.3 Characterization of SiGe/Al systems on silicon oxide substrates

In the previous chapter, it was shown that on the one hand a sufficient amount of Al has to be present to guarantee a complete MIC for the SiGe, but on the other hand too much Al results in detrimental, metallic-like thermoelectric properties. Therefore, a solution regarding the excess of Al has to be found. The approach taken here revolves around the reduction of SiO_2 by Al, which had affected the first samples deposited onto thermally oxidized Si by penetrating the SiO_2 isolation layer. Due to the electrical connection of the thermoelectric SiGe thin film and the Si substrate, intrinsic carrier excitation led to unfavorable thermoelectric properties in this case. This chapter will discuss the properties of Al-SiGe systems

deposited onto quartz glass, which will be simply denominated as SiO_2 . The goal is to have the excess of Al react with the SiO_2 substrate after the MIC for the SiGe has taken place. The samples deposited on SiO_2 are no more of multilayer form, but are either in the form of a bilayer $\text{Si}_{80}\text{Ge}_{20}(200\text{ nm})/\text{Al}(d_{\text{Al}})/\text{SiO}_2$ or a trilayer $\text{Si}_{80}\text{Ge}_{20}(100\text{ nm})/\text{Al}(d_{\text{Al}})/\text{Si}_{80}\text{Ge}_{20}(100\text{ nm})/\text{SiO}_2$ with d_{Al} ranging from 20 nm to 700 nm. As the SiGe thickness and substrate is kept the same in each case, nomenclature in the form of TL:Al20nm will be used: first indicating whether a bilayer (BL) or trilayer (TL) stack was used and afterwards the nominal Al thickness d_{Al} in nm.

Furthermore, the following new samples were analyzed after the transition of the HTS system to operate under N_2 atmosphere instead of vacuum improving the thermal coupling during Seebeck measurements (cf. chapter 3.8). Therefore, the systematic underestimation in Seebeck values of 20% to 25% is not in effect anymore. The results presented in this chapter were acquired by Anna Zera in the frame of her master thesis [119].

4.3.1 Reduction of silicon oxide by aluminum

Prior to the main experiments of this chapter, the feasibility of the reduction of SiO_2 by Al was tested. For this, a 200 nm thick Al layer was deposited on a SiO_2 and ADS substrate. As ADS is an Al_2O_3 based ceramic, no reduction should take place for this system. The respective XRD patterns are compared in fig. 4.31. In the as-deposited state, no peaks (except for ADS substrate peaks) could be observed in both cases. The reason for no Al peaks being detectable is not understood, but probably is only due to the Al having too small crystallites. Thermally evaporated Al was once analyzed by XRD as a comparison and revealed a clearly visible Al (111) peak (not shown) indicating that the sputter deposited Al in this work simply is x-ray amorphous. After the 200 nm thick Al layers had been annealed at 873 K for 1 h, a Si (111) peak could be detected for the Al film deposited on the SiO_2 substrate while additional peaks were observed in the case of the ADS substrate. As only the Si (111) peak was detected after annealing the Al layer on SiO_2 , the reduction of SiO_2 to Si by Al seemed to be successful. The Al_2O_3 based ADS substrate was as expected inert regarding this reduction.

4.3.2 Structural Characterization

Rutherford Backscattering Spectrometry

Samples with an Al thickness d_{Al} of 20 nm and 200 nm were characterized via RBS. Individual layer thicknesses were increased to the prior multilayer samples since sensitivity of RBS was too low to resolve the individual layers as Si and Al are hardly distinguishable due to their similar mass. The RBS spectra for both the BL and TL

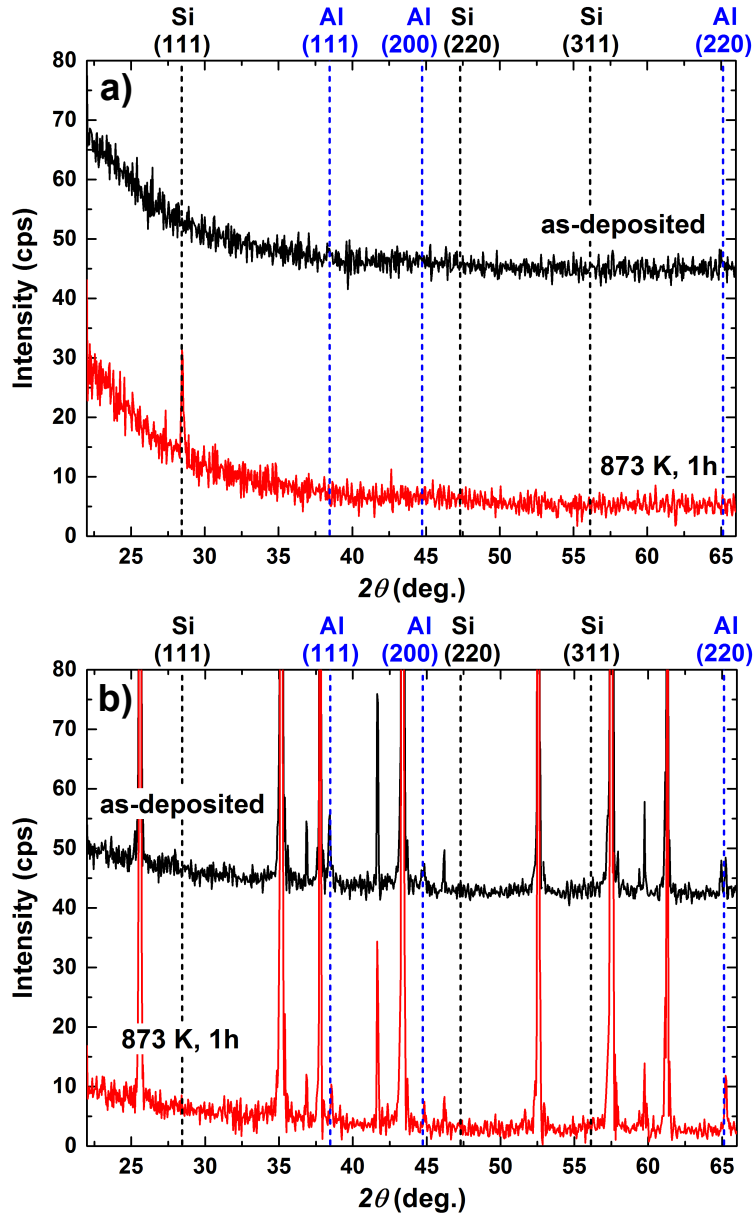


Figure 4.31: XRD ($\theta - 2\theta$) patterns of a 200 nm Al layer deposited on a) SiO₂ and b) ADS taken in the as-deposited state and after annealing at 873 K for 1 h. Dashed lines indicate the respective theoretical diffraction angles.

sample with $d_{\text{Al}} = 200$ nm in the as-deposited state are shown in fig. 4.32. Here, the individual contributions of each element were added to give the reader information about where to expect the respective elements in the following spectra. The elements appear starting from high energies in order from heaviest to lightest: Ge, Ar, Si, Al, O.

The Ge peak starts around 1350 keV and is not divided for the BL sample whereas the TL sample reveals an expected double peak for Ge due to the two separated SiGe layers. Following starts the Ar peak at around 1100 keV. The Ar peak also has double peak form for the TL sample while the BL sample has a single peak. As the width of the Ar peaks is the same as of the Ge peaks, the Ar was most likely only integrated during the sputtering of SiGe. The Ar content was lower than 3% for all samples. Additionally to Ar, O could be detected in the SiGe layers at around 5% content. The source of this oxygen contamination is unknown. Normally the peaks of Si and Al would lie very close to each other. The start of the Al peak, though, is shifted to lower energies as in both cases SiGe is deposited on top of the Al and thus causing an energy loss for all ions scattered at Al atoms. This shifting leads to a perceived double peak for Si and Al between 700 keV to 1000 keV as the Al and Si contributions only partly overlap for both samples. The simulated profile matches the measured values for the region of the deposited BL and TL. For energies lower than 450 keV, an increasing spread between simulated and experimental values is observed as multi-scattering events taking place at such low energies are not accounted for in the simulation.

Next, the structural changes due to annealing at 873 K for 1 h will be discussed with

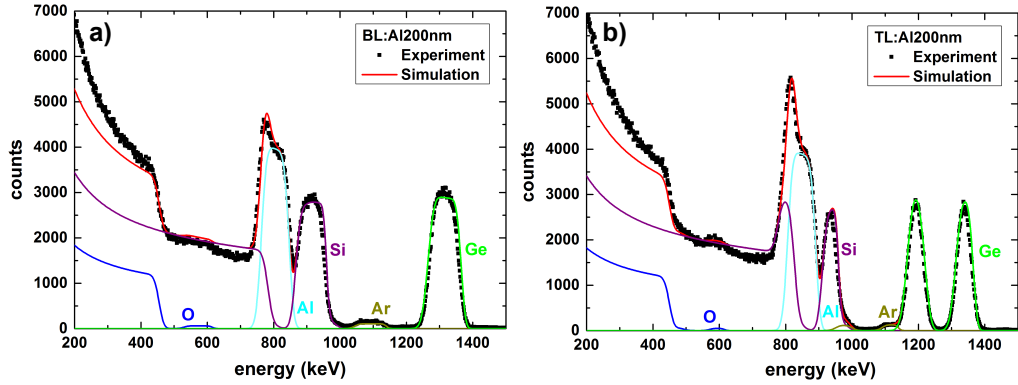


Figure 4.32: Comparison of the measured and simulated RBS spectra for a) BL and b) TL sample with $d_{\text{Al}} = 200$ nm in the as-deposited state. The respective contributions of each element are indexed in the graph by different colors.

respect to the measured RBS spectra. The comparison between as-deposited state and after annealing for the BL:Al20nm sample is shown in fig.4.33a). In the as-deposited state, the individual Al, Si, and Ge peaks are clearly distinguishable. After annealing, the Al peak itself has merged with the Si peak in so far that a slowly decaying flank to lower energies of the Si peak is observed. This indicates that the Al and SiGe layers intermixed during the annealing. The in principal same behavior is observed for TL:Al20nm in fig. 4.33b). The only difference occurs in the as-deposited state in form of the double peak for Ge representing the two individual SiGe layers. The separation of the respective peaks is more pronounced when d_{Al} is increased to 200 nm as the energy loss due to more Al separates the individual Si and Ge peaks. Looking at the spectra presented in fig.4.33c), the spectra after annealing has way lower intensity compared to the as-deposited case for BL:Al200nm. This is due to a measurement error, where the total to be collected charge was set to 6 μC instead of the normally used 10 μC . Disregarding this, the intermixture of the Al and SiGe layers is again observed by the merging of the AL and Si peak, but additionally by the slow fading out of the Ge peak to lower energies, too. The SiO_2 substrate sets in at energies of 450 keV in the as-deposited state, while the starting energy for the substrate is around 550 keV after annealing. The same is observed for TL:Al200nm in fig. 4.33d). This shift of the substrate onset energy to higher energies indicates the intermixing of the Al-SiGe thin film and SiO_2 substrate. As the amount of Al available for the reduction of SiO_2 is way smaller for samples with $d_{Al} = 20$ nm than for $d_{Al} = 200$ nm, this intermixing is only resolvable for samples with higher Al amounts. Another small peak evolves around 600 keV after annealing for both BL:Al200nm and TL:Al200nm. This peak most likely indicates an accumulation of oxygen. TEM images revealed that not all of the produced Al_xO_y necessarily is located at the former substrate interface, but also remnants can be found on top of the SiGe film after annealing. This small oxygen peak around 600 keV is not observed for the samples with $d_{Al} = 20$ nm and is very likely related to the formation of Al_xO_y . An oxygen contamination during annealing can therefore be ruled out.

The thickness of the individual layers in the as-deposited state was also calculated via eq. (3.3) using the results of the RBS simulations. As the measured RBS profiles of the annealed samples are rather difficult to be simulated due to the intermixing of the layers, no analysis was carried out for this case. The comparison of the nominal individual layer thicknesses and the layer thicknesses determined by RBS is summarized in table 4.5. The SiGe layers show matching results with respect to measurement uncertainty. The Al layers, though, appear to be much thinner than their intended nominal thickness. This deviation could be influenced by the fact that Al and Si in general are hard to be distinguished via RBS, but more likely the Al deposition rate was simply overestimated during deposition test runs. The ratio of Si:Ge was determined to be 83:17 for all samples thus being more Si-rich than the nominal 80:20 ratio of the used $\text{Si}_{80}\text{Ge}_{20}$ sputter target.

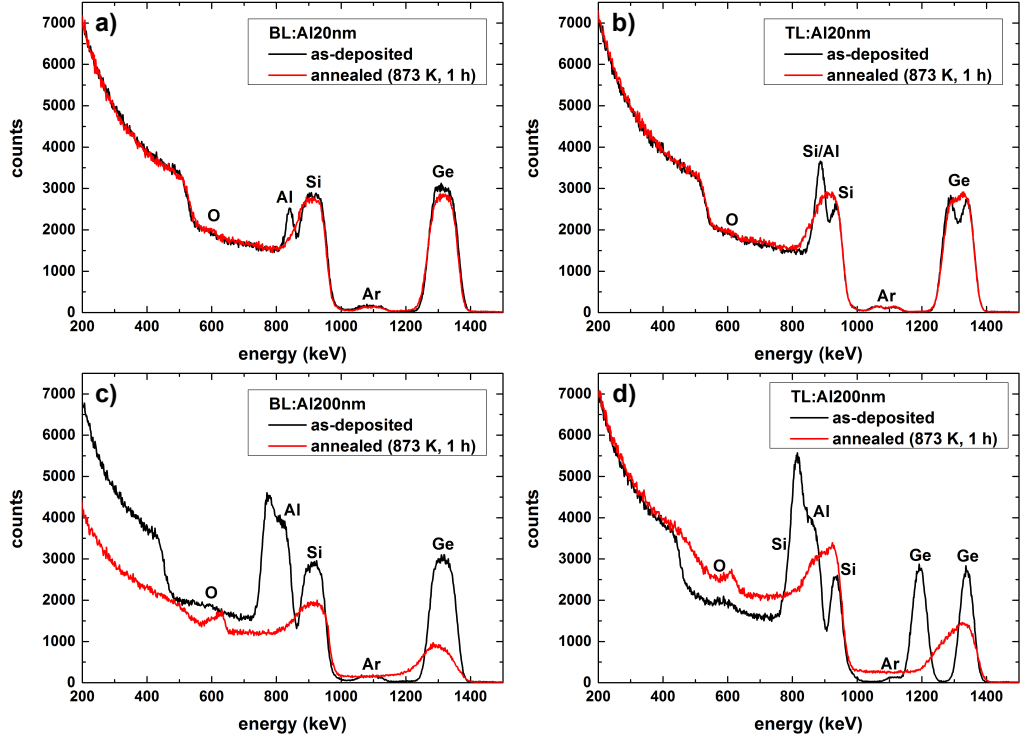


Figure 4.33: Comparison of the RBS spectra of a),c) BL and b),d) TL samples before and after annealing at 873 K for 1 h. The respective Al thicknesses were a),b) $d_{\text{Al}} = 20$ nm and c),d) $d_{\text{Al}} = 200$ nm.

Table 4.5: Comparison of the nominal individual layer thicknesses d_{Al} , and d_{SiGe} and the layer thicknesses $d_{\text{Al,RBS}}$, and $d_{\text{SiGe,RBS}}$ determined by RBS.

sample	d_{Al} (nm)	$d_{\text{Al,RBS}}$ (nm)	d_{SiGe} (nm)	$d_{\text{SiGe,RBS}}$ (nm)
BL:Al20nm	20	14	200	203
BL:Al200nm	200	166	200	203
TL:Al20nm	20	9	100	99
			100	106
TL:Al200nm	200	169	100	107
			100	105

X-Ray Diffraction

The series of BL and TL samples with different Al thickness d_{Al} was analyzed by XRD. The measured XRD patterns in as-deposited state are presented in fig. 4.34. Only few samples exhibited an Al (111) peak with no direct correlation to d_{Al} being apparent. As in the cases before, the Al appears to be x-ray amorphous as even a 700 nm thick Al film did reveal only faint Al peaks. No SiGe peaks were present in the as-deposited case as expected.

After the samples had been annealed at 873 K for 1 h, a peak near the $\text{Si}_{80}\text{Ge}_{20}$ (111) peak emerged for all samples except for $d_{\text{Al}} = 20$ nm for which the amount of Al was likely not sufficient for a successful MIC. This is shown in fig. 4.35. The intensity of the peak increased with increasing d_{Al} even though the total SiGe thickness is 200 nm for all samples highlighting an increase in diffracting material. Interestingly, no other peaks are detected even though the intensity of the observed $\text{Si}_{80}\text{Ge}_{20}$ (111) peak is high enough to expect at least also a noticeable peak regarding the $\text{Si}_{80}\text{Ge}_{20}$ (220) reflex. The SiGe thus appears to be strongly (111)-textured for these samples. A zoom in around 26° to 31° of the XRD patterns of the annealed samples is shown in fig. 4.36. An increasing shift of the $\text{Si}_{80}\text{Ge}_{20}$ (111) peak to higher angles with increasing d_{Al} is observed. This can be understood by the incorporation of further Si atoms released by the reduction of the SiO_2 substrate into the SiGe. As SiGe is a fully miscible crystal, the resulting lattice constant shifts towards a more Si rich SiGe alloy. Another sign for this can be found in the complete vanishing of the small Al peaks which previously were present. Through the reduction of SiO_2 by Al, the Al was oxidized and accordingly disappeared from the XRD patterns. The already for even low values of d_{Al} perceivable shift of the SiGe peaks to higher angles can be explained with the RBS results regarding the stoichiometry of the SiGe being $\text{Si}_{83}\text{Ge}_{17}$ in the as-deposited case.

The SiGe(111) peaks in the XRD patterns of the annealed BL and TL samples presented in fig. 4.36 were fitted with Gaussian fits to determine the center position and full width half maximum for each peak. The position of the SiGe(111) peak in dependency on d_{Al} is shown in fig. 4.37a). The shift to higher diffraction angles with increasing Al thickness becomes apparent again and in principle appears to be linear with increasing d_{Al} . Only the BL sample with $d_{\text{Al}} = 700$ nm deviates from the linear dependence. This is expected as the diffraction peak for pure Si is at 28.4422° (cf. table 3.2, [90]) while the SiGe(111) peak for sample BL:Al700nm is at 28.427° indicating that the SiGe layer at this point is almost only composed of Si. Furthermore, the full width half maximum of each peak was used to estimate the perpendicular SiGe grain size L_{gr} via Scherrer analysis using eq. (3.7). The estimation of L_{gr} reveals grain sizes increasing from 60 nm to 150 nm with d_{Al} in fig. 4.37b). The increase for L_{gr} is strongest for $d_{\text{Al}} \leq 100$ nm which equals to $d_{\text{Al}}/d_{\text{SiGe}} \leq 0.5$ for these samples with a fixed SiGe thickness of 200 nm and probably just highlights the

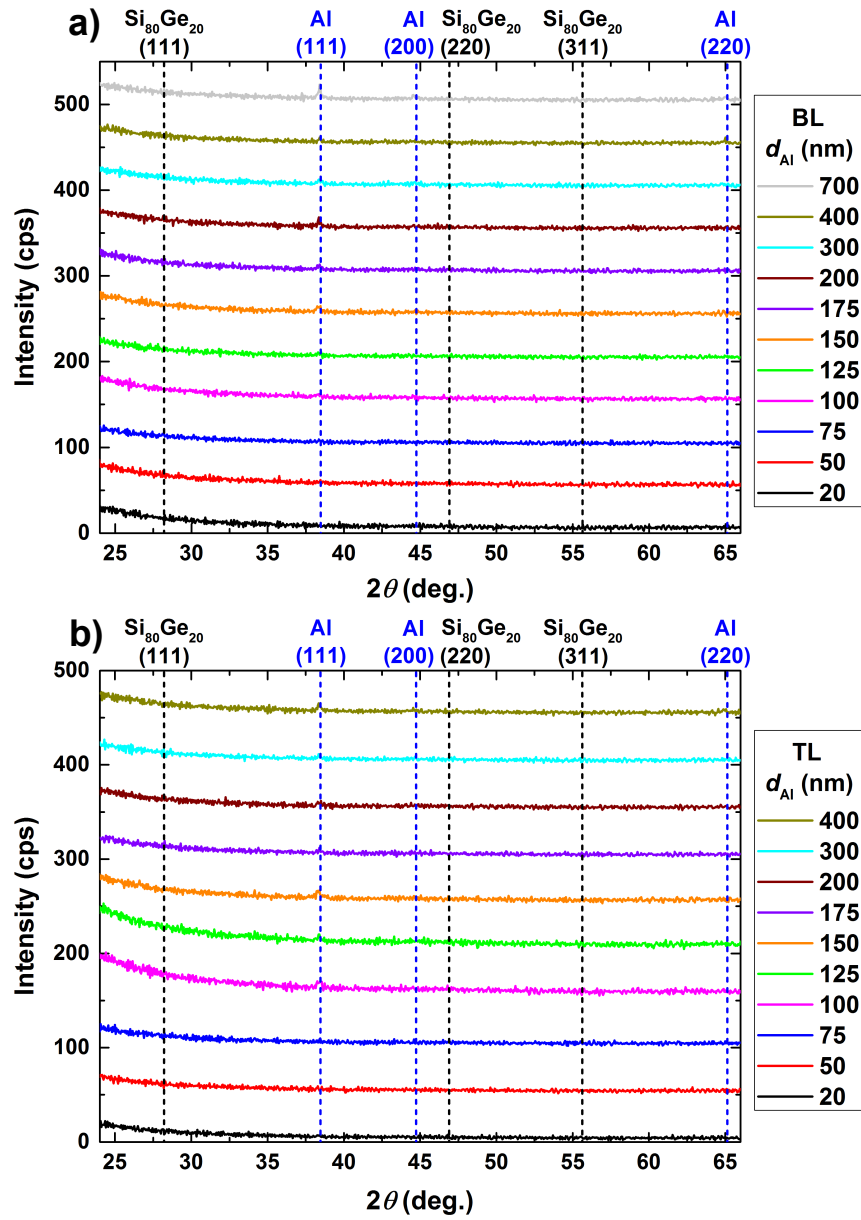


Figure 4.34: Comparison of the XRD ($\theta - 2\theta$) patterns for a) BL and b) TL samples with different d_{Al} in the as-deposited state. Dashed lines indicate the respective theoretical diffraction peak positions.

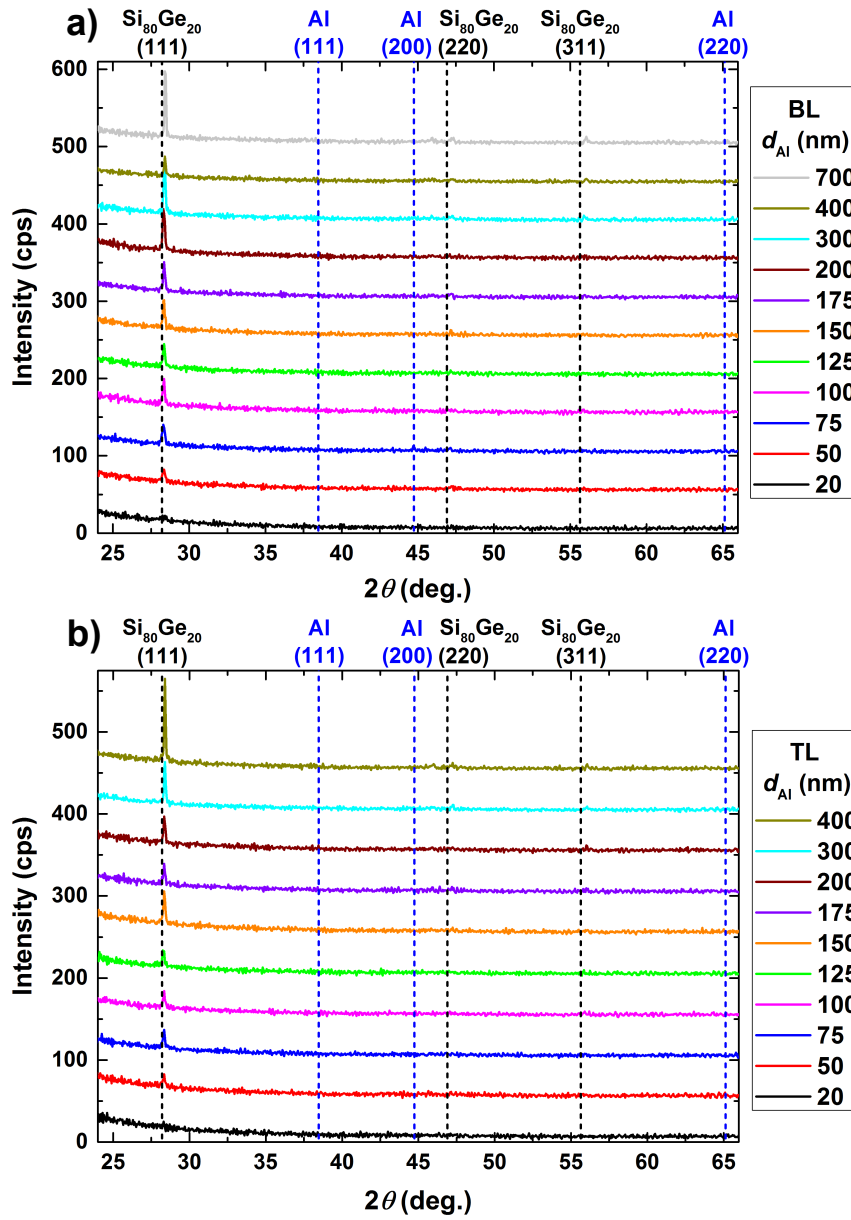


Figure 4.35: Comparison of the XRD ($\theta - 2\theta$) patterns for a) BL and b) TL samples with different d_{Al} after an annealing at 873 K for 1 h. Dashed lines indicate the respective theoretical diffraction peak positions.

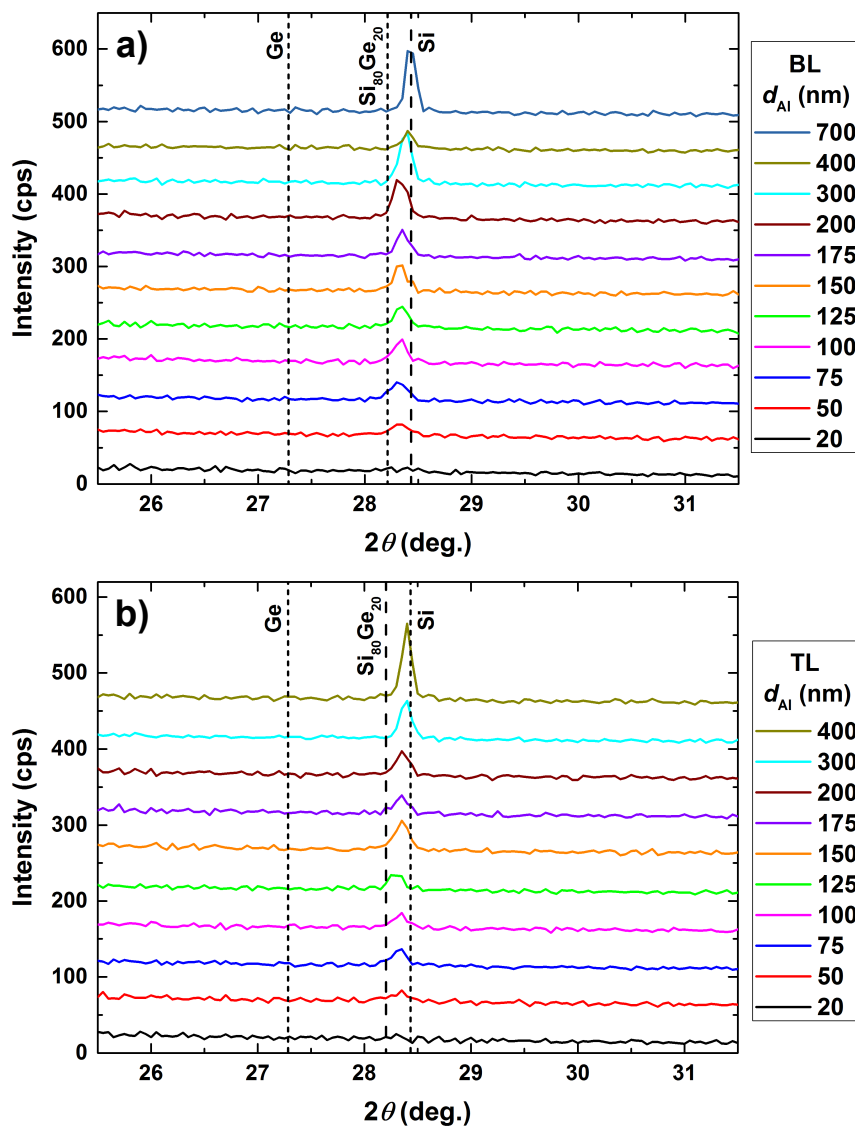


Figure 4.36: Comparison of the XRD ($\theta - 2\theta$) patterns zoomed in around 28° for a) BL and b) TL samples with different d_{Al} after an annealing at 873 K for 1 h. Dashed lines indicate the respective theoretical diffraction peak positions.

influence of insufficient amounts of Al impairing the MIC. In the range of $100 \text{ nm} \leq d_{\text{Al}} \leq 200 \text{ nm}$ ($0.5 \leq d_{\text{Al}}/d_{\text{SiGe}} \leq 1$), nearly no increase for L_{gr} is observed, which is unexpected at least for the BL samples as a continuous MIC of the whole 200 nm thick SiGe layer is expected for $d_{\text{Al}}/d_{\text{SiGe}} = 1$. The following increase in L_{gr} for samples with $d_{\text{Al}} \geq 300 \text{ nm}$ is probably only due to the noticeable increase in SiGe layer thickness to incorporation of Si atoms released by the SiO_2 reduction. These results show that the reduction of SiO_2 can be used to remove excess of Al after MIC without developing any thermoelectric detrimental secondary phases, but the composition of the SiGe shifts towards a more Si rich alloy. This (together with the increase in SiGe layer thickness) needs to be kept in mind as a sufficiently high enough Ge content is needed to lower the thermal conductivity by alloy scattering for SiGe and therefore a Ge-richer SiGe starting layer ought to be used accordingly.

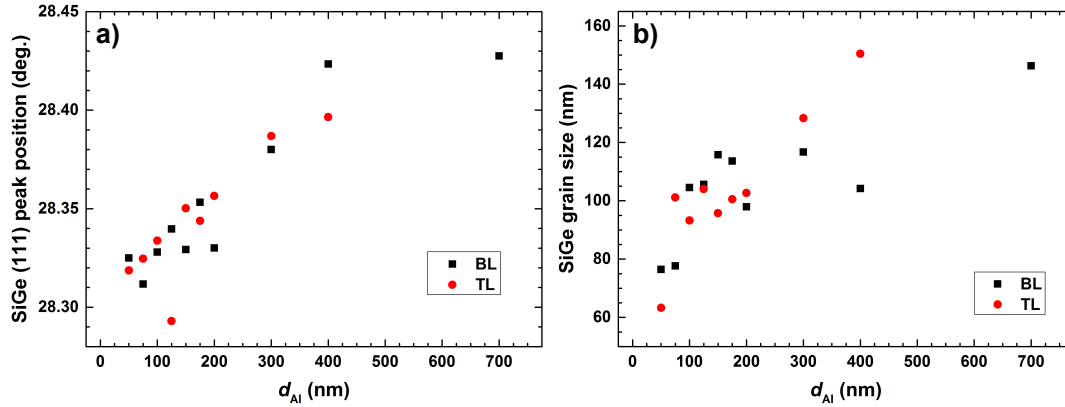


Figure 4.37: a) Center of the SiGe(111) peak position and b) results of Scherrer analysis for estimation of the SiGe grain size for the BL and TL samples after annealing at 873 K for 1 h as function of d_{Al} .

Transmission Electron Microscopy

The sample TL:Al200nm was analyzed by TEM. BF cross section images of the as-deposited state and after annealing at 873 K for 1 h are shown in fig. 4.38a) and b), respectively. The as-deposited state reveals three separate layers. The top and bottom layer appear to be of homogenous contrast while the middle layer has signs of added diffraction contrast. This matches the expectations as the SiGe should be amorphous and therefore appear homogenous. The bottom SiGe layer appears darker, as the prepared cross section becomes thicker in direction to the substrate due to its wedge shape. The origin of the dark dots at the interface to the substrate is unknown. Furthermore, such dots were observed for this sample only and could be

a simple preparation outlier. The diffraction contrast features of the Al layer indicate that the Al is in the crystalline state, which is a prerequisite for a successful MIC. The thicknesses of all layers are smaller than the nominal expected values with only 90 nm for the SiGe layers each and 175 nm for the Al layer. This matches the RBS results presented in table 4.5 with respect to the Al layer. Regarding the SiGe layers, RBS had predicted the SiGe thickness slightly above the nominal thickness values. As the both the TEM and RBS results do not deviate much from the nominal SiGe thickness, this discrepancy is most likely only due to measurement uncertainty. After the sample was annealed, the principal trilayer structure of the sample is still intact, but the thicknesses of each layer have changed. The outer layers are around 20 nm to 90 nm thick while the thickness of the middle layer increased to roughly 240 nm. Interestingly, SiGe and Al have switched places as could be shown via EDX elemental maps in fig. 4.39. The switching of the metal and semiconductor during MIC is a known side effect and called metal-induced layer exchange [71]. The oxidation of the Al was deduced by comparison of the elemental maps of Al and O, but no statements regarding the oxidation state of the Al_xO_y can be made as such elemental maps do not allow for a quantitative analysis. All three layers reveal signs of diffraction contrast and thus are in a crystalline state. At the bottom of the SiGe layer, a hole in the layer is present. This hole could be a TEM preparation artifact such that the layer thinned out faster at this particular spot than its surroundings. Another explanation could also be found in the reduction of the SiO_2 , as the density of the resulting reaction products is lower than the starting ones', which locally could lead to a material deficit resulting in holes.

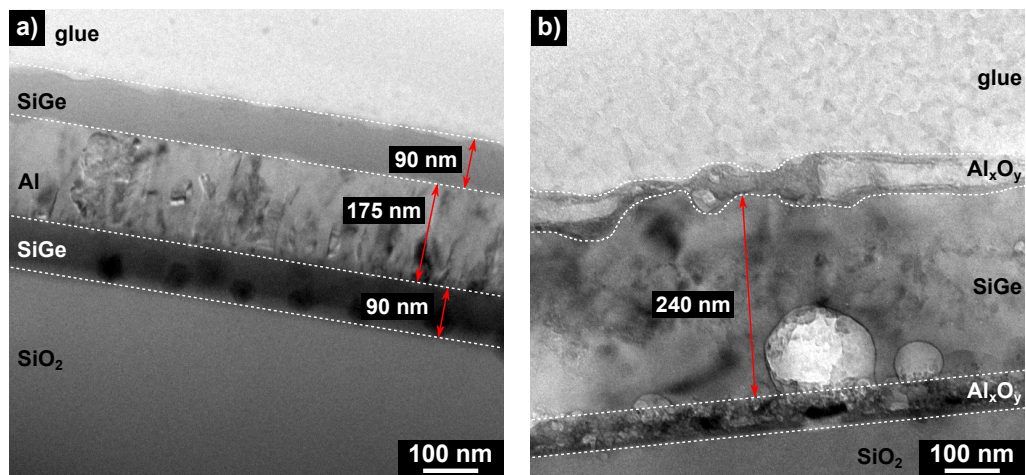


Figure 4.38: TEM BF cross section images of sample TL:Al200nm a) in the as-deposited state and b) after annealing at 873 K for 1 h.

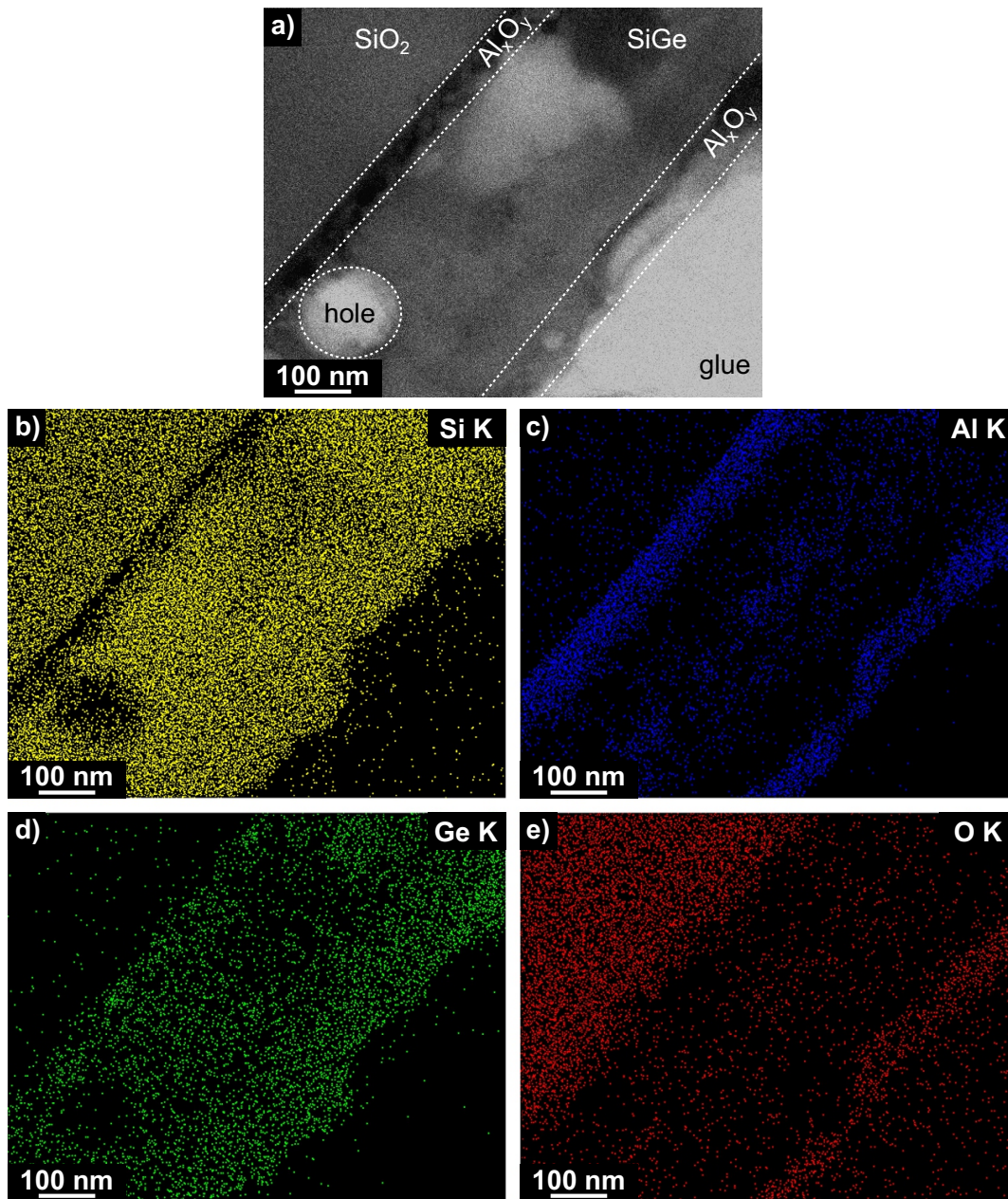


Figure 4.39: a) Secondary electron image of sample TL:Al200nm after annealing at 873 k for 1 h. Elemental maps for b) Si, c) Al, d) Ge, and e) O of the area observed in a).

The TEM analysis was repeated for sample BL:AL700nm. The high value of $d_{\text{Al}} = 700 \text{ nm}$ was chosen to undoubtedly highlight the increase of the thickness of the SiGe layer. The BF image of the as-deposited state is shown in fig. 4.40a). At first, three layers besides the substrate are discernible. Actually, the Al layer is divided into two parts as the deposition process of the Al layer was interrupted due to an error (without breaking the vacuum), which resulted in the apparent interface along the Al layer. Neglecting this additional interface, the expected layer stack can be observed. The SiGe layer thickness is 190 nm and close to the expected nominal thickness of 200 nm. The Al, though, is roughly 600 nm thick and thus again indicates that the Al deposition rate was overestimated. An overestimation of 10% to 15% appears reasonable regarding the RBS (compare table 4.5) and TEM results. After BL:Al700nm was annealed at 873 K for 1 h, the Al and SiGe switched positions partially. Only parts of the Al diffused to the top of the layer, where the SiGe was prior to the annealing, as the metal-induced layer exchange could only take place for an upper Al layer part equal to the thickness of the SiGe layer. The rest of the Al remained at the bottom next to the substrate. Interestingly, both parts of the Al were oxidized. The elemental maps for the Al near the SiO₂ substrate are shown in fig. 4.41. Here it becomes apparent that the top edge of the former SiO₂ substrate was completely replaced by Al_xO_y. The Al_xO_y appears to be dense and except for measurement noise shows no signs of remaining Si. The interface between the Al_xO_y and SiGe is quite rough. Apparently, a part of the Al_xO_y broke away from the main part of the Al_xO_y and can be seen as an isolated chunk at the bottom left of the images. This shows that even parts of the Al, which did not stay in direct contact to the SiO₂ substrate, could take part in the reduction and were accordingly oxidized. The thickness of the SiGe layer increased remarkably. As the top Al_xO_y layer was very rough and of discontinuous form, an exact value is hard to determine for the SiGe layer. The observed thickness for the SiGe layer was in between 270 nm to 520 nm. This thickness spread has to be kept in mind for all measurements which depend on the knowledge of the layer thickness.

The crystalline quality of the SiGe layer of sample BL:Al700nm after the MIC phase change and reduction of the excess Al was high as indicated by the observed lateral size of SiGe grains of several microns. In addition, no distinct border or gradient along the SiGe layer could be observed with respect to the released Si atoms of the SiO₂ reduction. A diffraction image of the SiGe layer is presented in fig. 4.42a). The image reveals a hexagonal-like diffraction pattern as expected for an incident beam along the [110] direction of a diamond lattice. Even faint Kikuchi lines are discernible in between the individual diffraction reflexes highlighting the high crystalline quality. The comparison with the theoretical diffraction pattern of a Si₈₀Ge₂₀ crystal is shown in fig. 4.42c). All diffraction reflexes match the theoretical pattern with even the forbidden reflexes also being present in the observed diffraction pattern. The presence of the forbidden reflexes could be explained by stress in the crystal lifting the extinction

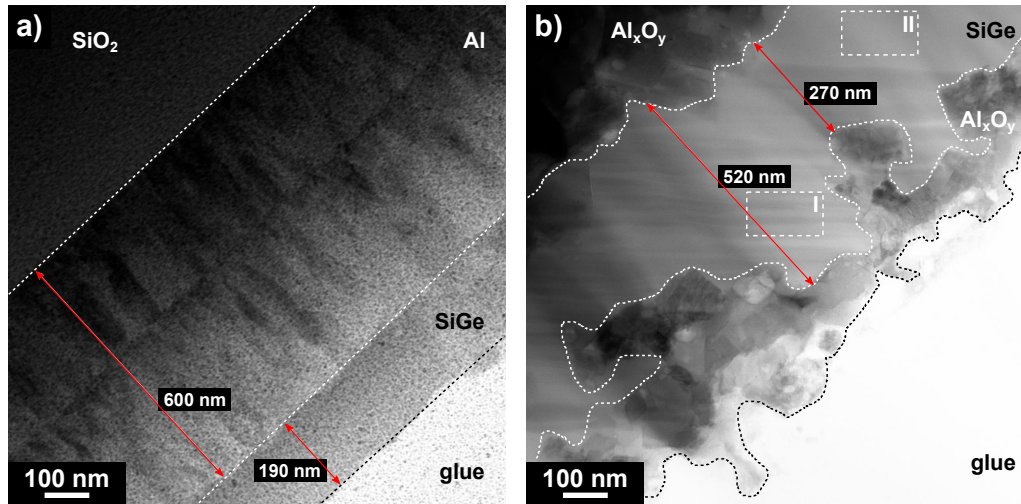


Figure 4.40: TEM BF cross section images of sample BL:Al700nm a) in the as-deposited state and b) after annealing at 873 K for 1 h. Boxes I and II mark areas of high and low twin grain boundary density, respectively.

rules or also by the crystal consisting of two different species of atoms and thus having different atomic factors also resulting in a lift of the extinction rules. Besides such pristine areas, another type of diffraction pattern was observed for the SiGe layer, which is shown in fig. 4.42b). Here, two hexagonal-like patterns are overlain with respect to a mirror axis. This is a typical diffraction pattern in the presence of twin grain boundaries. The mirror axis and the resulting two different hexagonal-like patterns are highlighted in fig. 4.42d). Such an area with several twin grain boundaries being present is shown in fig. 4.43. The individual twin grain boundaries and different orientations of the twin crystals are clearly discernible. The twin crystals connect seamlessly and the distance between two grain boundaries was typically around 1 nm to 20 nm. Such twin grained crystal structures hold high potential for thermoelectric application as phonons would easily be scattered along twin grain boundaries while electrons could pass those near freely. Looking back at fig. 4.40b), horizontal lines can be seen along the SiGe layer e.g. inside box I. These horizontal lines seem to be connected to Al_xO_y parts at the surface of the layer stack. It could be that this added contrast was caused by Al_xO_y creeping across the SiGe layer. Areas of the SiGe layer with such contrast like box I are of high twin grain boundary density while pristine SiGe parts like box II show nearly no twin grain boundaries. Further research is needed to discern how Al_xO_y is involved in the formation of twin grain boundaries. Nevertheless, twin grained microstructures were already reported for Si and SiGe deposited on sapphire substrates [120][121] and thus a connection between

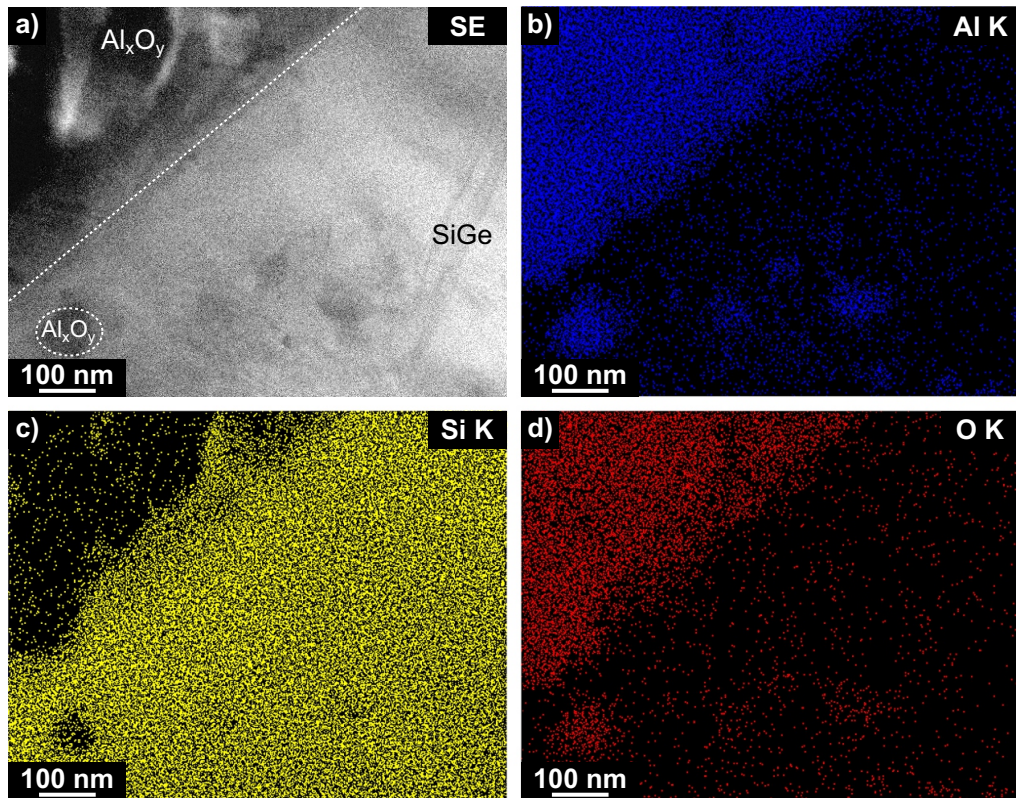


Figure 4.41: a) Secondary electron image of an area close to the substrate of sample BL:A1700nm after annealing at 873 k for 1 h. Elemental maps for b) Al, c) Si, and d) O of that area. The Ge signal is not shown, as the intensity was too low.

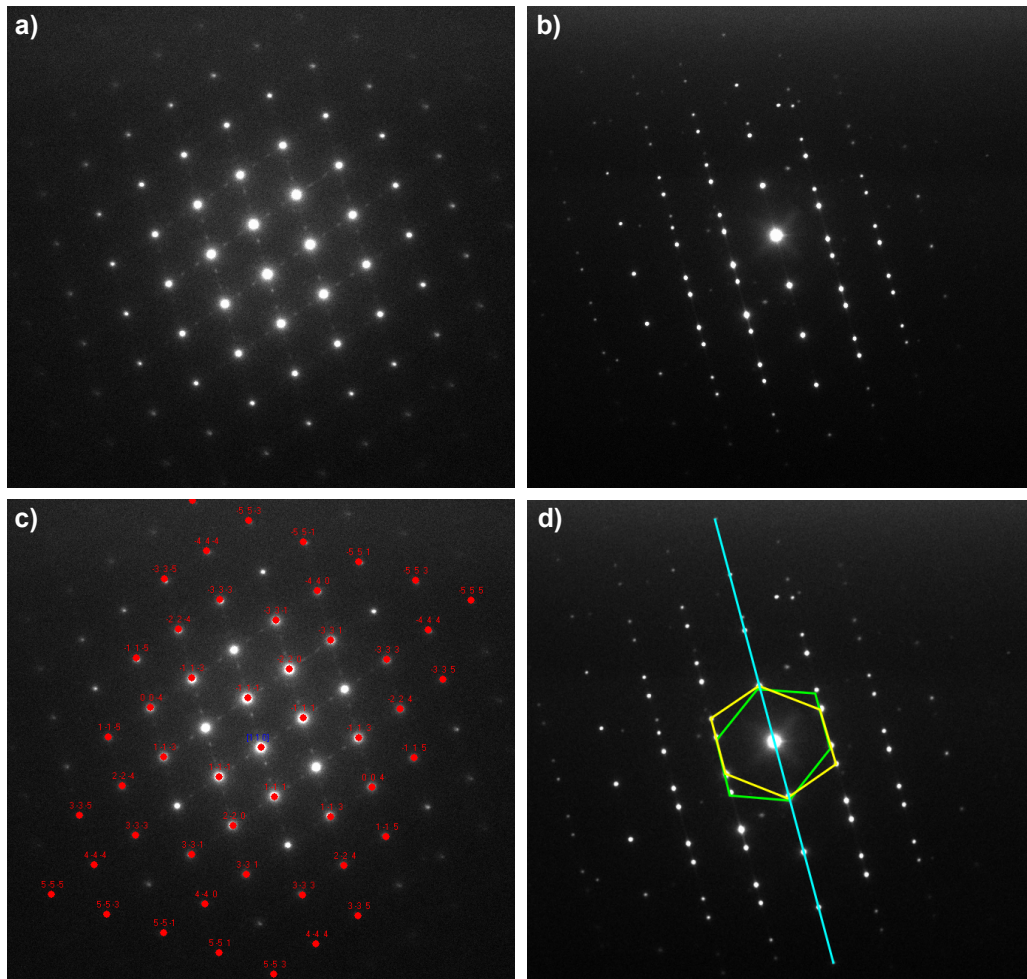


Figure 4.42: Diffraction images of sample BL:Al700nm after annealing at 873 K for 1 h taken in an area with a) low and b) high amount of twin grain boundaries. c) Overlay of the diffraction pattern shown in a) with a simulated diffraction pattern for a $\text{Si}_{80}\text{Ge}_{20}$ crystal with the incident beam along the [110] direction. d) Highlighted mirror axis and the resulting two hexagonal-like patterns for twin grains presented for the diffraction pattern of b).

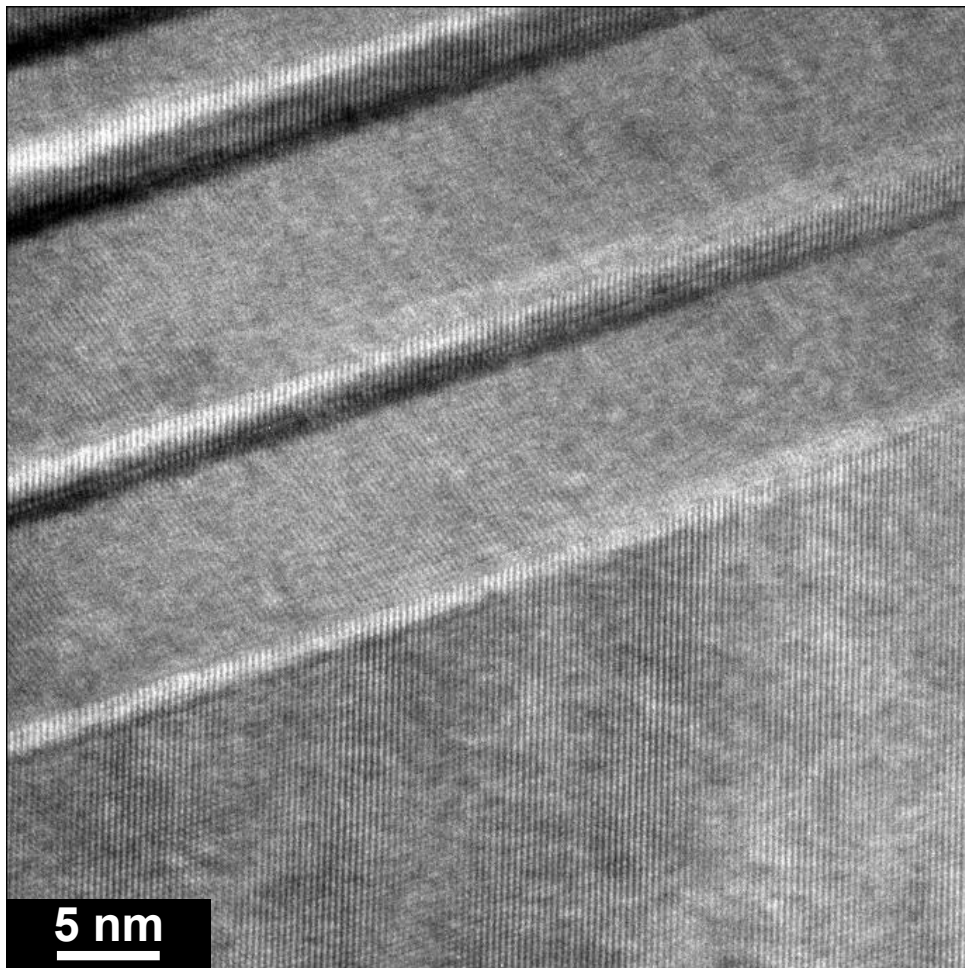


Figure 4.43: High resolution TEM image of an SiGe area with twin grain boundaries of sample BL:A1700nm annealed at 873 K for 1 h.

Al_xO_y and the formation of twin grain boundaries in SiGe appears possible.

4.3.3 Estimation of SiGe thickness increase

The reduction of SiO_2 by Al leads to the release of Si atoms which are incorporated into the SiGe layer. This results in an increase of the SiGe layer thickness d_{SiGe} in dependence on the Al layer thickness d_{Al} . TEM investigations have revealed that the resulting layer systems are rather rough and exhibit varying SiGe thicknesses. This section will give an estimation for the SiGe layer thickness, where the lower limit should be the nominal SiGe thickness

$$d_{\min} = d_{\text{SiGe}}. \quad (4.1)$$

The upper limit d_{\max} for the SiGe layer thickness can be estimated via the chemical reduction formula



If all Al atoms n_{Al} participate in the reduction of SiO_2 , the released Si atoms n_{Si} would amount to

$$4n_{\text{Si}} = 3n_{\text{Al}}. \quad (4.3)$$

Assuming constant atomic density N_{Si} for Si and N_{Al} for Al, the number of atoms present in the layers can be related to its spatial dimensions with

$$4N_{\text{Si}}d_{\text{Si}}A = 3N_{\text{Al}}d_{\text{Al}}A \quad (4.4)$$

where d_{Si} is the thickness of the newly formed Si layer and A is the area of the layer. As the area is the same for both the Si and Al layer, A can be omitted. This leads to the following expression for the Si layer thickness

$$d_{\text{Si}} = d_{\text{Al}} \frac{3N_{\text{Al}}}{4N_{\text{Si}}}. \quad (4.5)$$

Using the mass density ρ_d , molar mass M_{mol} , and Avogadro constant N_A for the relation

$$N = \frac{\rho_d N_A}{M_{\text{mol}}} \quad (4.6)$$

and the values of table 3.1, leads to

$$\begin{aligned} N_{\text{Si}} &= 5.00 \cdot 10^{22} \text{ atoms/cm}^3, \\ N_{\text{Al}} &= 6.05 \cdot 10^{22} \text{ atoms/cm}^3. \end{aligned}$$

The thickness of the formed Si layer can thus be estimated as

$$d_{\text{Si}} \approx 0.908 \cdot d_{\text{Al}}. \quad (4.7)$$

The upper limit d_{\max} for the SiGe thickness is presumed as the sum of the formed Si layer and the previously present SiGe thickness

$$d_{\max} = 0.908d_{\text{Al}} + d_{\text{SiGe}}. \quad (4.8)$$

This upper limit cannot be reached, since not every Al atom is available for the reduction process. Parts of the Al get incorporated into the SiGe acting as dopant atoms while other Al parts could also remain as inactive clusters in between the SiGe. The estimated range for the SiGe layer thickness fits to the SiGe thickness observed in the TEM images of fig. 4.38b) and fig. 4.40b). Since the layer thickness needs to be known for calculation of the charge carrier density n eq. (3.16) and the electrical resistivity ρ eq. (3.10), the effective layer thickness of the SiGe after annealing is assumed as

$$d_{\text{SiGe,eff}} = (d_{\min} + d_{\max})/2 = d_{\text{SiGe}} + \frac{0.908}{2}d_{\text{Al}} \quad (4.9)$$

with the uncertainty for this estimation being

$$\Delta d = d_{\max} - d_{\text{SiGe,eff}} = d_{\text{SiGe,eff}} - d_{\min} = \frac{0.908}{2}d_{\text{Al}}. \quad (4.10)$$

4.3.4 Thermoelectric Properties

The electrical resistivity and Seebeck coefficients were measured for all BL and TL samples in the as-deposited state. Only few of the TL samples could be measured with respect to their Seebeck coefficient as the amorphous, insulating 100 nm SiGe top layer made it hard to form stable contacts. The calculation of the electrical resistivity was carried out using the nominal Al thickness in the as-deposited state. For all samples, the resistivity was in the range of $0.8 \cdot 10^{-7} \Omega\text{m}$ to $1.3 \cdot 10^{-7} \Omega\text{m}$ while the Seebeck coefficient ranged from $5 \mu\text{V/K}$ to $8 \mu\text{V/K}$. The resistivity is about 4 times higher than of pure aluminum ($\rho_{\text{Al,RT}} = 2.687 \cdot 10^{-8} \Omega\text{m}$ [116]), which is likely due to crystal defects and grain boundaries affecting the electrical transport. The Seebeck coefficient is in the typical one digit $\mu\text{V/K}$ -regime for metals like Al.

All BL and TL samples were annealed at 873 K for 1 h so that the temperature was high enough to facilitate both, the MIC process and SiO_2 reduction. This is highlighted in fig. 4.44. Both the room temperature electrical resistivity and Seebeck coefficient of sample TL:Al200nm stay at low values of roughly $10^{-7} \Omega\text{m}$ and $5 \mu\text{V/K}$, respectively, after annealing at temperatures $T_{\text{ann}} \leq 773 \text{ K}$ for 1 h. After being annealed at $T_{\text{ann}} = 823 \text{ K}$ for 1 h, the room temperature resistivity has already increased by one order of magnitude while the Seebeck coefficient only increased to $8 \mu\text{V/K}$. This indicates that the reduction of SiO_2 by Al has already started at this temperature, but not all Al has completely reacted in 1 h. Annealing at $T_{\text{ann}} = 873 \text{ K}$ for 1 h leads to another increase in room temperature resistivity by two orders of magnitude, which is accompanied by an increase in Seebeck coefficient to $180 \mu\text{V/K}$. These values

are comparable to samples deposited on LTCC presented in section 4.2.3, for which the ratio $d_{\text{Al}}/d_{\text{SiGe}}$ was kept low enough to not have any continuous Al films after annealing. The annealing temperature was not increased any further as the quartz glass substrate started to soften for higher temperatures. An increase in annealing time led to no further change in transport properties, thus annealing at 873 K for 1 h can be assumed as sufficient to completely react any excess of Al. A sequential annealing process, which started at 563 K for 89 h to only induce the MIC process and afterwards reduce the SiO_2 at 873 K for 1 h, resulted in similar transport properties compared to the single step annealing.

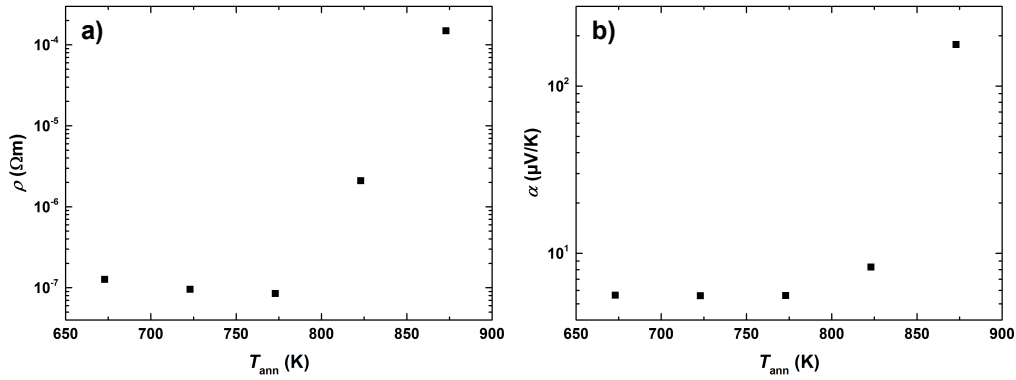


Figure 4.44: Dependence of the room temperature a) electrical resistivity and b) Seebeck coefficient on the annealing temperature T_{ann} of sample TL:Al200nm. The annealing time was kept constant at 1 h.

Electrical transport properties at room temperature in dependence on the Al layer thickness d_{Al} are summarized in fig. 4.45 for all samples after annealing at 873 K for 1 h. Samples TL:Al100nm and TL:Al125nm behaved as outliers and hence are not shown. Please keep in mind that the thickness used for calculating the charge carrier density and electrical resistivity is the previously discussed effective SiGe thickness presented in eq. (4.9).

The measured charge carrier density is shown in fig. 4.45a). All samples revealed positive charge carrier densities indicating successful p-type doping of the SiGe by the Al during the MIC process with charge carrier densities ranging from $2 \cdot 10^{19} \text{ cm}^{-3}$ to $2 \cdot 10^{20} \text{ cm}^{-3}$. Such charge carrier densities exceed the density of states of the valence band for pure Si of $N_{\text{V,Si}} = 2.65 \cdot 10^{19} \text{ cm}^{-3}$ (cf. table 2.1). As Ge has even a lower density of states in the valence band, the SiGe crystal can only have smaller N_{V} as for example $N_{\text{V,Si}_{80}\text{Ge}_{20}} = 9.52 \cdot 10^{18} \text{ cm}^{-3}$ was reported [122]. Therefore, all samples have to be assumed as degenerated semiconductors after annealing. The dependence of the charge carrier density on the Al thickness is qualitatively the same for BL and TL samples. Both samples series exhibit a minimum in charge carrier density around

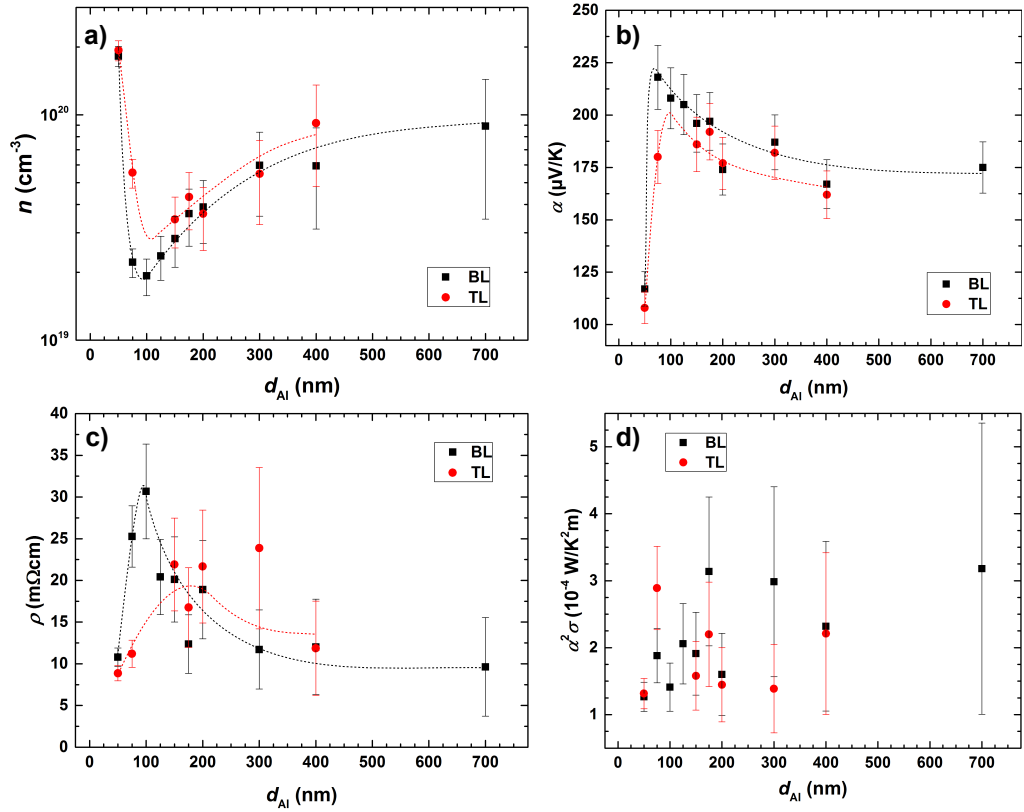


Figure 4.45: Dependence of the a) charge carrier density, b) Seebeck coefficient, b) electrical resistivity, and d) power factor on the initial Al thickness d_{Al} of the BL and TL samples annealed at 873 K for 1 h. Dashed lines are guides to the eye.

100 nm to 150 nm Al thickness.

The Seebeck coefficient for the annealed BL and TL samples is shown in fig. 4.45b). The uncertainty for the Seebeck measurement was estimated to be 7% based on spread of results among repetitive measurements. The lowest Seebeck coefficient of approximately $110 \mu\text{V}/\text{K}$ is obtained for both sample series at $d_{\text{Al}} = 50 \text{ nm}$. The Seebeck coefficient then rises to a maximum of $220 \mu\text{V}/\text{K}$ for the BL samples and then steadily decreases for thicker Al layers down to roughly $180 \mu\text{V}/\text{K}$. Because of the two missing outlier samples BL:Al100nm and BL:Al125nm, the maximum in Seebeck coefficient with respect to d_{Al} cannot be clearly determined for the TL samples. The Seebeck increases for $d_{\text{Al}} = 50 \text{ nm}$ to $180 \mu\text{V}/\text{K}$ and stays at nearly the same value of $187 \mu\text{V}/\text{K}$ for $d_{\text{Al}} = 150 \text{ nm}$. For the TL samples, the Seebeck coefficient saturates around $165 \mu\text{V}/\text{K}$ for high values of d_{Al} . The Seebeck coefficient for all annealed samples are in a typical range for degenerated semiconductors. The obtained Seebeck coefficients correlate well to the charge carrier densities as both indicate that no continuous Al layers are anymore present in annealed samples due to the reduction of SiO_2 by Al. Furthermore, the Seebeck coefficient follows the expected inverse dependency on the charge carrier density predicted by eq. (2.68). Except for $d_{\text{Al}} = 75 \text{ nm}$, both the charge carrier density and Seebeck coefficient reveal same values for samples with equal d_{Al} in the range of measurement uncertainty.

The electrical resistivity of the annealed BL and TL samples is shown in fig. 4.45c). The resistivity starts at $11 \text{ m}\Omega\text{cm}$ for $d_{\text{Al}} = 50 \text{ nm}$ and then increases to a maximum of $31 \text{ m}\Omega\text{cm}$ at $d_{\text{Al}} = 100 \text{ nm}$ for the TL samples. For higher d_{Al} , the resistivity decreases steadily again down to roughly $10 \text{ m}\Omega\text{cm}$. In case of the BL samples, the resistivity starts at $8 \text{ m}\Omega\text{cm}$ for $d_{\text{Al}} = 50 \text{ nm}$. The maximum in resistivity of $24 \text{ m}\Omega\text{cm}$ occurs at $d_{\text{Al}} = 300 \text{ nm}$. Possibly, this high resistivity value simply lies at the upper limit of measurement uncertainty, because the uncertainty bars for the resistivity of BL:Al300nm and TL:Al300nm overlap in a sensible intermediate range. For the high value of $d_{\text{Al}} = 400 \text{ nm}$, the resistivity likewise decreases for the BL sample down to $12 \text{ m}\Omega\text{cm}$. The qualitative temperature behavior of resistivity matches the one of the Seebeck coefficient and inversely also the one of the charge carrier density for the TL samples as expected. For the BL samples, the maximum is shifted too higher values of d_{Al} most likely due to sample outliers and measurement uncertainty.

The power factor calculated from the electrical resistivity and Seebeck coefficient is presented in fig. 4.45d). All obtained power factors are in the range from $1 \cdot 10^{-4} \text{ W}/\text{K}^2\text{m}$ to $3.5 \cdot 10^{-4} \text{ W}/\text{K}^2\text{m}$. Due to the large measurement uncertainties, especially for higher d_{Al} values, it is hardly possible to draw any systematic conclusions. At best, a slight tendency to increasing power factors with increasing d_{Al} could be supposed. Power factors for modern thermoelectric SiGe are typically up to one order of magnitude larger than the power factors presented here being in the order of $10^{-3} \text{ W}/\text{K}^2\text{m}$ [26]. This is mostly due to the relatively high electrical resistivity as the Seebeck coefficient reveals adequate values for the charge carrier densities present

in these samples. A possible explanation for this undesirable resistivity increase will be given in the next paragraph. Nevertheless, these results prove that the reduction of SiO₂ by Al can be utilized to remove excess of Al in a SiGe/Al system after being processed via MIC. No signs of metallic Al impairing the thermoelectric properties of the SiGe layers were detected up to ratios of $d_{\text{Al}}/d_{\text{SiGe}} \leq 3.5$. Additionally, BL and TL samples revealed the same transport properties for most samples highlighting that even Al not being in direct contact to the SiO₂ substrate in the as-deposited state could be reacted into insulating Al₂O₃.

Discussion on the temperature dependence of the electrical resistivity and Seebeck coefficient for samples annealed at 873 K for 1 h will be done exemplarily for samples TL:Al50nm, TL:Al150nm, and TL:Al400nm. Please note that the BL samples revealed the same temperature dependencies for the transport coefficients like TL samples [119]. The electrical resistivity of the three annealed samples is shown in fig. 4.46a) for the temperature range of 300 K to 700 K. The sample with the highest resistivity of roughly 20 mΩcm is TL:Al150nm. This correlates well to the measured charge carrier density of sample TL:Al150nm having the lowest charge carrier density of all TL samples. The other two samples have lower resistivity at around 10 mΩcm. Interestingly, the samples reveal different temperature dependencies. Sample TL:Al50nm has a resistivity of 12 mΩcm at 300 K, which then decreases with increasing temperature almost linearly down to 8 mΩcm at 700 K. The resistivity of TL:Al400nm instead starts with 9.5 mΩcm at 300 K and then increases linearly with temperature up to 11 mΩcm at 700 K. The sample TL:Al150nm with the intermediate Al thickness reveals decreasing resistivity up to temperatures of 380 K while for temperatures above 380 K the resistivity increases again. If these changes in resistivity are related to the excitation of additional free charge carriers, this would be detectable as a drop in Seebeck coefficient. The Seebeck coefficients of the respective samples are presented in fig. 4.46b). The Seebeck coefficients at 300 K are 135 μV/K, 180 μV/K, and 210 μV/K for samples TL:Al50nm, TL:Al150nm, and TL:Al400nm, respectively. An linear increase by 70 μV/K for all three samples up to the temperature of 700 K is obtained. This linear dependency is expected for degenerated semiconductors (compare eq. (2.68)) and indicates that no additional free charge carriers are thermally excited at elevated temperatures. The difference in resistivity behavior with temperature thus has to be governed by the charge carrier mobility μ .

To get a better insight on the underlying thermal excitation, Arrhenius plots for the electrical resistivity of samples TL:Al50nm and TL:Al150nm are shown in fig. 4.47a) and fig. 4.47b), respectively. Linear regions become apparent for the lower range of temperatures around 300 K. As the excitation of additional free charge carriers can be ruled out, this linear region can be attributed to energy barriers impairing the electrical transport [123]. A model for polycrystalline Si films was proposed by Seto [124]. Within this model, energy barriers are formed by trapping charge carriers in trap states along grain boundaries of the Si. The resulting energy barriers become

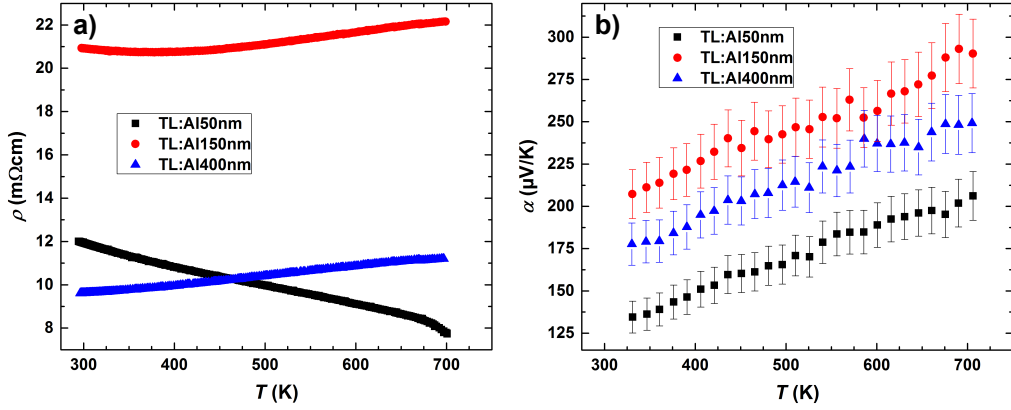


Figure 4.46: Dependence of the a) electrical resistivity and b) Seebeck coefficient on the temperature of samples TL:Al50nm, TL:Al150nm, and TL:Al400nm after being annealed at 873 K for 1 h.

maximal in height for the condition

$$L_{\text{gr}}N_{\text{imp}} = Q_{\text{t}} \quad (4.11)$$

with L_{gr} , N_{imp} , and Q_{t} being the grain size, density of singly charged ionized impurities, and area density of trapping states, respectively [124]. If $L_{\text{gr}}N_{\text{imp}} < Q_{\text{t}}$, the energy barriers are smaller due to not all trapping states being occupied as the crystallites are completely depleted with respect to their free charge carriers. For $L_{\text{gr}}N_{\text{imp}} > Q_{\text{t}}$, the energy barriers also decrease in height, because all trapping states are occupied and the width of the resulting dipole layer is shrunk by screening. Such effects have also been measured and the expected proportionality of

$$\rho \propto \frac{1}{\mu} \propto \exp(E_{\text{B}}/k_{\text{B}}T) \quad (4.12)$$

for the energy barrier height E_{B} was obtained [125]. The energy barrier height can thus be extracted from a linear fit to an Arrhenius plot of $\ln(\rho)$ over $1/T$ for degenerate semiconductors with a constant charge carrier density. The extracted energy barrier heights in dependence on the initial Al thickness for all annealed BL and TL samples are summarized in fig. 4.48. It becomes apparent that E_{B} decreases with increasing d_{Al} lying in the range from 1 meV to 13 meV. The obtained dependence of the charge carrier density on the initial Al thickness in fig. 4.46a) allows for the following interpretation. It was shown in fig. 4.37b) that the SiGe grain size $L_{\text{gr,SiGe}}$ of the annealed samples increases with d_{Al} . With respect to the model proposed by Seto and the condition for the maximal energy barrier height of eq. (4.11), it becomes apparent that this increase in grain size can lead to a decrease in barrier height E_{B} ,

if Q_t and N_{imp} are independent from the grain size. If $L_{\text{gr,SiGe}}$ becomes greater than Q_t/N_{imp} , effectively more charge carriers are able to participate in the electronic transport due to the lowered E_B . This could be attributed to the obtained increase in charge carrier density for increasing Al thickness for $d_{\text{Al}} > 100$ nm. The model of Seto cannot be used to explain the drop in charge carrier density for values up to $d_{\text{Al}} \leq 100$ nm as the measured energy barrier height continuously increases for decreasing d_{Al} .

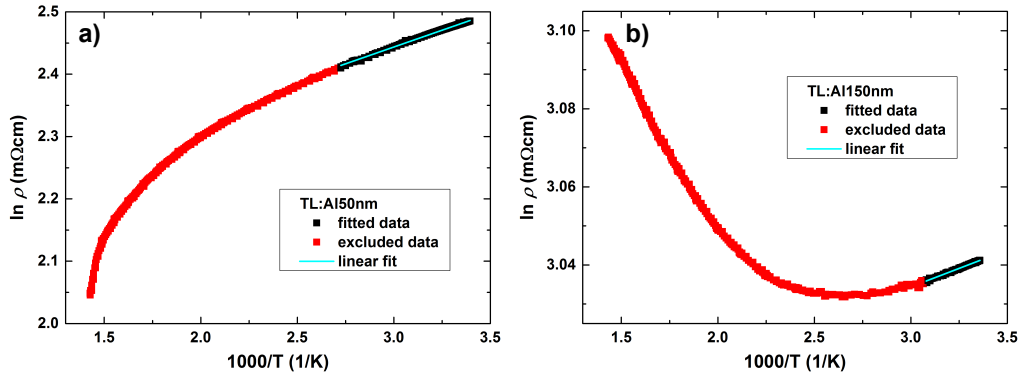


Figure 4.47: Arrhenius plot of $\ln(\rho)$ over $1/T$ highlighting the used data for a linear fit to estimate energy barrier height for samples a) TL:Al50nm and b) TL:Al150nm after being annealed at 873 K for 1 h.

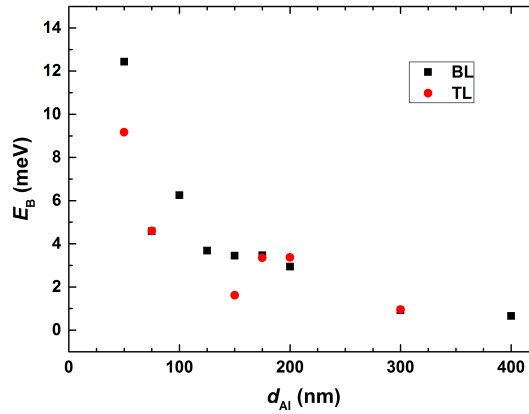


Figure 4.48: Energy barrier height in dependence on the initial Al thickness for the BL and TL samples after being annealed at 873 K for 1 h.

The occurrence of energy barriers also explains, why the electrical resistivity and Seebeck coefficient have different temperature dependencies discussed in the prior

chapter 4.2. If the ambient thermal energy is enough to fully excite all charge carriers over the energy barriers, the resistivity follows the typical linear proportionality to temperature of degenerated semiconductors (cf. eq. (2.62)), which can be seen in fig. 4.46a) for TL:Al150nm and TL:Al400nm. In case of energy barriers being too high, the ambient thermal energy is only sufficient to only excite parts of the charge carriers over energy barriers. This becomes apparent for sample TL:Al50nm in fig. 4.47a). Here, the energy barrier height was extracted from the temperature range of 300 K to 370 K. For higher temperatures, $\ln(\rho)$ over $1/T$ drops even faster than linear for this sample indicating even higher energy barriers being overcome by the increased thermal excitation. As no change to a positive temperature coefficient for the electrical resistivity could be observed at elevated temperatures, measurements at even higher temperatures would be valuable to see how far the resistivity decrease would continue.

5 Summary

The aim of this work was to prepare and to characterize thermoelectric $\text{Si}_{80}\text{Ge}_{20}$ thin films by utilizing the effect of MIC. The thin films were deposited by magnetron sputtering and the SiGe was amorphous in the as-deposited state. The process of MIC was utilized to induce crystallization of the SiGe during annealing at temperatures as low as 485 K. Aluminum was used as the catalytic metal for the MIC process. Three different kind of substrates in the form of thermally oxidized silicon, aluminum oxide based, and silicon oxide based substrates have been used. These substrates revealed a direct influence on the resulting thermoelectric properties after applied annealing. The first samples were deposited as multilayers with 50 repetitions of SiGe/Al bilayers on thermally oxidized silicon. The individual Al layer thickness d_{Al} was chosen in the range of 0.18 nm up to 1 nm while the SiGe layer thickness d_{SiGe} was kept constant at 10 nm for all samples of this series. The process of MIC could be verified for this sample series down to annealing temperatures as low as 673 K. The higher the Al thickness was chosen, the more the crystallization temperature of the SiGe could be reduced. The thinnest Al layer thickness still revealing reduced crystallization temperature due to MIC was 0.36 nm showing a crystallization temperature of 873 K. The microstructural characterization of the MIC processed SiGe thin films revealed polycrystalline, continuous SiGe layers with no traces left of the initial SiGe/Al multilayer heterostructure. Only a surface accumulation of Al which gets oxidized in ambient conditions could be detected besides the homogenous SiGe layer.

The transport properties of the as-deposited samples were insulator like due to discontinuous Al layers and the SiGe being amorphous. After the MIC process at annealing temperatures ranging from 673 K to 873 K, the samples exhibited semi-conducting transport properties at room temperature with electrical resistivity and Seebeck coefficient of around 50 m Ω cm to 100 m Ω cm and 80 μ V/K, respectively. This proved a successful MIC process accompanied by Al doping of the SiGe during the MIC process. At elevated temperatures higher than 500 K, a decrease for both the electrical resistivity and the Seebeck coefficient could be observed with the Seebeck coefficient even changing its sign. This could be attributed to intrinsic charge carrier excitation in the Si substrate. The Si substrate became electrically connected to the SiGe layer by reduction of the SiO_2 isolation layer via parts of the Al. At high enough temperatures, the intrinsic Si substrate became more electrically conducting than the SiGe thin film thus rendering the combination of a thermally oxidized Si substrate and a SiGe/Al system useless with respect to thermoelectric application at elevated temperatures.

The second series of samples retained principally the same SiGe/Al multilayer structure in the as-deposited state as the previous sample series. The substrate was changed to an electrically insulating, aluminum oxide based ceramic substrate to rule out any influence of the substrate on the thermoelectric active SiGe thin film like in case of the previous sample series. The MIC process could also be verified for these samples and matching results regarding the microstructure and crystallization temperature of the SiGe were obtained. The ceramic substrates exhibited huge surface roughness in the range of microns. This resulted in deep trenches along the thin film which was locally discontinuous. The transport properties revealed no signs of the MIC processes SiGe thin films being separated and an electrically continuous SiGe layer was always observed after the MIC process. An increase in SiGe crystallinity and grain size matching a decrease in electrical resistivity was obtained for increasing Al layer thickness up to 1 nm. As the Seebeck coefficient stayed constant despite decreasing resistivity, the sample series was extended to even thicker individual Al layers up to 10 nm to cover the range of $0.1 \leq d_{\text{Al}}/d_{\text{SiGe}} \leq 1$ and see how far this improvement in thermoelectric properties could be continued.

An increase of the ratio $d_{\text{Al}}/d_{\text{SiGe}}$ leads to an improved MIC process up to a ratio of $d_{\text{Al}}/d_{\text{SiGe}} = 1$. However, if too much Al is present, it is not possible to redistribute the Al during the diffusion driven MIC process without forming continuous Al layers and thus short circuiting the thermoelectric SiGe thin film. The switching point from semiconducting to metallic transport behavior after MIC in SiGe/Al systems was found to be around $d_{\text{Al}}/d_{\text{SiGe}} = 0.25$ and was coinciding with transport properties values indicating continuous Al layers in the as-deposited state. Furthermore, in-situ measurements of electrical resistivity and Seebeck coefficient were conducted during the MIC process for samples without Al short circuits being present after the MIC process. It could be shown that for increasing temperatures, a thinning out of the Al layers in form of a resistance increase can be observed at the beginning of the MIC process. When the Al layers are not continuous anymore, a sudden change in Seebeck coefficient from metallic-like to semiconducting is observed. Following, a decrease in resistance is observed as the remaining amorphous SiGe parts are crystallized. The best obtained room temperature values for electrical resistivity, Seebeck coefficient, and thermal conductivity of this sample series were $10 \text{ m}\Omega\text{cm}$, $150 \text{ }\mu\text{V/K}$, $2.7 \text{ Wm}^{-1}\text{K}^{-1}$, respectively.

Temperature-dependent XRD studies revealed a two-step process for the MIC of the SiGe. Both onset temperatures for the MIC process exhibited a strong dependence on the Al thickness with lower crystallization temperatures being achieved for increasing Al layer thickness. The lowest obtained onset temperatures were 485 K and 725 K, respectively. Samples with high enough Al content revealed a phase separation into a silicon- and germanium-rich SiGe alloy. Such phase separations are promising for future thermoelectric research by potentially decreasing the thermal conductivity.

The problem of remaining Al short circuiting the thermoelectric SiGe thin film after

MIC was solved via the reduction of SiO_2 and Al to Si and Al_2O_3 . Samples were deposited onto quartz glass to enable this chemical reaction. It could be shown that the reduction started at around 823 K and a complete reaction of the Al could be achieved when annealing at 873 K for 1 h. The released Si atoms did not form a separate phase, but were incorporated into the SiGe resulting in an increase of the SiGe thickness and a shift of the composition to being more Si-rich. TEM analysis revealed areas of high twin grain boundary density in the crystallized SiGe layer. Such structures could be beneficial for increasing the thermoelectric efficiency by hindering phonon movement while not impairing the electron transport.

The presence of energy barriers influencing electron transport could be detected after MIC of the SiGe. Electrical resistivity measurements revealed a decreasing height of the energy barriers with increasing Al content of the starting SiGe/Al system. If the energy barriers were overcome by thermal excitation, then the typical temperature dependence of degenerately doped SiGe was observed in form of increasing electrical resistivity and Seebeck coefficient with temperature. Obtained values ranged from 10 m Ω cm and 130 μ V/K at room temperature to 8 m Ω cm and 290 μ V/K at 700 K, respectively.

This work showed that the preparation of thermoelectric SiGe thin films via the process of MIC is possible. Interesting aspects like phase separation, twin grain boundaries, and energy barriers in the resulting SiGe layers prove the high potential for further thermoelectric research with respect to the MIC phenomena.

Bibliography

- [1] Key World Energy Statistics 2016. *International Energy Agency (IEA)*, page 28, 2016.
- [2] World Energy Outlook 2016. *International Energy Agency (IEA)*, 2016.
- [3] E. Cook. The Flow of Energy in an Industrial Society. *Scientific American*, 225(3):134–144, 1971.
- [4] L. Francioso, C. De Pascali, I. Farella, C. Martucci, P. Cretì, P. Siciliano, and A. Perrone. Flexible thermoelectric generator for ambient assisted living wearable biometric sensors. *J. Power Sources*, 196(6):3239–3243, 2011.
- [5] H. J. Goldsmid. Principles of thermoelectric devices. *British Journal of Applied Physics*, 11(6):209, 1960.
- [6] W. Thomson. On a mechanical theory of thermoelectric currents. *Proc. Roy. Soc. Edinburgh*, 3:91–98, 1857.
- [7] G. S. Nolas, J. Sharp, and H. J. Goldsmid. *Thermoelectric-Basic Principles and New Material Developments*. Springer, 2001.
- [8] A. F. Ioffe. *Semiconductor Thermoelements and Thermoelectric Cooling*. London: Infosearch, 1957.
- [9] M. V. Vedernikov and E. K. Iordanishvili. A. F. Ioffe and origin of modern semiconductor thermoelectric energy conversion. *17th Int. Conf. on Thermoelectrics*, 1:37–42, 1998.
- [10] O. Saka and S. Sato, N. Uchida. Development of Unmanned Magnetometer Stations for Use in Antarctica. *Antarctic Science*, 2(4):355–361, 1990.
- [11] S. Riffat and X. Ma. Thermoelectrics: A Review of Present and Potential Applications. *Applied Thermal Engineering*, 23(8):913–935, 2003.
- [12] C. B. Vining. The thermoelectric limit $ZT \sim 1$: fact or artifact. *Proceedings of the XI international conference on thermoelectrics*, pages 223–231, 1992.
- [13] D. M. Rowe. Applications of nuclear-powered thermoelectric generators in space. *Applied Energy*, 40:241–271, 1991.

- [14] B. Poudel, Q. Hao, Y. Ma, Y. Lan, A. Minnich, B. Yu, D. Yan, X. Wang, A. Muto, D. Vashaee, X. Chen, J. Liu, M. S. Dresselhaus, G. Chen, and Z. Ren. High-Thermoelectric Performance of Nanostructured Bismuth Antimony Telluride Bulk Alloys. *Science*, 320:634–638, 2008.
- [15] O. Yamashita, S. Tomiyoshi, and K. Makita. Bismuth telluride compounds with high thermoelectric figures of merit. *J. Appl. Phys.*, 93(1):368–374, 2003.
- [16] A. Saramat, G. Svensson, A. E. C. Palmqvist, C. Stiewe, E. Mueller, D. Platzek, S. G. K. Williams, D. M. Rowe, J. D. Bryan, and G. D. Stucky. Large thermoelectric figure of merit at high temperature in Czochralski-grown clathrate $\text{Ba}_8\text{Ga}_{16}\text{Ge}_{30}$. *J. Appl. Phys.*, 99:023708, 2006.
- [17] X. Shi, J. Yang, S. Bai, J. Yang, H. Wang, M. Chi, J. R. Salvador, W. Zhang, L. Chen, and W. Wong-Ng. On the Design of High-Efficiency Thermoelectric Clathrates through a Systematic Cross-Substitution of Framework Elements. *Adv. Funct. Mater.*, 20:755–763, 2010.
- [18] G. S. Nolas, D. T. Morelli, and T. M. Tritt. SKUTTERUDITES: A Phonon-Glass-Electron Crystal Approach to Advanced Thermoelectric Energy Conversion Applications. *Annu. Rev. Mater. Sci.*, 29:89–116, 1999.
- [19] X. Shi, J. Yang, J. R. Salvador, M. Chi, J. Y. Cho, H. Wang, S. Bai, J. Yang, W. Zhang, and L. Chen. Multiple-Filled Skutterudites: High Thermoelectric Figure of Merit through Separately Optimizing Electrical and Thermal Transports. *J. Am. Chem. Soc.*, 133:7837–7846, 2011.
- [20] C. Yu, T.-J. Zhu, R.-Z. Shi, Y. Zhang, X.-B. Zhao, and J. He. High-performance half-Heusler thermoelectric materials $\text{Hf}_{1-x}\text{Zr}_x\text{NiSn}_{1-y}\text{Sb}_y$ prepared by levitation melting and spark plasma sintering. *Acta Materialia*, 57:2757–2764, 2009.
- [21] G. Joshi, X. Yan, H. Wang, W. Liu, G. Chen, and Z. Ren. Enhancement in Thermoelectric Figure-Of-Merit of an N-Type Half-Heusler Compound by the Nanocomposite Approach. *Adv. Energy Mater.*, 1:643–647, 2011.
- [22] N. Mingo, D. Hauser, N. P. Kobayashi, M. Plissonnier, and A. Shakouri. ”Nanoparticle-in-Alloy” Approach to Efficient Thermoelectrics: Silicides in SiGe. *Nano Lett.*, 9(2):711–715, 2009.
- [23] A. J. Minnich, M. S. Dresselhaus, Z. F. Ren, and G. Chen. Bulk nanostructured thermoelectric materials: current research and future prospects. *Energy Environ. Sci.*, 2:466–479, 2009.
- [24] M. S. Dresselhaus and M. Y. Chen, G. and Tang. New Directions for Low-Dimensional Thermoelectric Materials. *Adv. Mater.*, 19:1043–1053, 2007.

-
- [25] Q. Zhang, Y. Sun, W. Xu, and D. Zhu. Organic Thermoelectric Materials: Emerging Green Energy Materials Converting Heat to Electricity Directly and Efficiently. *Adv. Mater.*, 26:6829–6851, 2014.
- [26] Y. Lan, A. J. Minnich, G. Chen, and Z. Ren. Enhancement of Thermoelectric Figure-of-Merit by a Bulk Nanostructuring Approach. *Adv. Funct. Mater.*, 20:357–376, 2010.
- [27] W. L. Liu, T. Borca-Tasciuc, G. Chen, J. L. Liu, and K. L. Wang. Anisotropic Thermal Conductivity of Ge Quantum-Dot and Symmetrically Strained Si/Ge Superlattices. *Journal of Nanoscience and Nanotechnology*, 4:39–42, 2001.
- [28] M. Zebarjadi, G. Joshi, G. Zhu, B. Yu, A. Minnich, Y. Lan, X. Wang, M. Dresselhaus, Z. Ren, and G. Chen. Power Factor Enhancement by Modulation Doping in Bulk Nanocomposites. *Nano Lett.*, 11(6):2225–2230, 2011.
- [29] L. P. H. Jeurgens, Z. Wang, and E. J. Mittemeijer. Thermodynamics of reactions and phase transformations at interfaces and surfaces. *Int. J. Mat. Res.*, 100:1281–1307, 2009.
- [30] W. H. Lucke. A Brief Survey of Elementary Thermoelectric Theory. Technical report, Energy Conversion Branch Electronics Division - U.S. NAVAL RESEARCH LABORATORY Washington, D.C., 1963.
- [31] C. Goupil, W. Seifert, K. Zabrocki, E. Müller, and G. J. Snyder. Thermodynamics of Thermoelectric Phenomena and Applications. *Entropy*, 13:1481–1517, 2011.
- [32] L. Onsager. Reciprocal Relations in Irreversible Processes. I. *Phys. Rev.*, 37:405–426, 1931.
- [33] D. Nemir and J. Beck. On the Significance of the Thermoelectric Figure of Merit Z . *Journal of Electronic Materials*, 39(9):1897–1901, 2010.
- [34] S. M. Sze and K. Ng Kwok. *Physics of Semiconductor Devices*. John Wiley & Sons, Inc., Hoboken, New Jersey, 3rd edition, 2007.
- [35] E. Conwell and V. F. Weisskopf. Theory of impurity scattering in semiconductors. *Phys. Rev.*, 77:388, 1950.
- [36] J. Bardeen and W. Shockley. Deformation Potentials and Mobilities in Nonpolar Crystals. *Phys. Rev.*, 80:72, 1950.
- [37] H. Ibach and H. Lüth. *Festkörperphysik: Einführung in die Grundlagen*. Springer, Berlin, Heidelberg, 7th edition, 2009.

- [38] N. W. Ashcroft and N. D. Mermin. *Solid State Physics*. Holt-Saunders, Philadelphia, Pennsylvania, Holt-Saunders International edition, 1976.
- [39] M. Jonson and G. D. Mahan. Mott's formula for the thermopower and the Wiedemann-Franz law. *Phys. Rev. B*, 21:4223–4229, 1979.
- [40] I. Pallecchi, G. Lamura, M. Tropeano, M. Putti, R. Viennois, E. Giannini, and D. Van der Marel. Seebeck effect in $\text{Fe}_{1+x}\text{Te}_{1-y}\text{Se}_y$ single crystals. *Phys. Rev. B*, 80:214511, 2009.
- [41] Q. Zhu, E. M. Hopper, B. J. Ingram, and T. O. Mason. Combined Jonker and Ioffe analysis of oxide conductors and semiconductors. *Journal of the American Ceramic Society*, 94:187–193, 2011.
- [42] G. J. Snyder and E. S. Toberer. Complex thermoelectric materials. *Nature Materials*, 7:105–114, 2008.
- [43] N. Stein, N. Petermann, R. Theissmann, G. Schierning, R. Schmechel, and H. Wiggers. Artificially nanostructured n-type SiGe bulk thermoelectrics through plasma enhanced growth of alloy nanoparticles from the gas phase. *J. Mater. Res.*, 26(15):1872–1878, 2011.
- [44] T. C. Harman, P. J. Taylor, M. P. Walsh, and B. E. LaForge. Quantum Dot Superlattice Thermoelectric Materials and Devices. *Science*, 297:2229–2232, 2002.
- [45] L. D. Hicks and M. S. Dresselhaus. Effect of quantum-well structures on the thermoelectric figure of merit. *Phys. Rev. B*, 47:12727, 1993.
- [46] M. V. Daniel, L. Hammerschmidt, C. Schmidt, F. Timmermann, J. Franke, N. Jöhrmann, M. Hietschold, D. C. Johnson, B. Paulus, and M. Albrecht. Structural and thermoelectric properties of FeSb_3 skutterudite thin films. *Phys. Rev. B*, 91:085410, 2015.
- [47] E. S. Landry, M. I. Hussein, and A. J. H. McGaughey. Complex superlattice unit cell designs for reduced thermal conductivity. *Phys. Rev. B*, 77:184302, 2008.
- [48] C. He, M. Daniel, M. Grossmann, O. Ristow, D. Brick, M. Schubert, M. Albrecht, and T. Dekorsy. Dynamics of coherent acoustic phonons in thin films of CoSb_3 and partially filled $\text{Yb}_x\text{Co}_4\text{Sb}_{12}$ skutterudites. *Phys. Rev. B*, 89:174303, 2014.
- [49] Z. Xionga, X. Chena, X. Huang, S. Baia, and L. Chen. High thermoelectric performance of $\text{Yb}_{0.26}\text{Co}_4\text{Sb}_{12}/\text{yGaSb}$ nanocomposites originating from scattering electrons of low energy. *Acta Materialia*, 58:3995–4002, 2010.

-
- [50] C. B. Vining, W. Laskow, J. O. Hanson, R. R. Van der Beck, and P. D. Gorsuch. Thermoelectric properties of pressure-sintered $\text{Si}_{0.8}\text{Ge}_{0.2}$ thermoelectric alloys. *J. Appl. Phys.*, 69(8):4333–4340, 1991.
- [51] M. G. Kanatzidis. Nanostructured Thermoelectrics: The New Paradigm? *Chem. Mater.*, 22:648–659, 2010.
- [52] C. B. Vining. *CRC Handbook of Thermoelectrics*. Boca Raton, Florida, 1995.
- [53] J. Garg, N. Bonini, B. Kozinsky, and N. Marzari. Role of disorder and anharmonicity in the thermal conductivity of silicon-germanium alloys: A first-principles study. *Phys. Rev. Lett.*, 106:045901, 2011.
- [54] C. M. Bhandari and D. M. Rowe. Silicon-germanium alloys as high-temperature thermoelectric materials. *Contemp. Phys.*, 21(3):219–242, 1980.
- [55] Ioffe Physico-Technical Institute. Electronic Archive: New Semiconductor Materials. Characteristics and Properties, 2001.
- [56] L. Vegard. Die Konstitution der Mischkristalle und die Raumfüllung der Atome. *Zeitschrift für Physik A Hadrons and Nuclei*, 5(5):1726, 1921.
- [57] J. P. Dismukes, L. Ekstrom, E. F. Steigmeier, I. Kudman, and D. S. Beers. Thermal and electrical properties of heavily doped Ge-Si alloys up to 1300K. *J. Appl. Phys.*, 35(10):2899–2907, 1964.
- [58] J. Martin, W. Wong-Ng, I. Caillat, T. and Yonenaga, and M. L. Green. Thermocyclic stability of candidate Seebeck coefficient standard reference materials at high temperature. *J. Appl. Phys.*, 115:193501, 2014.
- [59] G. H. Zhu, H. Lee, Y. C. Lan, X. W. Wang, G. Joshi, D. Z. Wang, J. Yang, D. Vashaee, H. Guilbert, A. Pillitteri, M. S. Dresselhaus, G. Chen, and Z. F. Ren. Increased Phonon Scattering by Nanograins and Point Defects in Nanostructured Silicon with a Low Concentration of Germanium. *Phys. Rev. Lett.*, 102:196803, 2009.
- [60] B. Yu, M. Zebarjadi, H. Wang, K. Lukas, H. Wang, D. Wang, C. Opeil, M. Dresselhaus, G. Chen, and Z. Ren. Enhancement of Thermoelectric Properties by Modulation-Doping in Silicon Germanium Alloy Nanocomposites. *Nano Lett.*, 12(4):2077–2082, 2012.
- [61] Y. Wu, R. Fan, and P. Yang. Block-by-Block Growth of Single-Crystalline Si/SiGe Superlattice Nanowires. *Nano Lett.*, 2(2):83–86, 2002.

- [62] E. K. Lee, L. Yin, Y. Lee, J. W. Lee, S. J. Lee, J. Lee, S. N. Cha, D. Whang, G. S. Hwang, K. Hippalgaonkar, A. Majumdar, C. Yu, B. L. Choi, J. M. Kim, and K. Kim. Large Thermoelectric Figure-of-Merits from SiGe Nanowires by Simultaneously Measuring Electrical and Thermal Transport Properties. *Nano Lett.*, 12(6):2918–2923, 2012.
- [63] D. Grützmacher, T. Fromherz, C. Dais, J. Stangl, E. Müller, Y. Ekinici, H. H. Solak, H. Sigg, R. T. Lechner, E. Wintersberger, S. Birner, V. Holý, and G. Bauer. Three-Dimensional Si/Ge Quantum Dot Crystals. *Nano Lett.*, 7(10):3150–3156, 2007.
- [64] K. Brunner. Si/Ge nanostructures. *Reg. Prog. Phys.*, 65:27–72, 2002.
- [65] R. Lechner, M. Buschbeck, M. Gjukic, and M. Stutzmann. Thin polycrystalline SiGe films by aluminium-induced layer exchange. *physc stat. sol. (c)*, 1(5):1131–1143, 2004.
- [66] J. P. Fleurial and A. Borshchevsky. Si-Ge-metal ternary phase diagram calculations. *Journal of the Electrochemical Society*, 137(9):2928–2937, 1990.
- [67] A. E. Gershinskii, A. A. Khoromenko, and F. L. Edelman. Reduction of thermally grown SiO₂ by Al films. *Physica Status Solidi (a)*, 25(2):645–651, 1974.
- [68] F. Oki, Y. Ogawa, and Y. Fujiki. Effect of deposited metals on crystallization temperature of amorphous germanium film. *Japanese Journal of Applied Physics*, 8:1056, 1969.
- [69] J. R. Bosnell and U. C. Voisey. The influence of contact materials on the conduction crystallization temperature and electrical properties of amorphous germanium, silicon and boron films. *Thin Solid Films*, 6:161–166, 1970.
- [70] Z. Wang, L. P. H. Jeurgens, and E. J. Mittemeijer. *Meta-Induced Crystallization: Fundamentals and Applications*. Pan Stanford Publishing Pte. Ltd., Singapore, 2015.
- [71] O. Nast and S. R. Wenham. Elucidation of the layer exchange mechanism in the formation of polycrystalline silicon by aluminum-induced crystallization. *J. Appl. Phys.*, 88(1):124–132, 2000.
- [72] M. Wong, Z. Jin, G. A. Bhat, P. C. Wong, and H. S. Kwok. Characterization of the MIC/MILC Interface and Its Effects on the Performance of MILC Thin-Film Transistors. *IEEE Transactions on Electronic Devices*, 47(5):1061–1067, 2000.

-
- [73] W. Knaepen, C. Detavernier, R. L. Van Meirhaeghe, J. Jordan Sweet, and C. Lavoie. In-situ X-ray Diffraction study of Metal Induced Crystallization of amorphous silicon. *Thin Solid Films*, 516:4946–4952, 2008.
- [74] W. Knaepen, S. Gaudet, C. Detavernier, R. L. Van Meirhaeghe, J. Jordan Sweet, and C. Lavoie. In situ x-ray diffraction study of metal induced crystallization of amorphous germanium. *J. Appl. Phys.*, 105:083532, 2009.
- [75] C. A. Niedermeier, Z. Wang, and E. J. Mittemeijer. Al-induced crystallization of amorphous $\text{Si}_x\text{Ge}_{1-x}$ ($0 \leq x \leq 1$): Diffusion, phase development and layer exchange. *Acta Materialia*, 72:211–222, 2014.
- [76] S. Peng, X. Shen, Z. Tang, and D. He. Low-temperature Al-induced crystallization of hydrogenated amorphous $\text{Si}_{1-x}\text{Ge}_x$ ($0.2 \leq x \leq 1$) thin films. *Thin Solid Films*, 516:2276–2279, 2008.
- [77] T. L. Cottrell. *The Strength of Chemical Bonds*. Butterworths Publications, London, 1958.
- [78] T. J. Konno and R. Sincalir. Metal-contact-induced crystallization of semiconductors. *Materials and Science Engineering: A*, 179:426–432, 1994.
- [79] A. Hiraki. Low temperature reactions at Si/metal interfaces: what is going on at the interfaces? *Surface Science Reports*, 3:357–412, 1983.
- [80] Z. M. Wang, J. Y. Wang, L. P. H. Jeurgens, and E. J. Mittemeijer. Tailoring the Ultrathin Al-Induced Crystallization Temperature of Amorphous Si by Application of Interface Thermodynamics. *Phys. Rev. Lett.*, 100:125503, 2008.
- [81] Z. M. Wang, L. Gu, F. Phillipp, J. Y. Wang, L. P. H. Jeurgens, and E. J. Mittemeijer. Metal-catalyzed growth of semiconductor nanostructures with solubility and diffusivity constraints. *Advanced Materials*, 23:845–859, 2011.
- [82] R. A. Haefer. *Werkstoff-Forschung und Technik*, volume 5. Springer, Berlin, 1987.
- [83] W. Husinsky and G. Betz. Fundamental aspects of SNMS for thin film characterization: experimental studies and computer simulations. *Thin Solid Films*, 272:289–309, 1996.
- [84] M. Senoner and W. E. S. Unger. SIMS imaging of the nanoworld: applications in science and technology. *J. Anal. Spectrom.*, 27:1050–1068, 2012.
- [85] L. C. Feldman and J. M. Poate. Rutherford Backscattering and Channeling Analysis of Interfaces and Epitaxial Structures. *Ann. Rev. Mater. Sci.*, 12:149–176, 1982.

- [86] W. D. Callister and D. G. Rethwisch. *Materialwissenschaften und Werkstofftechnik: Eine Einführung*. Wiley-VCH, Weinheim, 1st edition, 2012.
- [87] M. Mayer. *SIMNRA User's Guide 6.05*. Max-Planck-Institut für Plasmaphysik, Garching, Germany, 2009.
- [88] U. Welzel, J. Ligot, P. Lamparter, A. C. Vermeulen, and E. J. Mittemeijer. Stress analysis of polycrystalline thin films and surface regions by X-ray diffraction. *J. Appl. Cryst.*, 38:1–29, 2005.
- [89] P. Scherrer. Bestimmung der Größe und der inneren Struktur von Kolloidteilchen mittels Röntgenstrahlen. *Nachrichten von der Gesellschaft der Wissenschaften zu Göttingen*, 1918:98–100, 1918.
- [90] International Centre for Diffraction Data. Powder Diffraction File, version 1.30, 1997.
- [91] C. Michaelsen, P. Ricardo, D. Anders, M. Schuster, J. Schilling, and H. Göbel. Improved graded multilayer mirrors for XRD applications. *Advances in X-ray Analysis*, 42:308–320, 2000.
- [92] P. J. Goodhew, J. Humphreys, and R. Beanland. *Electron Microscopy and Analysis*. Taylor & Francis, London / New York, 3rd edition, 2001.
- [93] K. D. Vernon-Parry. Scanning Electron Microscopy: an introduction. *Analysis*, 13(4):40–44, 2000.
- [94] L. Reimer and H. Kohl. *Transmission Electron Microscopy: Physics of Image Formation*. Springer, New York, 5th edition, 2008.
- [95] D. B. Williams and C. B. Carter. *Transmission Electron Microscopy: A Textbook for Material Science*. Springer, New York, 2009.
- [96] L. J. van der Pauw. A method of measuring the resistivity and hall coefficient on lamellae of arbitrary shape. *Philips Technical Review*, 20:220, 1958/59.
- [97] J. Franke. Aufbau und Erprobung eines Messsystems zur Messung elektrischer Transportkoeffizienten bei hohen Temperaturen, Bachelor thesis, Technische Universität Chemnitz, Chemnitz, 2011.
- [98] J. Franke. Charakterisierung von CoSb₃-schichten bei hohen Temperaturen, Master Thesis, Technische Universität Chemnitz, Chemnitz, 2013.
- [99] E. H. Hall. On a new action of the magnet on electric currents. *American Journal of Mathematics*, 2(3), 287 1879.

-
- [100] J. de Boor and E. Müller. Data analysis for Seebeck coefficient measurements. *Review of Scientific Instruments*, 84:065102, 2013.
- [101] J. Martin, T. Tritt, and Uher; C. High temperature Seebeck coefficient metrology. *J. Appl. Phys.*, 108:121101, 2010.
- [102] S.-M. Lee and D. G. Cahill. Heat transport in thin dielectric films. *J. Appl. Phys.*, 81(6):2590–2595, 1997.
- [103] D. G. Cahill, M. Katiyar, and J. R. Abelson. Thermal conductivity of a-Si:H thin films. *Phys. Rev. B*, 50(9):6077–6081, 1994.
- [104] M. Lindorf, H. Rohrmann, G. L. Katona, D. L. Beke, H.-F. Pernau, and M. Albrecht. Nanostructured SiGe thin films obtained through MIC processing. *Materials Today: Proceedings*, 2:557–565, 2015.
- [105] T. J. Konno and R Sinclair. Crystallization of silicon in aluminium/amorphous-silicon multilayers. *Philosophical Magazine Part B*, 66(6):749–765, 1992.
- [106] A. Barrie. X-ray photoelectron spectra of aluminium and oxidised aluminium. *Chemical Physics Letters*, 19(1):109–113, 1973.
- [107] E. V. Jelenkovic and K. Y. Tong. Effect of SiGe thickness on crystallisation and electrical properties of sputtered silicon film in Si/SiGe/insulator structure. *Appl. Surf. Sci.*, 135:143–149, 1998.
- [108] W. K. Choi, L. K. Teh, L. K. Bera, and W. K. Chim. Microstructural characterization of rf sputtered polycrystalline silicon germanium films. *J. Appl. Phys.*, 91(1):444–450, 2002.
- [109] M. Podgorny, G. Wolfgarten, and J. Pollmann. The band structure of $\text{Si}_x\text{Ge}_{1-x}$ alloys: the self-consistent virtual-crystal approximation. *J. Phys. C: Solid State Physics*, 19:L141–L146, 1986.
- [110] M. A. Green. Intrinsic concentration, effective densities of states, and effective mass in silicon. *J. Appl. Phys.*, 67(7):2944–2954, 1990.
- [111] J. H. Kim and J. Y. Lee. Al-Induced Crystallization of an Amorphous Si Thin Film in a Polycrystalline Al/Native SiO_2 /Amorphous Si Structure. *Jpn. J. Appl. Phys.*, 35(41):2052–2056, 1996.
- [112] L. Golonka, P. Bemnowicz, D. Jurkow, K. Malecha, H. Roguszczyk, and Tadaszak R. Low temperature co-fired ceramics (LTCC) microsystems. *Optica Applicata*, XLI(2):383–388, 2011.

- [113] CoorsTek. Thin-Film Ceramic Substrates: Design Guide <https://www.coorstek.com/media/2857/01041-thin-film-substrates-design-guide.pdf>.
- [114] M. Lindorf, H. Rohrmann, G. Span, and M. Albrecht. Effect of Percolation on Structural and Electrical Properties of MIC Processed SiGe/Al Multilayers. *J. Electron. Mater.*, 45(3):1730–1733, 2016.
- [115] M. Lindorf, H. Rohrmann, G. Span, S. Raoux, J. Jordan-Sweet, and M. Albrecht. Structural and thermoelectric properties of SiGe/Al multilayer systems during metal induced crystallization. *J. Appl. Phys.*, 120:205304, 2016.
- [116] R. O. Simmons and R. W. Baluffi. Measurements of the High-Temperature Electrical Resistance of Aluminum: Resistivity of Lattice Vacancies. *Phys. Rev.*, 117(1):62–68, 1960.
- [117] C.-W. Hwang, M.-K. Ryu, K.-B. Kim, S.-C. Lee, and C.-S. Kim. Solid phase crystallization of amorphous $\text{Si}_{1-x}\text{Ge}_x$ films deposited on SiO_2 by molecular beam epitaxy. *J. Appl. Phys.*, 77(7):3042–3047, 1995.
- [118] Z. Zamanipour, E. Salahinejad, P. Norouzzadeh, J. S. Krasinski, L. Tayebi, and D. Vashaee. The effect of phase heterogeneity on thermoelectric properties of nanostructured silicon germanium alloy. *J. Appl. Phys.*, 114:023705, 2013.
- [119] A. Zera. Thermoelektrische Eigenschaften von AIC prozessierten SiGe-Schichtsystemen, Master Thesis, Universität Augsburg, Augsburg, 2016.
- [120] R. L. Nolder, D. J. Klein, and D. H. Forbes. Twinning in Silicon Epitaxially deposited on sapphire. *J. Appl. Phys.*, 36(11):3444–3450, 1965.
- [121] Y. Park, C. G. Kind, and S. H. Choi. Rhombohedral epitaxy of cubic SiGe on trigonal c-plane sapphire. *J. Cryst. Growth*, 310:2724–2731, 2008.
- [122] C. K. Maiti and G. A. Armstrong. *Applications of silicon-germanium heterostructure devices*. CRC Press, 2001.
- [123] R. L. Petritz. Theory of Photoconductivity in Semiconductor Films. *Phys. Rev.*, 104(6):1508–1516, 1956.
- [124] J. Y. W. Seto. The electrical properties of polycrystalline silicon films. *J. Appl. Phys.*, 46(12):5247–5254, 1975.
- [125] K. v. Maydell, S. Brehme, N. H. Nickel, and W. Fuhs. Electronic transport in P-doped laser-crystallized polycrystalline silicon. *Thin Solid Films*, 487:93–96, 2005.

Acknowledgment

This work would not have been possible without the help and support of many people. First, I would like to thank the former group of Surface and Interface Physics from the Technical University of Chemnitz where I started my quest for scientific research and never felt left alone with all the questions and problems I had to face especially at the beginning of my work. Secondly, I also want to express my gratitude to the whole chair of Experimental Physics IV from the University of Augsburg where I continued my research after a change of working place. Also here, I was welcome and integrated into this new team by everybody. Both research groups exhibited a lively and nice atmosphere providing motivation in the form of excursions, (non-)coffee breaks, Friday beers, and cheerful discussions about scientific and non-scientific topics.

I want to express my gratitude in particular towards the following people:

- Prof. Manfred Albrecht for welcoming me in his research group and giving me the opportunity to work in this interesting research field on my own ideas. I am especially thankful for having the chance to follow him to Augsburg which opened a whole new world to me in many ways.
- Dr. Hartmut Rohrmann who initiated the research on thermoelectric SiGe thin films and acted as the direct link to the company of Oerlikon Balzers regarding all my wishes and questions with respect to preparation of my samples there.
- Anna Zera for her work in the form of sample preparation and countless measurements during her master thesis laying the foundation for the results of the last chapter of this dissertation.
- my fellow thermoelectricians Dr. Marcus Daniel, Felix Timmermann, and Jonny Franke who always - despite having their own problems and workload - were there for me, if a second opinion or helping hand was needed.
- Dr. Gunther Beddies and Prof. Helmut Karl for their vast knowledge they shared among numerous discussions.
- Prof. Simone Raoux for being interested in my research topic and performing the time-resolved in-situ XRD measurements.
- Beate Mainz and Dr. Oliver Klein for measuring my TEM samples, but also training me to be able to use a TEM on my own.

BIBLIOGRAPHY

- Dr. Birgit Hebler, Natalia Safonova, Dr. Dmitriy Mitin, Dr. Andreas Liebig, Dr. Dennis Nissen, Dr. Christian Schubert, and Dr. Patrick Matthes for being courageous, helpful, and friendly colleagues during the time I had the pleasure working with them.
- my family for without its support this dissertation would not have been possible this way.
- all my friends who kept me company during these years and extended the time needed to finish this work, because all good things come to an end.

Friends are like lanterns in a dark night: They may not shorten your journey, but definitely brighten it.

Publications

List of publications:

- M. Lindorf, H. Rohrmann, G. L. Katona, D. L. Beke, H.-F. Pernau, and M. Albrecht. Nanostructured SiGe thin films obtained through MIC processing. *Materials Today: Proceedings*, 2:557-565, 2015.
- M. Lindorf, H. Rohrmann, G. Span, and M. Albrecht. Effect of Percolation on Structural and Electrical Properties of MIC Processed SiGe/Al Multilayers. *J. Electron. Mater.*, 45(3):1730-1733, 2016.
- M. V. Daniel, M. Lindorf, and M. Albrecht. Thermoelectric properties of skutterudite CoSb₃ thin films. *J. Appl. Phys.*, 120:125306, 2016
- M. Lindorf, H. Rohrmann, G. Span, S. Raoux, J. Jordan-Sweet, and M. Albrecht. Structural and thermoelectric properties of SiGe/Al multilayer systems during metal induced crystallization. *J. Appl. Phys.*, 120:205304, 2016.

List of oral presentations:

- 15th European Conference on Thermoelectrics (ECT2014), *Nanostructured SiGe thin films obtained through MIC processing*, Madrid (Spain), 2014
- 34th International Conference on Thermoelectrics (ICT2015), *Evolution of transport properties of multilayered SiGe/Al thin films during MIC phase change*, Dresden (Germany), 2015
- 36th International Conference on Thermoelectrics (ICT2017), *Thermoelectric nanocrystalline SiGe thin films prepared by the combination of AIC and SiO₂ reduction*, Pasadena (USA), 2017

